Carnegie Mellon University
MELLON COLLEGE OF SCIENCE

THESIS

SUBMITTED IN PARTIAL FULFILLMENT OF THE REQUIREMENTS
FOR THE DEGREE OF

DOCTOR OF PHILOSOPHY IN THE FIELD OF PHYSICS

TITLE: "Structural studies of peripheral membrane proteins involved in HIV-1 infection and propagation."

PRESENTED BY: Rebecca Eells

ACCEPTED BY THE DEPARTMENT OF PHYSICS

Mathias Loesche	2/14/18
MATHIAS LOESCHE, CHAIR PROFESSOR	DATE

Scott Dodelson	2/14/18
SCOTT DODELSON, DEPT HEAD	DATE

APPROVED BY THE COLLEGE COUNCIL

Rebecca Doerge	3/02/18
REBECCA DOERGE, DEAN	DATE

Structural Studies of Peripheral Membrane Proteins Involved in HIV-1 Infection and Propagation

by

Rebecca Eells

Submitted in partial fulfillment of the
requirements for the degree of
Doctor of Philosophy
in
Molecular Biophysics and Structural Biology
from
Carnegie Mellon University
Pittsburgh, Pennsylvania

Thesis Committee:
Mathias Lösche (Chair)
Frank Heinrich
Markus Deserno
Patrick van der Wel

January 30, 2018

Abstract

Soluble peripheral membrane proteins form a class of proteins that transiently associate with the membrane. Even though the interactions are transient, the peripheral membrane proteins often undergo conformational changes at the membrane interface in order to perform their function. As a result, studying the protein separate from a lipid environment often provides insufficient information to fully understand the biological processes in which these proteins are involved. Neutron reflectometry offers particular advantages to studying peripheral membrane proteins in a biomimetic membrane environment. In this thesis I discuss the application of surface sensitive techniques, including electrochemical impedance spectroscopy, surface plasmon resonance, and neutron reflection, to the study of peripheral membrane proteins involved in HIV-1 viral assembly and propagation.

HIV-1 matrix is the myristoylated membrane-targeting domain of the Gag polyprotein, which is the structural factor required for viral assembly and capsid formation. Matrix uses multiple motifs for membrane association including hydrophobic, electrostatic, and lipid specific interactions with PIP_2. As a result, matrix is conformationally flexible and can adopt multiple conformations at the membrane depending on which motifs are engaged. We identified experimental conditions that overcame the challenges presented by this flexibility and allowed us to determine the effect of myristoylation on the structural organization of matrix bound to charged membranes. The presence of the myristate resulted in shift in membrane contacts from helix II for non-myristoylated matrix on charged membranes to helix I and brought the basic patch used for electrostatic interactions into direct contact with the membrane. In addition the myristoyl-dependent re-orientation positioned key residues favorably for engagement of PIP_2.

Relatively simple lipid compositions (two or three components) have been essential for dissecting the molecular mechanisms that drive membrane attraction and determining the membrane-bound structures of matrix and other peripheral membrane proteins. However, to bridge the gap to complementary studies in a cellular context it is desirable to also conduct measurements using model membranes with lipid compositions that more closely mimic the target cellular membranes. In the case of matrix, this means a model membrane mimic for the inner leaflet of the plasma membrane. Complex, PE-containing tethered bilayer membranes were developed as model membrane mimics of the inner leaflet of the plasma membrane using an adapted osmotic shock vesicle fusion method for bilayer formation. The effect of the PE-containing complex model membrane on the binding affinity of myristoylated matrix was then measured. Inclusion of PE increased the affinity of myristoylated matrix for charged, cholesterol containing membranes. A plasma membrane mimic containing relevant phosphoinositides was also developed to be used in future matrix work.

In addition to matrix, the membrane interactions of the HIV-1 accessory protein Nef were measured using tethered bilayer membranes. Full-length Nef consists of a well-folded core and a flexible, myristoylated N-terminal arm. The core is primarily responsible for interactions with binding partners essential to Nef function, such as tyrosine kinases, while the N-terminal arm drives membrane binding via the myristate and charged residues. The structure of myristoylated Nef was previously determined using neutron reflectometry on fully (100%) charged monolayers. To determine the conformation of myristoylated Nef on more physiologically relevant bilayers of moderate charge (30%), neutron reflectometry was again applied. For both model systems the Nef core was dynamic and displaced from the membrane while the N-terminal myristate and charged residues anchored the protein on the membrane. The displacement of the core from the membrane interface is presumably amenable for interactions with membrane-bound kinases and may also result in dimerization. To provide indirect evidence for dimerization, a dimerization defective mutant was also measured to probe for conformational differences. The distance of the Nef core from the membrane differed slightly for wild-type Nef and the mutant, although it may simply be due to differences in surface concentration.

The long-term goal of the Nef project is to determine the membrane-bound structure(s) of Nef in complex with host cell tyrosine kinases implicated in HIV-1 infection via their interactions with Nef. However, it is important to understand the membrane-interactions of the individual components of the complex before measuring them together. The membrane-association of two non-receptor tyrosine kinases that interact with Nef, Itk and Hck, were measured. Unfortunately, Itk was difficult to express and purify and was aggregation-prone during measurements. Measurements with Hck were more successful and yielded interesting results. We focused on the disordered N-terminal SH4-U region implicated in membrane-targeting and downstream function for which the mechanism(s) controlling these processes are not understood. For the isoform of Hck studied here, the SH4-U region was found to specifically target PA lipids, and the PA/protein interaction resulted in a persistently bound state in which the protein was partially inserted. Addition of a regulatory domain to the SH4-U construct appeared to change the lipid-binding behavior of the protein, which suggests a role for the regulatory domains in modulating the membrane-association of the protein in addition to their known role in regulating the activity of the kinase domain.

Acknowledgments

I would like to thank my advisor/mentor Dr. Mathias Lösche for his guidance and support as I navigated graduate school and transitioned from physics into molecular biophysics and structural biology research. I would also like to thank Dr. Frank Heinrich for his mentorship and keeping a cool head whenever my brain was running a mile a minute. Thank you to my committee members Drs. Markus Deserno and Patrick van der Wel for supporting my progress and offering advice and encouraging words. Thank you to Dr. Marilia Barros for showing me the ropes in the lab and offering advice on my projects as I found my way, as well as for all the hard work on the matrix project which I was able to continue. This work would not be possible without my collaborators: Dr. Ioannis Karageorgos (matrix project); Drs. Matthew Pond and Benoit Roux (Hck project); Kindra Whitlatch, Dr. John Jeff Alvarado, and Dr. Tom Smithgall (Itk and Nef project).

Thank you to my previous mentors Mr. Brent Patterson and Dr. Jenny Magnes for challenging and encouraging me. From high school chemistry class to college physics and my first introduction to biophysics research–I wouldn't be here without you.

To my friends and family – thank you for sticking with me through the highs and lows of this wild journey.

Finally, I would like to thank my unofficial therapy animals – Bunsen, Zoey, and Charlie. The cuddles, purrs, and hugs helped keep me sane.

J.K. Rowling,
Harry Potter and the Prisoner of Azkaban
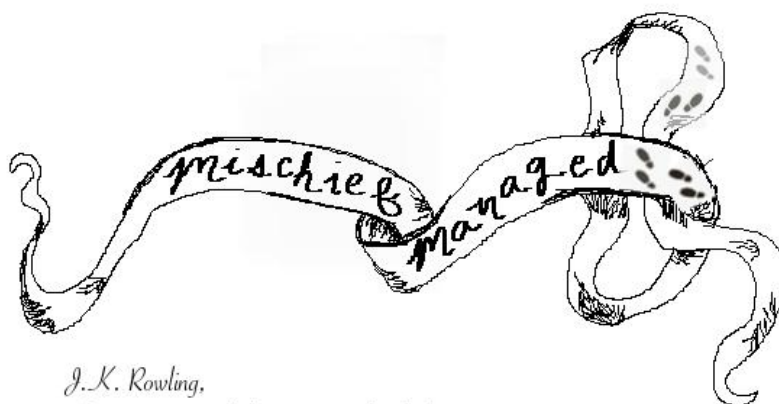
List of Publications

K. Zimmermann, **R. Eells**, F. Heinrich, S. Rintoul, B. Josey, P. Shekhar, M. Lösche, L.J. Stern (2017) "The cytosolic domain of T-cell receptor ζ associates with membranes in a dynamic equilibrium and deeply penetrates the bilayer." J. Biol. Chem. **292**(43), 11746.

R. Eells, M. Barros, K.M. Scott, I. Karageorgos, F. Heinrich, and M. Lösche (2017) "Structural characterization of membrane-bound human immunodeficiency virus-1 Gag matrix with neutron reflectometry." Biointerphases **12**(2):02D408.

Contents

List of Tables

List of Figures

Chapter 1

Introduction

Retroviruses are membrane enveloped single-stranded RNA viruses that contain two full copies of their RNA genome [1–3] and share three common features: receptor mediated host cell entry, reverse transcription of the RNA genome into double stranded DNA that is integrated into the host cell genome, and primarily cytosolic assembly of the viral particles [4]. Retroviral replication starts with host cell entry via receptor binding followed by fusion of the viral and host cell membranes either directly at the cell surface or within the endosome for viruses that utilize endocytic uptake for entry. Following membrane fusion, the viral core enters the cytoplasm where the single stranded RNA genome is transcribed into double stranded DNA. The viral DNA is then delivered from the cytoplasm to the nucleus where it is inserted into the host cell genome and transcribed by the host RNA polymerase II system. Following mRNA transcription, the viral RNAs are processed and exported out of the nucleus into the cytoplasm. In the cytosol the structural factors needed for particle assembly are translated then targeted to the plasma membrane (PM) where assembly occurs [5]. Once assembled, the viral particles bud from the PM from which they acquire their lipid envelope [6]. Maturation occurs after the particles are released resulting in infectious virions [5].

Three genes, *pol*, *env*, and *gag*, are common to all retroviruses [1–4]. The *pol* gene encodes proteins involved in reverse transcription and integration of viral DNA into the host genome, as well as the viral protease essential for virion maturation. The protein products of the *env* gene mediate receptor binding and membrane fusion. Finally, the *gag* gene encodes the structural factor essential for capsid formation [1–3]. Retroviruses are considered either simple or complex depending on the organization of their genome. Both types contain two full-length copies of the single-stranded RNA genome, and these full-length RNA transcripts encode the *gag* and *pol* gene products. In addition, both simple and complex retroviruses splice a subset of genomic RNA to produce a transcript that encodes the protein product of *env*. Complex retroviruses, however, produce additional singly and multiply spliced transcripts resulting in unique regulatory and accessory proteins. For example, lentiviruses express at least two con-
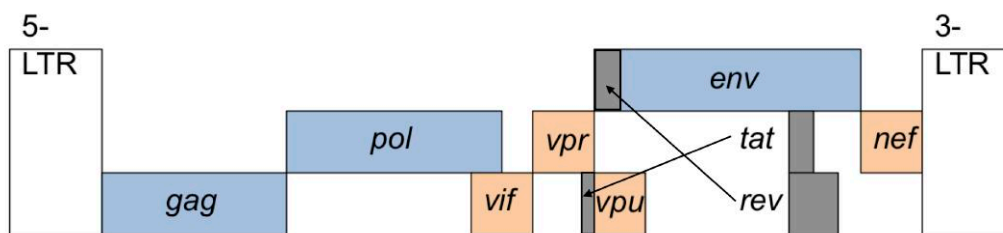
Figure 1.1: Genome organization of HIV-1 DNA. 5' and 3' long terminal repeats (LTR) are shown in white. LTR regions contain repeats of noncoding DNA used by viruses to insert the viral genome into the host genome [10]. Conserved retroviral genes (*gag, pol, env*) are shown in blue. Regulatory genes (*tat, rev*) are shown in gray. Accessory proteins (*vif, vpr, vpu, nef*) are shown in orange. Figure adapted from [9].

served regulatory proteins, Tat and Rev, and primate lentiviruses produce additional accessory proteins that enhance viral replication and infectivity [7].

Human immunodeficiency virus (HIV) is a complex retrovirus, more specifically a primate lentivirus, and the causative agent of acquired immune deficiency syndrome (AIDS). There are two subtypes, HIV-1 and HIV-2. Most HIV infections worldwide are caused by HIV-1 while HIV-2 is primarily localized to West Africa. HIV-1 is also more pathogenic with an increased likelihood of progressing to AIDS compared to HIV-2 [8]. The HIV-1 genome contains nine genes essential for the assembly of infectious virions [9]. The genome contains *pol, env*, and *gag*, common to all retroviruses, and also encodes the lentiviral regulatory factors Tat and Rev. In addition, the genome encodes four accessory proteins Vif, Vpr, Vpu, and Nef [7]. The DNA genome organization of HIV-1 is shown in Figure 1.1.

In this work two aspects of HIV-1 infection were investigated: (1) the membrane association of the myristoylated membrane-targeting domain of the structural factor (Gag polyprotein) required for viral assembly and capsid formation and (2) the interactions of the accessory protein Nef at the membrane. Two biophysical techniques were primarily used, surface plasmon resonance (SPR) and neutron reflectometry (NR), to measure protein binding affinities to membranes of varying composition and the structure of the membrane-bound proteins, respectively. An introduction to these techniques is provided in Chapter 2, and examples of their application to the study of HIV-1 membrane-associated proteins are provided in the remaining chapters. Chapters 3 and 4 focus on method development applied to the study of the membrane-association of the myristoylated membrane targeting domain of the Gag polyprotein. Chapter 3 details the development of complex tethered bilayer lipid membranes as model membranes which mimic of the inner leaflet of the PM. In Chapter 4 the effect of these complex model membranes on the binding affinity of
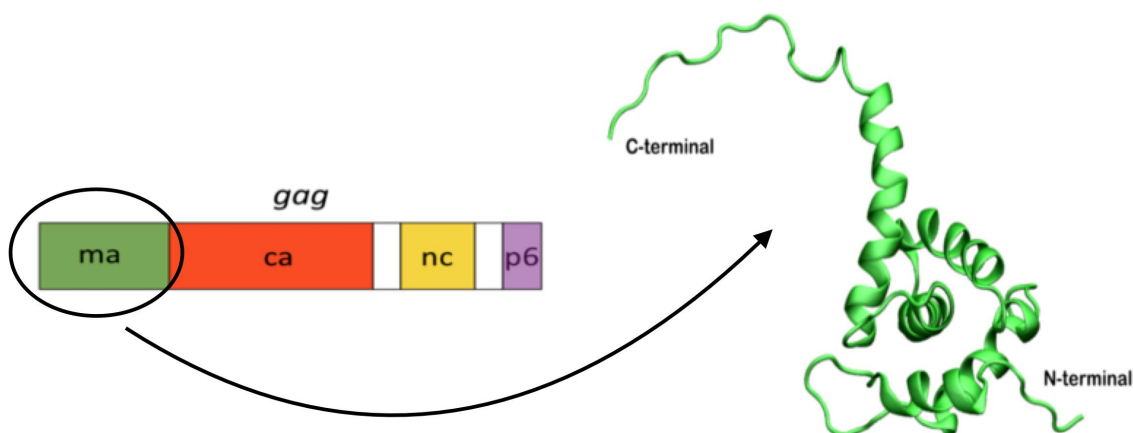
Figure 1.2: Domain organization of the *gag* gene and solution structure of HIV-1 MA. *gag* encodes the Gag polyprotein which contains four major structural protein domains: MA (green), CA (red), NC (yellow), and p6 (purple). The domains are connected by spacer peptides represented in white. The solution structure of non-myristoylated MA is primarily α helical with a flexible C-terminal. The image was rendered using PDB 2H3F (NMR ensemble from [18]).

the myristoylated membrane targeting domain of Gag is discussed. Chapter 4 also introduces the the challenges associated with probing the structure of a protein with reduced solubility that uses multiple binding motifs for membrane-association and the conditions needed to overcome these obstacles. Then the structural organization of the myristoylated protein on a charged model membrane is revealed. Chapters 5-7 focus on the accessory protein Nef and its membrane interactions, as well as the membrane-interactions of two host cell kinases that are activated by Nef, as a first step towards determining the structure(s) of membrane-bound Nef:kinase complexes.

1.1   HIV-1 Gag Matrix

HIV-1 encodes a Gag polyprotein required for viral assembly and capsid formation [11] that contains four major structural domains to perform its function: matrix (MA), capsid (CA), nucleocapsid (NC), and p6 as well as connecting spacer peptides [12] (Figure 1.2). Membrane targeting of Gag is mediated by the myristoylated N-terminal MA domain, which is a common feature of many retroviruses [6]. MA recognizes specific components of the PM and binds to the membrane via several physical interactions including a hydrophobic anchor [13–15]; electrostatic attraction [14, 16, 17]; and lipid specificity for $PI(4,5)P_2$ [18–20].

3

Previously, the structure of non-myristoylated matrix, –myrMA, on charged model membranes was determined using NR, which resulted a model for membrane association driven purely by electrostatics [21]. The observed orientation of the protein on the membrane was favorable for Gag lattice formation. However, it was not clear from this study if myristoylation would further modulate the structural organization of the protein on the membrane. More recently, free energy calculations of MA binding to membranes of varying composition revealed how individual bilayer components and protein myristoylation contribute to MA membrane association [22] but did not provide structural information. The study did, however, show that efficient membrane-association is driven not only by lipids that directly engage the protein but by membrane properties as a whole, based on the effect of cholesterol on binding affinity. The lipid compositions used were relatively complex (three to four components) [22], but they lacked phosphatidylethanolamine (PE)—the main zwitterionic component of the inner leaflet of the PM [23]. Even if MA does not directly bind PE lipids, PE may impact MA membrane association since the target membrane contains significant amounts of PE.

This work advances previous studies on the membrane-association of HIV-1 matrix presented in [21] and [22]. Two aspects of myristoylated (myr) MA membrane association were studied in parallel: the structure of myrMA on a simple, charged membrane using NR and the effect of a PE-containing PM mimic on myrMA binding affinity. To determine the membrane-bound structure of myrMA with NR a specific set of experimental conditions (50mM NaCl, pH 8, and a membrane containing 50% charged lipid species) were needed to overcome the challenges presented by the conformationally dynamic membrane-association of MA and reduced solubility due to the myristoyl moiety. These challenges and the conditions needed for structure determination are discussed. Then I report the structural organization of myrMA on charged membranes and compare it with the structure of –myrMA [21] to show the effect of myristoylation on the orientation of membrane-bound MA. For MA, relatively simple lipid compositions have been key for determining membrane-bound structures [21,24] and dissecting the interactions that drive membrane binding [22]. However, in order to bridge the gap to complementary studies in a cellular context, it is desirable to more closely mimic the lipid compositions found in cellular membranes. To establish a mimic of the inner leaflet of the PM, it was important to first develop defect-free PE-containing planar bilayer membranes, then increase the complexity to include cholesterol, anionic lipids, and, finally, PI(4,5)P$_2$. Here I discuss the development of the PM mimic then investigate the effect of PE on the binding affinity of myrMA.

1.2   HIV-1 Nef

HIV-1 negative regulatory factor (Nef) is a membrane-associated accessory protein that is essential for viral replication, immune evasion, and AIDS progression [25]. Nef exhibits no intrinsic catalytic activity, has no direct role in viral reproduction, and
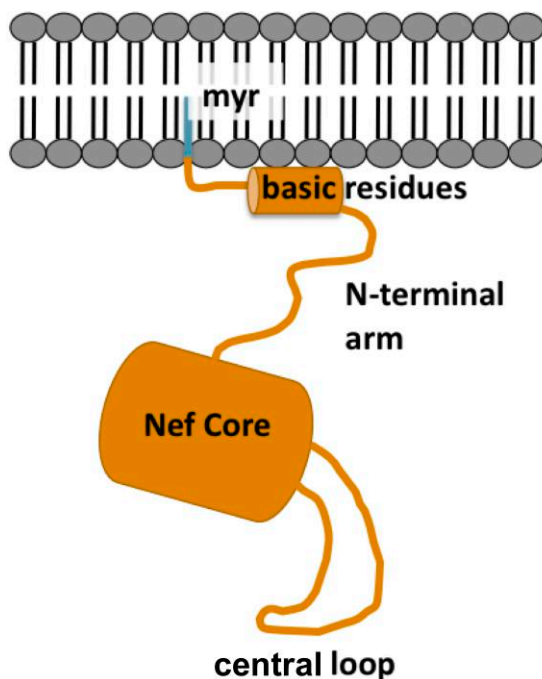
Figure 1.3: Model for membrane-bound myristoylated Nef. The interactions between Nef and the membrane via insertion of the myristate and a patch of basic residues on the N-terminal arm resulted in displacement of the Nef core from the membrane surface. The separation between the N-terminal arm and core may be favorable for dimerization [26] and interactions with host cell proteins. (Figure based on data from [32] and adapted from [33]).

does not serve a structural role in virion assembly. Instead Nef functions through interactions with multiple classes of host cell proteins involved in signal transduction and trafficking via the endosomal pathway [26–29]. Structurally Nef contains a disordered N-terminal arm (residues 2-54) and a well-folded core domain (residues 55-206) that contains a flexible central loop (residues 149-179) [34]. The core domain is primarily responsible for interactions with host cell proteins while membrane association is driven by a N-terminal myristate and a patch of basic residues on the N-terminal arm. *In vivo*, myristolyation is required for Nef function [30, 31], which demonstrates the importance of membrane-association for Nef-mediated enhancement of HIV-1 infection and disease.

Despite the importance of the membrane for Nef function, there is limited structural information about the membrane-associated form(s) of Nef. NR has been successfully used to determine the structure of Nef on charged monolayers [32]. Non-myristoylated Nef adopted a single conformation with the core in contact with the lipid monolayer whereas the conformation of myristoylated Nef was dynamic with the
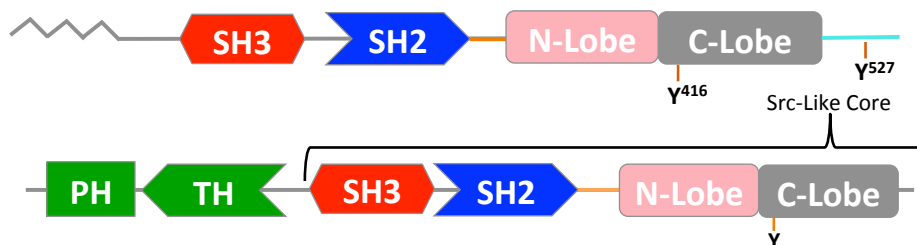
Figure 1.4: Domain organization of Src and Tec family kinases. SFK domain organization is shown on top and TFK organization is shown on bottom.

core displaced from the monolayer (Figure 1.3) at a range of distances [32]. There is increasing evidence that Nef forms dimers on the membrane and that dimerization is required for at least some functions of Nef [37, 38]. While reflectivity measurements cannot directly detect dimer formation, since this method is not sensitive to structural changes in the plane of the membrane, the previously observed conformation of Nef with the core separated from the N-terminal arm [32] is favorable for exposure of the dimerization interface [26]. In terms of physiological relevance, model bilayer lipid membranes capture the cellular environment better than lipid monolayers. In addition, the monolayers used in the previous NR measurements were fully charged, which also deviates from physiological relevance. Thus, the measurements on bilayer membranes of relevant charge ($\sim$30%), presented here, were important to validate the structural model proposed based on the monolayer data [32]. In this work I used SPR to determine the affinity of various Nef constructs to charged membranes and optimize conditions for NR experiments. Then NR was used to probe the structure of myristoylated Nef and a dimerization defective Nef mutant at a membrane bilayer interface. Differences in the membrane-bound structures of the wildtype and mutant protein may be indicative of dimerization.

1.2.1   Non-Receptor Tyrosine Kinases Activated by Nef

The two largest families of non-receptor tyrosine kinases (nRTK) are the Src family and Tec family kinases (SFKs and TFKs, respectively) [39]. SFKs and TFKs share a similar domain structure with a Src homology 3 (SH3) and Src homology 2 (SH2) regulatory domains followed by a catalytic domain (Figure 1.4). For both families membrane targeting is driven by the N-terminal region, although the mechanism for membrane binding differs. In addition, members of both families are expressed in HIV-1 target cells and have been implicated in HIV-1 propagation and progression to AIDS through interactions with Nef [40, 41].

In this work I focused on the membrane interactions of two kinases that are constitutively activated by Nef: Hck (a Src kinase) and Itk (a Tec kinase). Nef-

mediated Hck activation contributes to enhanced viral replication [42,43] and immune evasion through downregulation of MHC-1 [44,45], and Itk activation has been shown to be essential for multiple steps of the HIV-1 life-cycle [46]. Since both kinases and Nef are membrane-associated proteins it has been postulated that Nef:kinase interactions occur on the PM [40,41]. Most studies of Nef:kinase complexes, however, are solution based or crystallographic. While these studies provide a foundation for understanding the Nef:kinase interaction, they do not account for the influence of the membrane on the binding partners. In addition, the mechanisms that regulate membrane-binding for the kinases, even in the absence of Nef, have not been fully elucidated. For Itk, the interaction between the N-terminal Pleckstrin homology (PH) domain and target lipid phosphatidylinositol-3,4,5-triphosphate, found on the inner leaflet of the PM, is well-understood. More recently, it has been reported that SH2 domains, which both Itk and Hck contain, are also capable of binding lipids with submicromolar affinity [47]. However, the study was conducted using the isolated SH2 domain, thus does not address if the presence of the other domains modulate the lipid binding behavior of the SH2 domain. For Hck, the N-terminal membrane-targeting region is intrinsically disordered, and this region does not exhibit sequence homology between different SFK members [48]. While myristoylation is important for membrane-association, the disordered region also appears to have an active role in membrane targeting that may be modulated by the regulatory domains (SH3-SH2) [49,50]. While the eventual aim of the Nef project is to reconstitute Nef:kinase complexes at a model membrane interface, the first step towards this goal is obtaining a full understanding of the membrane-interactions of the individual proteins (Nef, Itk, Hck). To begin probing the mechanisms that drive membrane binding for Itk and Hck, non-full length constructs were used to probe the membrane interactions of the PH and SH2 domain of Itk and the disordered region of Hck and optimize conditions for measurements with full-length kinase.

1.3   Motivation

All the proteins presented in this work are involved in the HIV-1 lifecycle, and elucidating their interactions with and at the membrane helps further our understanding of HIV-1 infection. Due to the critical role of membrane-interactions for protein function, it is important to study these proteins in a membrane environment to gain a full understanding of the processes in which they are involved. This detailed knowledge provides insight into the overall pathogen biology and may lead to the development of new and better therapeutics. While current treatments for HIV-1 infection have taken it from a life-threatening illness to a chronic condition—for those with access to the antiretrovirals—prolonged retroviral treatment can lead to negative side effects, such as organ damage and the mutation into drug-resistant strains.

Beyond HIV-1, the proteins investigated in this work are more generally connected because they are peripheral membrane proteins that shuttle between the cytosol and

cellular membranes. Peripheral membrane proteins perform a wide range of functions within the cell and are involved in cell signaling: the transfer of chemical information into and out of the cell, enzymatic activities on membrane components, regulation of integral membrane proteins, transport of small molecules or electrons, and structural support for the localization of proteins/protein complexes on the membrane. To achieve their broad range of functionality, peripheral proteins, in many cases, interact only temporarily with lipid membranes or receptor sites in integral membrane proteins [51, 52]. Even when the interactions between the protein and membrane are transient, these interactions can lead to structural rearrangements or conformational changes in the protein that allow it to perform its function [53]. As such, structures of the solution state of these proteins, while valuable, often provide insufficient information to fully understand the biological processes in which they are involved. Reflectometry techniques offer distinct advantages for characterizing proteins in a biomimetic membrane environment [54–57], and the tools used in this work have transformed the technique to allow for routine studies of membrane associated proteins [57–62].

Chapter 2

Experimental Techniques

Sparsely-tethered lipid bilayer membranes (stBLMs) are resilient biomimetic model membranes used to study the interactions driving protein association with lipid bilayers and the resulting membrane-bound structures. The properties and formation of stBLMs will be discussed in section 2.1 followed by an introduction to the surface sensitive techniques, electrochemical impedance spectroscopy (EIS; section 2.2), SPR (section 2.3), and NR (section 2.4), used to probe the protein/membrane interactions. In this work EIS was used to assess the quality of the stBLMs before and after protein incubation and optimize more complex lipid mixtures. SPR was used to determine the molecular-level interactions that drive association of the protein with the membrane and optimize experimental conditions for NR measurements. Finally, NR was used to obtain structural details of the membrane-bound proteins.

2.1 stBLMs

2.1.1 Introduction

In the stBLM system (Figure 2.1) a bilayer membrane is adsorbed to a gold-coated substrate via a chemical linker resulting in a resilient, in-plane fluid system [63–66]. The tether molecules have a central polyethylene chain of 6-9 repeat units and are functionalized with two hydrocarbon chains on one end, either saturated or unsaturated, that integrate into the inner leaflet of the supported lipid bilayer. The other end has a thiol or thiol acetate group that binds to the gold film on the substrate. The tether molecule used in this work, HC18, was synthesized by David Vanderah (Institute for Bioscience and Biotechnology Research; IBBR). HC18 has unsaturated dioleoyl chains providing more fluidity to the lipid bilayer than previously used tether molecules [65]. A small spacer molecule, β-mercaptoethanol (βME), is co-adsorbed with the tethers to lower the density of tether molecules (i.e. make the bilayer "sparsely-tethered") and passivate the gold surface. Incorporation of the tether molecule provides $\sim$20 Å of hydrated space between the lipid bilayer and substrate
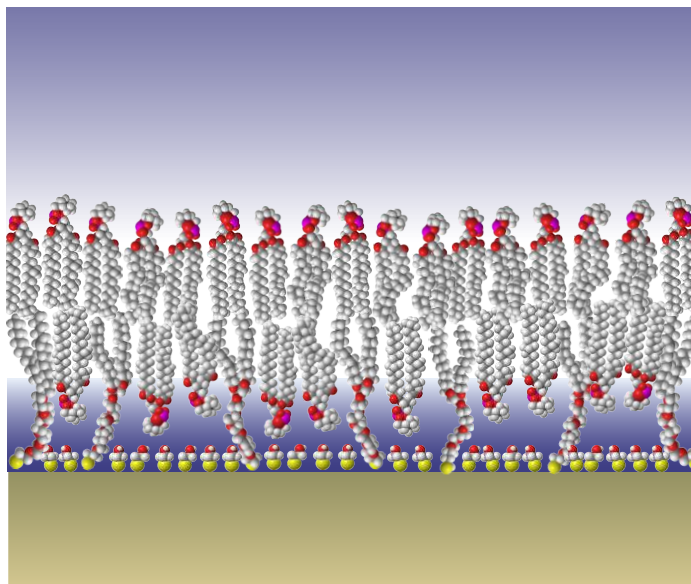
Figure 2.1: Sparsely-tethered bilayer lipid membrane. The lipid bilayer is coupled to a gold-coated solid support by a synthetic lipid used as a tether. A spacer molecule is used to control the density of the tether ("sparsely-tethered").

which prevents interactions with the solid support and results in lipid diffusion rates of the interspersed free phospholipids comparable to that of unilamellar vesicles [66]. The tether also ensures a flat membrane of low roughness and long-term stability. stBLMs have a low defect density, and we have not encountered any limitations for lipid composition. While stBLMs are not as complex as a native membrane, they capture many of the fundamental aspects of biomembranes.

2.1.2 stBLM formation

Self Assembled Monolayer (SAM)

Self-assembled monolayers (SAMs) were formed on gold-coated glass microscopy slides (3" X 1" X 1 mm; Thermo Fisher Scientific, Waltham, MA) or silicon wafers (3" diameter, 5 mm thick n-type Si:P[100] wafer; El-Cat Inc., Ridgefield Park, NJ) for SPR and NR, respectively. The substrates were cleaned with 5 vol% Hellmanex solution (Hellma Analytics, Müllheim, Germany) then sulphuric acid plus Nochromix (Godax Laboratories, Cabin John, MD). These steps are followed by excessive rinsing with ultrapure water (EMD Millipore, Billerica, MA) and pure ethanol (EtOH; Pharmo-Aaper, Shelbyville, KY) and drying of the substrates in a N_2 gas stream. The substrates were then coated with chromium ($\sim$20 Å) and gold ($\sim$150 Å and $\sim$ 450 Å for NR and SPR, respectively) by magnetron sputtering (ATC Orion; AJA International, Scituate, MA). For NR experiments rough interfaces lead to attenuation of the

reflectivity curve. Thus, the interfacial roughness of the gold film should be $\sigma < 5$ Å, assuming a typical roughness of $\sigma < 3$ Å for the polished wafer. σ is the root mean square deviation from a perfectly smooth surface. The gold-coated substrates were incubated in an ethanolic solution of HC18 and βME (30:70 mol/mol tether:spacer, unless otherwise stated) at a total concentration of 0.2 mM to form a SAM.

stBLM Completion

In this work, stBLMs were formed using an osmotic shock vesicle fusion method. In this method lipids from stock solutions in chloroform are mixed at desired molar ratios. Then the organic solvent is evaporated under vacuum for 12 h to form a lipid film. Vesicles are formed by hydrating the lipid films in high salt aqueous buffer (1 or 2 M NaCl, 10 mM NaPO$_4$, pH 7.4) to a lipid concentration of 5 mg/mL. The vesicles are sonicated until clear, then the solution is then allowed to incubate the SAM for $\sim$2 h. stBLM formation is completed by flushing the system with low ionic strength buffer (50 mM NaCl, 10 mM NaPO$_4$, pH 7.4) which assists bilayer formation by vesicle rupture due to osmotic shock.

2.1.3   Materials for stBLM Preparation

All lipids, 1,2-dioleoyl-sn-glyero-3-phosphocholine (DOPC), 1,2-dioleoyl-sn-glycero-3-phosphoethanolamine (DOPE), 1,2-dioleoyl-sn-glyero-3- phospho-L-serine (DOPS), 1,2-dimyristoyl-sn-glycero-3-phosphocholine (DMPC), 1-palmitoyl-2-oleoyl-sn-glycero-3-phosphocholine (POPC), 1-palmitoyl-2-oleoyl-sn-glycero-3-phosphoethanolamine (POPE), 1-palmitoyl-d31-2-oleoyl-sn-glycero-3-phosphocholine (d$_{31}$-POPC) 1-palmitoyl-2-oleoyl-sn-glycero-3-phospho-L-serine (POPS), L-α-phosphatidylinositol (PI) from soy, L-α-phosphatidylinositol-4,5-bisphosphate (PI(4,5)P$_2$; PIP$_2$) from porcine brain, 1,2-dioleoyl-sn-glycero-3-phospho-(1'-myo-inositol-3',4',5'-trisphosphate) (PI(3,4,5)P$_3$; PIP$_3$), L-α-phosphatidylinositol-4-phosphate (PI(4)P) from porcine brain, and cholesterol from Ovine Wool were purchased from Avanti Polar Lipids, Inc. (Alabaster, AL). The tether compound HC18 was synthesized and characterized as described [65].

2.2   Electrochemical Impedance Spectroscopy

2.2.1   Introduction

The ability to form defect-free membranes is an important feature of model membrane systems and is essential for preventing non-specific binding when studying protein-lipid interactions. Membranes that are highly insulating (resistant to ion flow across the membrane) are low in defect density. EIS offers a tool to assess the bilayer quality prior to the addition of protein [68], as well as monitor the effect of protein adsorption on the membrane electrical properties.

2.2.2 Theory

EIS is an alternating current (AC) method that measures the electrical properties of a sample, such as capacitance and resistance. An AC voltage is applied across the stBLMs in an electrochemical cell and the resulting current through the sample is measured. The EI spectrum is obtained by scanning over a range of frequencies [69]. Electric circuit models are then used to obtain detailed physical information about the properties of the interfacial film [68].

In our experiments, a sinusoidal voltage [$V(t)$] of amplitude V_0 and angular frequency ω ($\omega = 2\pi f$, where f=frequency) was applied across the sample, and the phase shift (θ) and amplitude (I_0) of the resulting current [$I(t)$] was measured. The current response $I(\omega)$ of electrochemical cells is non-linear unless the excitation is small [70] and only perturbs the sample slightly from its equilibrium. In the linear regime, the response has the same frequency ω as the applied voltage but a phase shift between the applied voltage and response current, θ, is observed.

$$V(\omega) = V_0 sin(\omega t) \tag{2.1}$$

$$I(t) = I_0 sin(wt + \theta) \tag{2.2}$$

In exponential notation,

$$V(\omega) = V_0 e^{i\omega t} \tag{2.3}$$

$$I(\omega) = I_0 e^{i(\omega t - \theta)} \tag{2.4}$$

The complex electrical impedance, $Z(\omega)$, is the ratio of the applied voltage to the measured current.

$$Z(\omega) = \frac{V(\omega)}{I(\omega)} = \frac{V_0}{I_0} e^{i\theta} \tag{2.5}$$

Equation 2.5 can then be re-arranged using $Z_0 = V_0/I_0$

$$\begin{aligned} Z(\omega) &= Z_0 e^{i\theta} \\ &= Z_0 cos(\theta) + i|Z_0|sin(\theta) \\ &= Z'(\omega) + iZ"(\omega) \end{aligned} \tag{2.6}$$

where Z'(ω) and Z"(ω) are the real and imaginary parts of the impedance, respectively. The impedance of a capacitor is given by

$$Z(\omega) = \frac{1}{i\omega C} \tag{2.7}$$

where C is the capacitance which leads to the frequency dependent capacitance of the electrode

$$C(\omega) = -\frac{Z"(\omega)}{\omega|Z(\omega)|^2} - i\frac{Z'(\omega)}{\omega|Z(\omega)|^2} = C'(\omega) + iC"(\omega) \tag{2.8}$$

2.2.3   Instrumentation

EIS experiments were performed using a Solartron (Farnborough, UK) 1287A potentiostat and 1260 frequency analyzer. A three electrode configuration was used with the gold-coated substrate serving as the working electrode, a saturated silver-silver chloride (Ag|AgCl|KCl(aq,sat)) microelectrode (M-401F; Microelectrodes, Bedford, NH) as the reference electrode, and a 0.25 mm diameter platinum wire (99.9% purity, Sigma Aldrich, St. Louis, MO) coiled around the reference electrode acting as the auxiliary electrode. The potentiostat maintained a constant potential across the reference and working electrodes by adjusting the current of the counter electrode. An AC voltage of amplitude 10 mV was applied across the sample, which is small enough to ensure a linear response of the system. The frequency analyzer applied a sinusoidal wave into the electrochemical cell and measured the amplitude and phase shift of the current response at each frequency. A frequency range from 1 Hz to 100 kHz was measured with ten logarithmically distributed data points per decade. The data was acquired and modeled using Zplot and Zview (Scribner Associates, Southern Pines, NC), respectively. Measurements were carried out at room temperature at 0 V bias vs. the reference electrode over the measured frequency range.

A custom-designed Teflon electrochemical cell with six separate sample wells allowed for preparation of up to six different samples on a single substrate. Each well holds a volume of 400 μL and has a geometric area of A $\approx$ 0.33 cm^2 as determined using the copper contrast method [71]. Viton O-rings are used to ensure a tight seal between the Teflon well and the substrate. The roughness of the gold film interface, β, was estimated to be between 1.2 and 1.4 for this experimental set-up based on gold surface oxidation/oxide stripping charge. Roughness increases the surface area of the sample, and β is the factor that can be applied to the geometric area to account for this increase.

2.2.4   Data Analysis

Equivalent Circuit Model (ECM)
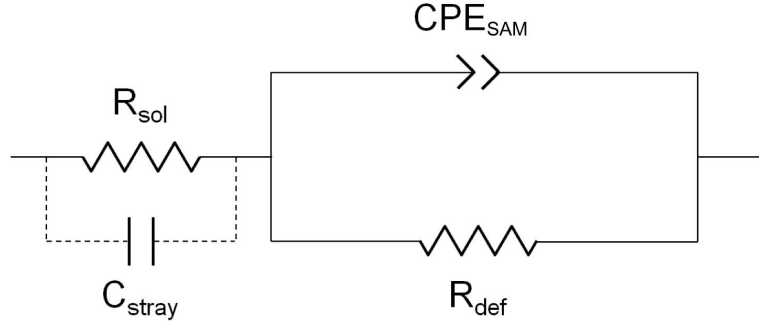
Figure 2.2: ~~F~~ ... s described as a parallel RC ... ~~e~~havior of the monolayer and ...
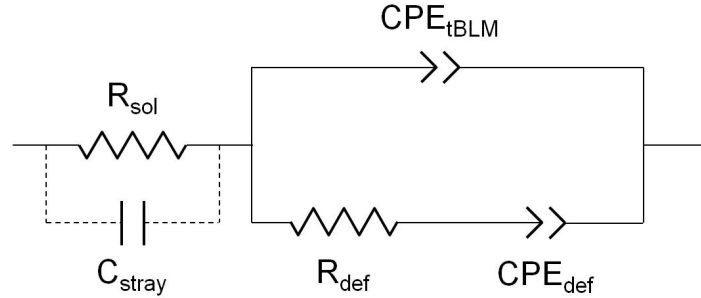
Figure 2.3: Equivalent circuit model for a stBLM. The stBLM is described by a CPE_{tBLM} in parallel with a branch that captures the membrane defects characterized by the resistance, R_{def}, and the capacitance-like behavior of the defects, CPE_{def}.

Equivalent circuit models (ECMs), in which the electrochemical system is described in terms of the electrical circuit components, were used to obtain physical parameters from the impedance data. ECMs used to fit the impedance spectra of SAMs and stBLMs are shown in Figure 2.2 and Figure 2.3, respectively. The solution resistance, R_{sol}, is the resistance of the buffer solution between the working electrode and reference electrode. The stray capacitance, C_{stray}, is from the wiring and the sample
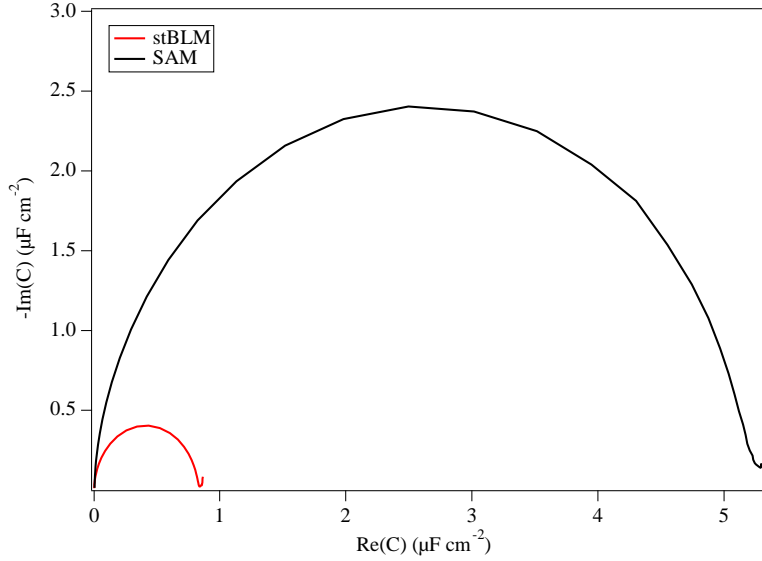
Figure 2.4: Cole-cole plot for an stBLM and a SAM. EI spectra of a 30:70 HC18:βME SAM and stBLM normalized by the surface area (A $\approx$ 0.33 cm^2) The diameter of the semi-circle provides a value of C'$\sim$5 μFcm^{-2} for the SAM and C'$\sim$0.8 μFcm^{-2} for the stBLM.

cell. Since tethered bilayer membranes with their narrow electrolyte filled submembrane space are not always well approximated by an ideal capacitor, a constant phase element (CPE) models the behavior of an imperfect capacitor.

$$Z_{CPE} = \frac{1}{CPE(i\omega)^{\alpha}} \quad \text{with} \quad 0 \leq \alpha \leq 1 \tag{2.9}$$

For $\alpha = 1$ the CPE describes an ideal capacitor. The SAM is represented by a parallel RC circuit with the monolayer capacitance-like behavior described by CPE_{SAM} and the resistance by R_{def}. The stBLM is represented by CPE_{tBLM} in parallel with R_{def} and CPE_{def}, which represent the bilayer defects in terms of the resistance and the capacitance-like behavior of the defects, respectively [63]. The impedance spectra were fit in Zview with best-fit ECM parameters determined by a Levenberg-Marquardt algorithm. The resistance and capacitance values were then normalized by the surface area of the working electrode (A $\approx$ 0.33 cm^2).

Cole-Cole Plots

Plotting the imaginary vs. real part of the complex capacitance C(ω) [C'(ω) vs. C"(ω)] produces a Cole-Cole plot, a well-established representation of impedance spectra of circuits (Figure 2.4). From the Cole-Cole plot a qualitative assessment

of the bilayer quality can be obtained. For an ideal membrane capacitor (α=1) the data appears as a semicircle, and typical α values for the stBLMs are $\geq$ 0.98. Thus, the intersection of the semi-circle with the C' axis provides the (non-normalized) capacitance of the SAM and the stBLM with C'$_{stBLM}$ < C'$_{SAM}$. The tail is a measure of the defect density of the lipid bilayer, and the length of the tail scales with the density of defects [63] with a shorter tail indicating a lower number of defects.

2.3 Surface Plasmon Resonance

2.3.1 Introduction

SPR is an analytical surface sensitive technique used to probe molecular interactions at interfaces, such as ligand-receptor interactions [72]. In this technique collective oscillations of free electrons (i.e. surface plasmons) are excited when polarized light strikes a thin metal film. Resonant excitation of the surface plasmons occurs when both the momentum and energy of the incident beam matches that of the surface plasmons. The energy and momentum matching occurs at a specific angle of incidence, known as the "resonance angle", and can be observed as a reduction in the reflected intensity at that angle [73]. Changes in the refractive index near the interface, such as when a ligand binds, result in a shift in the resonance angle allowing the detection of adsorbed molecules at the surface in real-time.

2.3.2 Theory

Detailed descriptions of the theory that describes surface plasmons and surface plasmon resonance can be found in the literature and standard textbooks (such as [74]). A brief overview is presented here. Surface plasmons are coherent oscillations of free electrons in a metal which occur due to excitation by photons of p-polarized light (which has an electric field component perpendicular to the surface). Surface plasmons can be excited in a metal film at an interface with a dielectric medium under specific conditions which are satisfied by metals like silver or gold at air or water interfaces. In terms of biological applications, gold provides advantages due to its biological and chemical inertness. When the momentum and energy of the incident monochromatic light beam simultaneously match that of plasmons supported by the geometry of the metal film, energy is converted from photons into plasmons.

In the Kretschmann configuration [76] used in this work surface plasmon resonance occurs under conditions of total internal reflection. The incident light travels through a glass prism and hits a gold film which carries the stBLM adjacent to aqueous buffer that provides membrane ligands. When electromagnetic waves travel from a medium of higher refractive index (glass prism) to one of lower refractive index (aqueous buffer) the light is partially reflected and partially transmitted at the interface. Above a certain angle of incidence, the critical angle, total internal reflection occurs and only
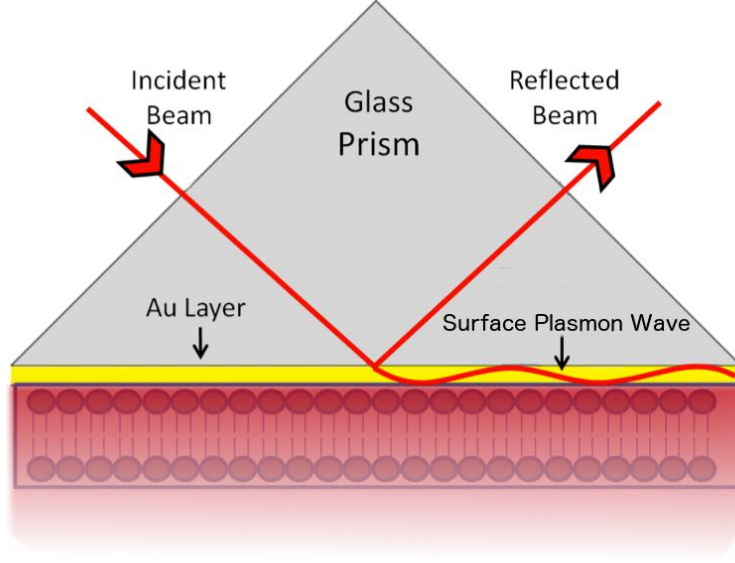
Figure 2.5: Surface plasmon resonance in the Kretschmann configuration.
The substrate carrying the stBLM is optically coupled to the glass prism using a
refractive index matching fluid. The incident beam undergoes total internal reflection
at the glass/buffer interface and generates an evanescent wave which interacts with the
free electrons in the gold film. Resonance is achieved when the energy and momentum
of the incoming beam matches that of the surface plasmons.

an evanescent wave penetrates the low-refractive index medium. Using Snell's law
the critical angle is given by [75]

$$sin\theta_c = \frac{n_{low}}{n_{high}} \tag{2.10}$$

Since the evanescent wave decreases exponentially with distance from the interface
(penetration depth of the order of the optical wavelength λ), SPR is sensitive to
changes near the interface and not the bulk. The decay length, l, is given by [75]

$$l = \frac{\lambda}{2\pi\sqrt{(nsin\theta)^2 - 1}} \tag{2.11}$$

Adsorption of molecules near the interface (in our case protein/peptide binding to the
stBLM) change the refractive index resulting in a shift in the resonance angle which
is monitored in real-time with high sensitivity to detect adsorption.

17

2.3.3   Instrumentation

SPR measurements were conducted in single batch mode using a custom-built instrument (SPR Biosystems, Germantown, MD) assembled in a Kretschmann configuration (Figure 2.5). Gold-coated ($\sim$45 nm) glass slides with a SAM were optically coupled to the glass prism using a refractive index matching fluid, n=1.52 $\pm$ 0.0002 (Cargile, Cedar Grove, NJ). A superluminescent LED (EXS7510 Exalos AG, Switzerland) fan of monochromatic light of wavelength 763.8 nm hits the sample at a range of incident angles. A 2D-CCD detector (Hamamatsu C10990, Hamamatsu City, Japan) with 250 lines of 1024 pixels records the intensity of reflected light as a function of the reflected angles, and the position of the intensity minimum (resonance angle) is recorded as a function of time. In the single-batch mode used for measurements all 250 lines are binned into one line of 1024 pixels. The time resolution of the system is 0.1 s and the sensitivity of at least 5 X 10^{-7} response units (RU; 1 RU $\sim$1 pg of adsorbed protein per mm^2). A temperature controller (Wavelength Electronics LFI-3751, Bozeman, MT) was used to maintain the temperature within $\pm$ 0.01° C. Measurements were typically conducted at 25° C. SPARia (SPR Biosystems) was used for the real-time data viewing and acquisition. The set-up allows for simultaneous EIS measurements which are used to assess the quality of the lipid membranes before and after protein incubation.

2.3.4   Data Acquisition

During a measurement, the reflected intensity as a function of pixel on the detector and the resonance angle as a function of time are monitored (Figure 2.6). The reflected intensity as a function of pixel represents a standard SPR reflectivity curve where the minimum is the resonance angle. The shift in minimum over time can then be used to monitor the adsorption of the protein/peptide to the membrane at increasing concentrations.

The measured response (R) is the position of the reflection minimum on the CCD detector. The resonance angle for the neat stBLM in the working buffer is first measured as a baseline. The change in resonance angle is then measured as increasing protein concentrations are added to the system. The resonance angle increases due to the increase in refractive index at the stBLM/buffer interface as protein binds ($n_{protein}$=1.41, n_{lipid}=1.5, and n_{bulk}=1.33 where n_{bulk} is the refractive index of the aqueous buffer). Time courses of R were recorded for each protein concentration, c_p, until equilibrated (resonance angle stops changing) at R_{eq}.

2.3.5   Data Analysis

To determine the equilibrium dissociation constant, K_d, and the saturation SPR response, R_∞, the change in R_{eq} was plotted as a function of c_p. The data was then fit to a Langmuir isotherm (Figure 2.7). The basic assumptions of the Langmuir
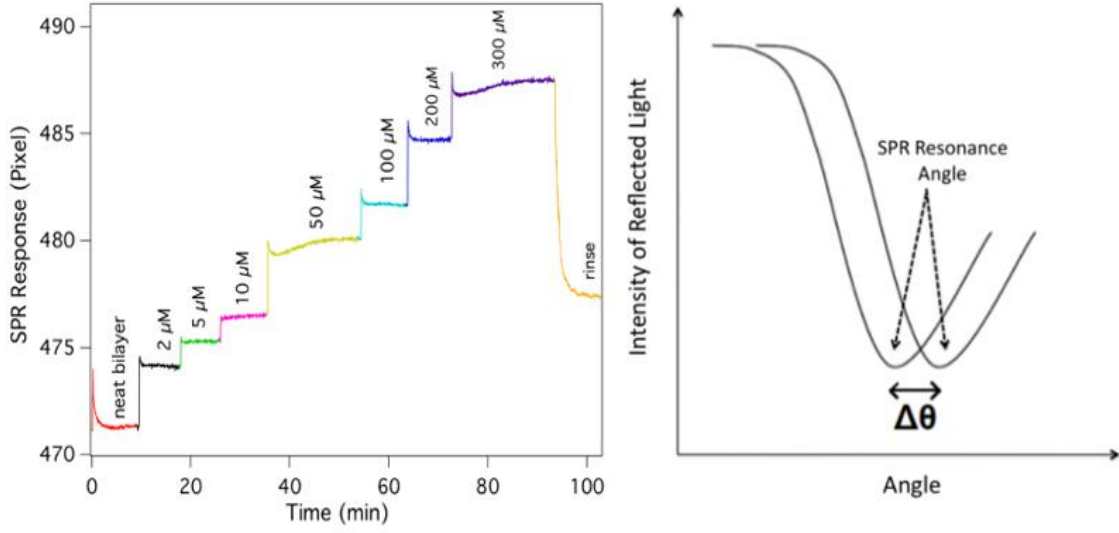
Figure 2.6: SPR Data Acquisition. The resonance angle is monitored as increasing concentrations of protein are added to the system. The right panel is an example SPR reflectivity curve where the minimum is the SPR resonance angle which shifts as the refractive index near the interface changes (protein binds). The left panel is an example titration curve which represents the change in SPR signal as a function of time as protein is added to the system.

isotherm are (1) one ligand molecule interacts with a single analyte molecule, (2) all binding sites are equivalent, and (3) all binding sites are independent of each other. The Langmuir binding model describes a 1:1 molecular interaction.

$$A + B \underset{k_{off}}{\overset{k_{on}}{\rightleftharpoons}} AB \tag{2.12}$$

In the case of protein/membrane binding, A represents the protein and B represents an area on the membrane that the protein binds. The rates of association and dissociation can then be written

$$\text{Association}: \frac{d[AB]}{dt} = k_{on}[A][B] - k_{off}[AB] \tag{2.13}$$

At equilibrium

$$\frac{d[AB]}{dt} = 0 \tag{2.14}$$

19
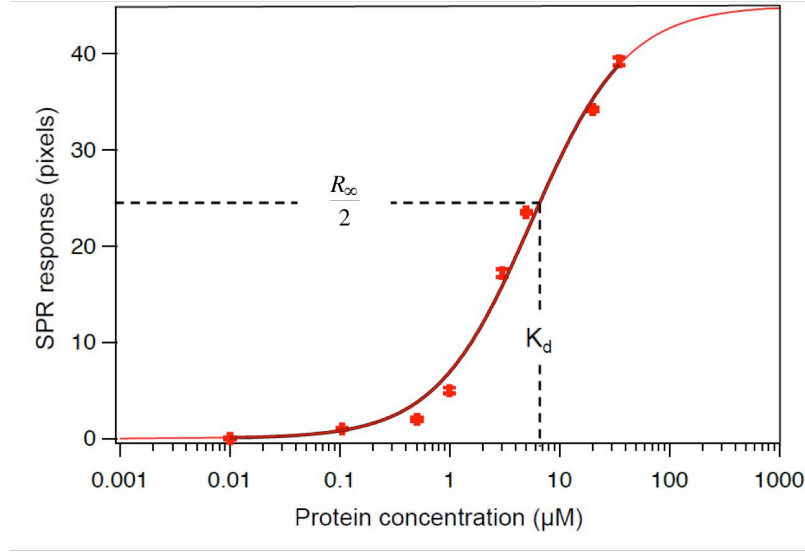
Figure 2.7: An Exemplary SPR Binding Curve. The equilibrium SPR response (the change in signal compared to the neat bilayer baseline) is plotted as a function of concentration. A Langmuir isotherm is used to fit the data and obtain the equilibrium dissociation constant K_d and the saturation response R_∞. K_d is the concentration at which half of the binding sites are occupied and the R_∞ is the SPR response when all binding sites are occupied.

Taking Eq. 2.13 at equilibrium and rearranging yields

$$k_{on}[A][B] = k_{off}[AB]$$

$$\frac{[AB]}{[A][B]} = \frac{k_{on}}{k_{off}} = K_a \text{ (equilibrium association constant)} \tag{2.15}$$

$$\frac{[A][B]}{[AB]} = \frac{k_{off}}{k_{on}} = \frac{1}{K_a} = K_d \text{ (equilibrium dissociation constant)}$$

If the concentration of the bound complex at saturation is given by $[AB]_{max}$ then

$$[B] = [AB]_{max} - [AB]$$

$$\tag{2.16}$$

$$\frac{d[AB]}{dt} = k_{on}[A]([AB]_{max} - [AB]) - k_{off}[AB]$$

And at equilibrium

$$k_{on}[A]([AB]_{max} - [AB]) = k_{off}[AB]$$

$$k_{on}[A][AB]_{max} = [AB](k_{off} + k_{on}[A])$$

$$\frac{k_{on}[A][AB]_{max}}{k_{off} + k_{on}[A]} = [AB] \tag{2.17}$$

$$\frac{[A] \cdot [AB]_{max}}{K_d + [A]} = [AB]$$

Given [AB] is proportional to the SPR response (R; at equilibrium R_{eq}), [A] is the protein concentration added to the system (c_p), and $[AB]_{max}$ is proportional to the saturation response (R_∞) the equation can be re-written to obtain

$$R_{eq} = \frac{R_\infty \cdot c_p}{c_p + K_d} \tag{2.18}$$

Bulk Corrections

To quantify low affinity interactions high protein concentrations are needed. This can impact the optical index, n, of the medium in contact with the sensor surface resulting in a signal increase. In the case of the stBLM system, the refractive index of the bulk aqueous buffer shifts due to the large concentration of protein in solution. In such cases, a correction should be applied to the SPR response that takes into account the contribution from the bulk. The bulk effect for each protein concentration can be estimated using $dn/dc \times \rho = \Delta n$ where dn/dc is the refractive index increment for protein, Δn is the change in refractive index, and ρ is the mass concentration of the protein (g/mL). For a pixel change of 1, $\Delta n = 6.3 \times 10^{-5}$.

2.4   Specular Neutron Reflection

2.4.1   Introduction

NR offers several competitive advantages for application to structural biology of membrane proteins compared to traditional structure determination methods. NR is non-destructive allowing for sample manipulation during a measurement. Therefore, biological processes can be simulated *in situ* by changing the environmental conditions, for example by adding molecular co-factors [59], and the evolution of the
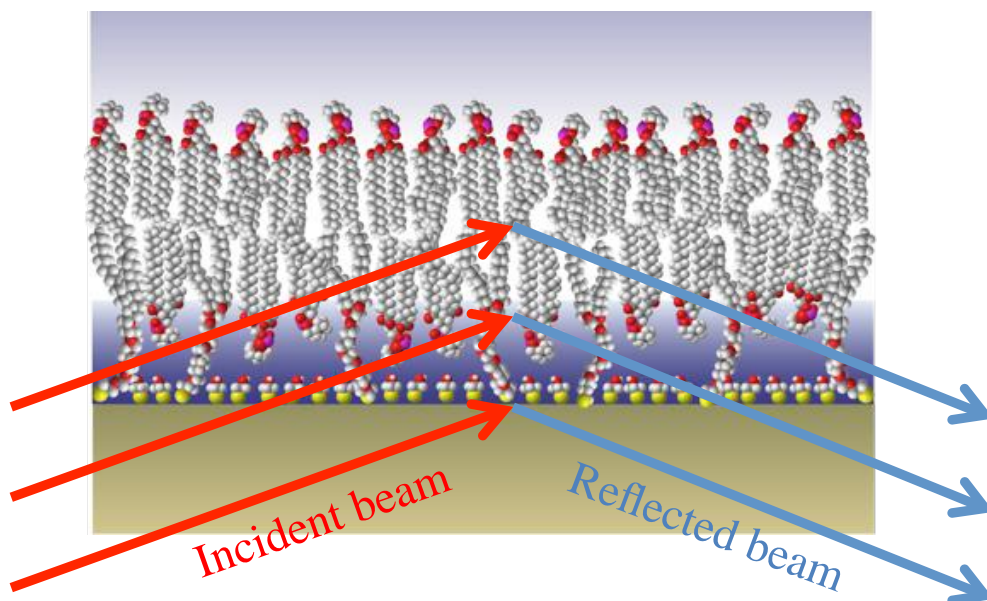
Figure 2.8: Illustration of specular neutron reflection at a stBLM interface. In NR a collimated beam of neutrons strikes the planar stBLM and the reflected intensity is measured as a function of angle.

system can be monitored. Specific isotope labeling of a subset of proteins that form protein-protein complexes on the membrane allows for the structural characterization of individual proteins within the complex [77, 78]. It is not necessary for the protein to be well-structured/folded which allows for the study of intrinsically disordered and partially unfolded proteins and peptides [79, 80], and peripheral membrane proteins that may only associate with the membrane transiently can also be measured [81]. Most importantly, proteins can be measured in a lipid environment as long as the model membrane system is planar, of low interfacial roughness [82], homogenous, and stable for long periods. stBLMs meet these criteria and with the implementation of molecular modeling strategies allow for the routine study of membrane-associated proteins. The result of an NR measurement applied to a protein/membrane system is a 1-dimensional compositional profile normal to the bilayer.

2.4.2 Theory

Since a detailed description of the theory and applications of NR can be found in standard textbooks [83], only a brief overview of the concepts will be given. In specular reflection the angle of incidence equals the angle of reflection (Figure 2.8),

and the momentum transfer occurs normal to the interface. The reflected intensity is measured as a function of the momentum transfer, q_z, which is given by

$$q_z = \frac{4\pi}{\lambda} sin(\theta) \tag{2.19}$$

In this equation z is the direction normal to the interface, λ is the wavelength of the collimated neutron beam, and θ is the incident and reflected angle. NR is sensitive to the refractive index profile normal to a surface, and the neutron refractive index of a medium is defined as

$$n = 1 - \frac{\lambda^2 N_d b}{2\pi} + \frac{i\lambda N_d \sigma_a}{4\pi} \tag{2.20}$$

N_d is the atomic number density, b is the coherent scattering length, and σ_a is the adsorption cross section. ρ is the neutron scattering length density (nSLD) given by

$$\rho = N_d b \tag{2.21}$$

σ_a=0 for most materials, thus

$$n \approx 1 - \frac{\lambda^2}{2\pi}\rho \tag{2.22}$$

For specular reflection θ_i=θ_r, and Snell's law gives the relation:

$$n_1 cos(\theta_1) = n_2 cos(\theta_2) \tag{2.23}$$

Total external reflection occurs below a critical angle given by Snell's Law:

$$cos\theta_c = \frac{n_2}{n_1} \tag{2.24}$$

For neutrons incident from air n_1=1, thus

$$cos\theta_c = n \tag{2.25}$$

with n=n_2. If θ_c is sufficiently small then the first term in the Taylor expansion can be used to approximate θ_c.

$$cos\theta_c = 1 - \frac{\theta_c^2}{2} \tag{2.26}$$

Then equations 2.22, 2.25, and 2.26 can be used to re-write θ_c using

$$n = 1 - \rho\frac{\lambda^2}{2\pi} = 1 - \frac{\theta_c^2}{2} \tag{2.27}$$

resulting in

$$\theta_c = \lambda \sqrt{\frac{\rho}{\pi}} \tag{2.28}$$

The critical neutron momentum transfer wave vector, q_c, is then given by

$$q_c = \frac{4\pi sin\theta_c}{\lambda} = 4\sqrt{\pi\rho} \tag{2.29}$$

Neutrons follow the same laws of reflection and refraction as electromagnetic waves with the electric vector perpendicular to the plane of incidence (s-wave). The reflectivity $R = R(q_z)$ is the ratio of the reflected and incident intensities. For reflection at a planar interface between two media R is given by Fresnel's law

$$R = \begin{cases} 1 & \text{if } \theta \leq \theta_c \\ |r|^2 & \text{if } \theta \geq \theta_c \end{cases} \tag{2.30}$$

$|r|$ is the reflection coefficient

$$|r|^2 = rr^* = \left| \frac{n_1 sin\theta_1 - n_2 sin\theta_2}{n_1 sin\theta_1 + n_2 sin\theta_2} \right|^2 \tag{2.31}$$

The result that R is the square of a complex quantity shows that the phase information is lost when measuring the reflectivity.

Reflection from Multiple Layers

The reflected intensity from multiple layers is the result of interference from reflections at all interfaces in the system (Figure 2.9). For a sample that contains m discrete (smooth) layers with a semi-infinite 0th layer and a semi-infinite $(m+1)^{th}$ substrate layer the reflectivity amplitude between layers $(m-1)$ and m is given by

$$r'_{m-1,m} = \frac{r_{m-1,m} + r_{m,m+1}e^{2i\beta_m}}{1 + r_{m-1,m} \cdot r_{m,m+1}e^{2i\beta_m}} \tag{2.32}$$

with

$$\beta_m = \frac{2\pi}{\lambda}n_m d_m sin\theta \tag{2.33}$$

$$r_{i,j} = \frac{n_i sin\theta_i - n_j sin\theta_j}{n_i sin\theta_i + n_j sin\theta_j} \tag{2.34}$$

24
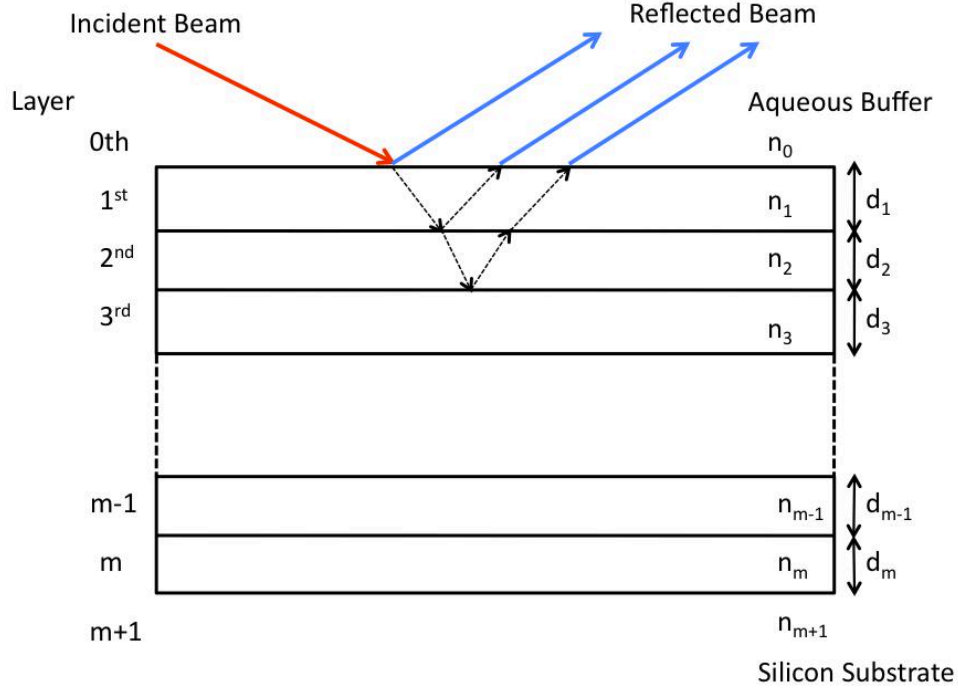
Figure 2.9: Reflectivity from a layered material. A slab view of a multilayer sample consisting of m layers of thickness d_i and refractive index n_i. The incident beam will be reflected (and refracted) at the interfaces between each of the layers. The measured intensity is the result of the interference from all the reflections.

d_m is the thickness and n is the refractive index of layer m. r is determined by first calculating the reflected amplitude between the bottom two layers $(r_{m+1,m})$. The resulting value is then recursively used to calculate $r_{m,m-1}$ and so forth until $r_{0,1}$ is evaluated, which eventually provides the reflectivity of the sample using $R = rr^*$.

2.4.3   Instrumentation

NR measurements were performed at the NIST Center for Neutron Research (Gaithersburg, MD) using the the NG7 horizontal (λ=4.75 Å) and CGD Magik (λ=5 Å) reflectometers [84]. A schematic of the reflectometer set-up is shown in Figure 2.10. During the reflectivity measurement the angle of the incident beam is varied, and a q_z range of 0.01 to 0.250 Å^{-1} was used. stBLMs were formed on gold-coated ($\sim$15 nm) SAM-covered silicon wafers and assembled in a flow cell. The flow cell allowed for *in situ* changes in environmental conditions [85], such as change in buffer from H_2O to D_2O for isotopic contrast [86], while measuring the same footprint on the sample for all conditions. The flow cell was maintained at room temperature.
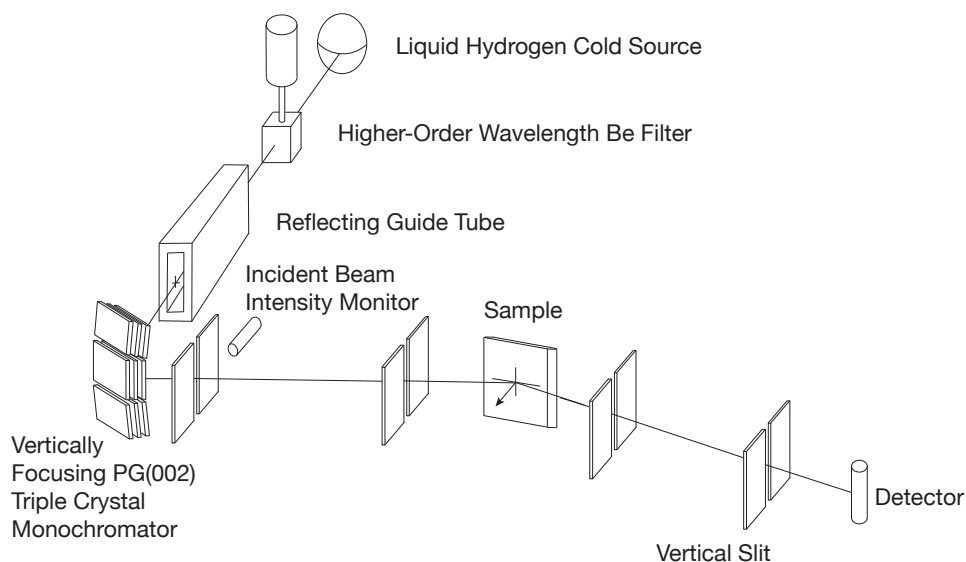
Figure 2.10: Schematic of a Typical Neutron Reflectometer. This schematic illustrates a typical instrument set-up for non-polarized measurements at a steady state source where a single crystal monochromator is used to obtain a quasi-monochromatic beam of neutrons.

2.4.4 Data Acquisition

NR data for the stBLM was sequentially collected in D_2O and H_2O to characterize the bilayer before adding protein. Buffer exchange was accomplished by flushing $\sim$10 mL of buffer through the cell (volume $\sim$1.3 mL) using a syringe either manually or with a pump. Protein at the desired concentration and volume ($\sim$1.5 mL) was introduced to the NR cell manually via a syringe. Protein measurements were conducted two ways: the incubation of the protein with the stBLM in two contrasts (H_2O and D_2O) was measured followed by a rinse measurement in both contrasts or the protein was incubated with the stBLM in H_2O buffer for typically 1 hr followed by rinse measurements in both contrasts. The incubation measurements detect all protein that at the bilayer interface while the rinse measurements detect any remaining, tightly bound protein. Adequate counting statistics, such as those exemplified in Figure 2.11, were obtained for each measurement (neat bilayer, protein incubation, rinse in each contrast) after 5-7 hrs.

2.4.5 Data Analysis

The aim of the NR data evaluation is to determine a unique compositional profile along the membrane normal that accounts for all the molecular components of the
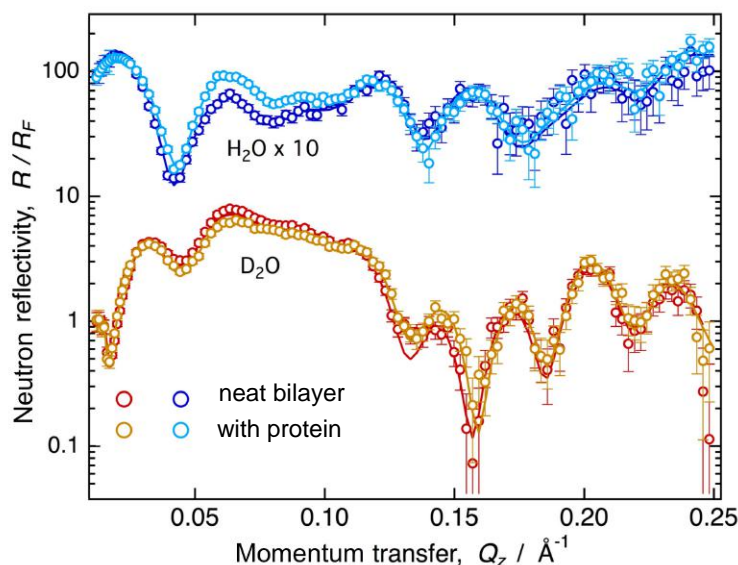
Figure 2.11: NR curves normalized by the Fresnel reflectivity. The data shows an stBLM before and after protein addition. Each condition was characterized using two isotopically distinct bulk solvents (H_2O and D_2O) using *in situ* buffer exchange. (Reproduced from R. Eells, M. Barros, K.M. Scott, I. Karageorgos, F. Heinirch and M. Lösche (2017) Biointerphases 12, 02D408 with the permission of AIP Publishing).

interfacial architecture, which includes the lipid bilayer and any membrane associated protein, peptides, or small molecules. All reflectivity curves from one sample measured under a range of conditions (neat bilayer and protein measurements in all contrasts) are co-refined, which allows the compositional profile to be determined with high confidence, particularly in the solvent containing regions [85], and allows for a precise quantification of the changes in interfacial structure as a result of protein association with the membrane.

The one-dimensional nSLD profiles along the membrane normal were typically parameterized using a stratified slab model for the solid substrate [87], a continuous distribution model for the stBLM [88], and a monotomic Hermite spline for the model-free protein distribution [57] (Figure 2.12). Individual slabs were used for the bulk silicon, silicon oxide, chromium and gold layers. For each layer, the fit parameters are the thickness and nSLD, except for the bulk silicon for which the nSLD is known. For the continuous distribution model of the stBLM the sub-molecular groups implemented were: βME, tether PEG chains, tether glycerol groups, inner and outer lipid headgroups, inner and outer lipid methylene chains, and lipid and tether methyl groups. The bilayer hydrocarbon thickness for each leaflet, bilayer completeness, tether surface density, tether thickness, and βME surface density were
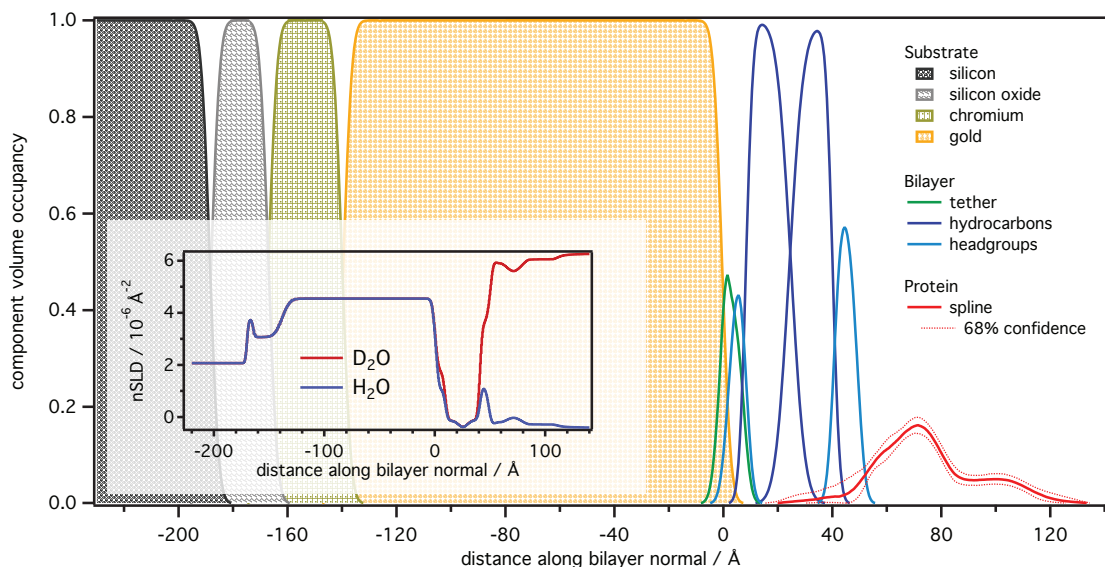
Figure 2.12: Schematic for a hybrid real-space model. The hybrid model combines a traditional slab model for the substrate layers with a composition space model for the lipid bilayer and protein. The lipid bilayer was constructed using a continuous distribution model, and the protein was modeled using free-form Hermite splines. Volume that is not filled with either substrate layers or molecular components is taken up by bulk solvent. The inset shows the nSLD profile calculated from the real-space model assuming H_2O and D_2O based solvents.

all determined from the fit. For a defect-free membrane the bilayer completeness is 100%. Two roughness parameters are applied to the system: one to describe the substrate and one to describe the bilayer. Data modeling and optimization of the model parameters were performed using the ga_refl and Refl1D software packages developed at the NCNR [85].

Composition Space Modeling: The Continuous Distribution Model

Although the phase information is lost, preventing direct data inversion, robust modeling strategies have been developed for structures that are approximately known that circumvent this problem. To extract structural information on membrane-bound proteins from NR measurements we use a molecular scale description of the system paired with well-determined confidence limits on the model parameters via a composition space model that uses error functions to model the continuous distributions of molecular components ("continuous distribution model") [88]. Importantly, the composition-space model allows for spatial overlap between molecular distributions instead of a sharp demarcation between components as in the slab model. The con-

28
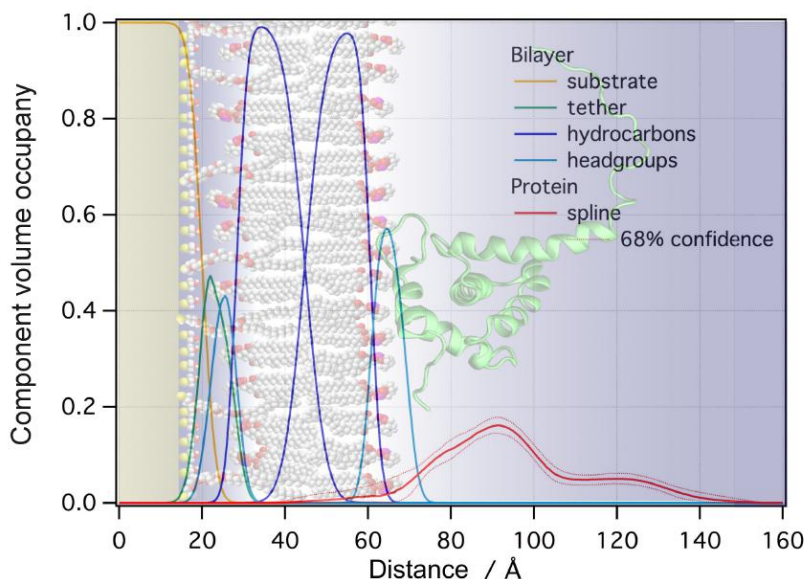
Figure 2.13: CVO profiles for a protein/stBLM complex. The CVO profiles for the stBLM structure and membrane-associated protein were obtained by composition space modeling. The background image visualizes the mostly likely protein orientation, as determined by rigid body modeling using the NMR structure in PDB entry 2H3F, on the stBLM surface. (Reproduced from R. Eells, M. Barros, K.M. Scott, I. Karageorgos, F. Heinrich and M. Lösche (2017) Biointerphases 12, 02D408 with the permission of AIP Publishing).

tinuous distribution model yields component volume occupancy (CVO) profiles of the molecular and sub-molecular groups (Figure 2.13), and this model has been validated for lipid bilayer membranes by comparing distributions of sub-molecular fragments with those obtained from MD simulations [57].

The continuous distribution model integrates auxiliary information such as molecular volumes and chemical connectivity to reduce the number of fit parameters and increase the precision and confidence with which molecular components are localized within the sample. For example, in the stBLM the CVOs of the headgroups are tied to those of their respective hydrocarbon chains since the individual volumes for these two components are known from auxiliary methods, such as X-ray diffraction [89] or MD simulation [90]. As a result, besides the parameters for the tether molecules, only three parameters are required to describe all the submolecular groups of the lipid bilayer: thickness of the hydrocarbon chains for two independent leaflets and the bilayer completeness. The headgroup thicknesses are typically too small to be reliably determined with NR and fixed values obtained from other methods, such as molecular dynamics simulations, are used instead.

2.4.6 Modeling CVO Envelopes for Membrane-Associated Proteins

CVO profiles of unknown shape, such as those of membrane-associated proteins for which molecular structures or orientations are unknown, require free-form models. In our approach, Hermite splines are used that accurately describe arbitrary protein profiles that can be easily joined with CVO profiles of the molecular constituents of the lipid bilayer to build a consistent protein/lipid bilayer complex [57] (Figure 2.13). A constant nSLD representation of the average nSLD of the protein, taking into account proton exchange with the bulk solvent, is used for the entire spline. The Hermite spline is defined by control points located, on average, 15 Å apart. The number of control points is determined by the extension of the protein along the membrane normal and is iteratively refined during model optimization. Two fit parameters are used for each control point: the volume occupancy of the envelope and the deviations from an equidistant separation of the control points. By allowing the control points to deviate, to some extent, from their equally spaced center positions on z maximizes the flexibility of the Hermite splines.

2.4.7 Uncertainty Analysis

Surface structures in biological NR require a large number of parameters to model due to their complexity. Therefore, rigorous methods are needed to determine the parameter uncertainties and avoid over-parameterization. We currently use a Monte Carlo Markov Chain global optimizer [85] that yields reliable confidence intervals and provides access to the full posterior parameter distribution from which parameter correlations can be obtained that are useful for model optimization. Uncertainties can also be determined for properties that depend on parameter combinations, such as the area per lipid for the bilayer lipid membrane. This allows the confidence bands on the free-form profiles to be determined as well.

2.4.8 Control Fit

Control fits are used to estimate systematic errors that may occur when modeling the NR data. These systematic errors can be a result of issues with the measurement or the model may have deficiencies in describing the interfacial structure. The control fit is the equivalent of the co-refinement of the neat bilayer and protein measurements, but the protein data set is replaced with data from the neat bilayer. The fit now contains two identical data sets. However, for the second data set the model has the option to place "protein," which means any systematic errors manifest as protein. Ideally no protein should be present in the control fit.

Integrative Modeling of Interfacial Structures

NR is intrinsically a low resolution technique providing only 1D-structural profiles. To determine high resolution 3D information of membrane-bound proteins that are consistent with the 1D profiles, integrative modeling strategies are needed. We routinely integrate crystallographic and NMR structures into the refinement of the NR data [57,60,61] by slicing the protein structure(s) in the PDB file into slabs, typically of thickness 0.5 Å, along the membrane normal. For each slab the cross sectional area and scattering length are determined. The scattering length is calculated by adding the coherent cross sections [91] of all atoms of the protein that fall within the slab. The cross-sectional area can be determined by calculating the solvent accessible volume of the protein [92, 93] and slicing it using the same sequence of slabs, or can be derived from experimentally determined average volumes per amino acid, such as those from SANS contrast matching experiments [94]. The computationally generated model profile(s) can be compared to the free-form profile (obtained from fitting the NR data) to determine whether the protein undergoes reorganization upon membrane binding.

If the protein does not undergo major changes within the resolution of NR, the orientation of the high-resolution protein structure can be varied with respect to the membrane (rigid body modeling) to determine the orientation of the protein on the membrane. The protein orientation is defined by two Euler angles, β and γ. The third angle is irrelevant since NR is invariant against rotational symmetry around the z-axis. Orientations (β, γ) are obtained by extrinsic rotations of the protein around the axes of the bilayer coordinate system, first by $0° \leq \gamma \leq 360°$ about the membrane normal then by $0° \leq \beta \leq 90°$ around the x-axis in the plane of the membrane. The initial orientation of the protein ($\beta=0$, $\gamma=0$) is the one provided by in the PDB file. A probability plot consistent with the NR data is generated and used to determine the most likely orientation of the protein in its membrane bound form. If conformational changes are evident based on the comparison of the free-form and modeled profiles, additional modeling using molecular dynamics or Monte Carlo simulations of the membrane-bound protein are needed. While we have started using simulation-based integrative modeling strategies [21, 61, 79, 95], a complete integrative framework for NR has not yet been established.

Chapter 3

Methodology: Development of a Complex stBLM to Mimic the Inner Leaflet of the Plasma Membrane

Model membranes seek to capture the biophysical properties of cellular membranes while reducing the complexity to a controlled number of components. In terms of the stBLM system, compositions containing two or three lipid components have been essential for systematically probing the interactions that drive protein/membrane association. However, to bridge the gap to complementary studies in a cellular context, stBLMs that more closely mimic the lipid compositions found in cellular membranes are desirable. Here we developed an osmotic shock vesicle fusion method to prepare complex stBLMs that mimic the inner leaflet of the plasma membrane.

3.1   Introduction

On the most basic level, lipid membranes define the boundaries of a cell and its internal organelles. However, cellular membranes, along with membrane-associated proteins, have an active and essential role in many cellular processes. The composition of lipid membranes vary between different cell types and between the organelles within a cell [102]. Membrane organization is dynamic in order for cellular processes, such as cell signaling and trafficking, to occur and be controlled [102]. While the complexity of cell membranes is essential for their function, it poses experimental challenges for understanding the specific molecular mechanisms that drive membrane attraction; for example, the binding of a peripheral membrane protein to its target membrane. In order to systematically probe these interactions model membranes—which reduce the complex cellular membrane to a limited number of components but maintain the key elements needed for the interactions of interest to occur—are an important tool.

A variety of model membranes have been developed that seek to capture the biophysical properties of cellular membranes. These model membranes include free-standing, tethered, and supported membranes in vesicle, nanodisc, and planar bilayer forms. In terms of geometry, planar membranes allows for the utilization of surface characterization techniques such as quartz crystal microbalance with dissipation (QCM-D) and atomic force microscopy (AFM) [113–115], SPR and EIS [68, 115], and NR [63–65]. Free standing planar bilayers, such as black lipid membranes, offer advantages in terms of incorporation of membrane proteins, but these bilayers are not stable long term [111, 112]. To obtain long term stability some form of support structure is needed. Solid supported lipid bilayers, in which the bilayer is formed on a substrate, offer advantages in terms of robustness and stability. However, a major disadvantage of this system is that the supported membrane is not decoupled from the underlying substrate. The proximity to the substrate can lead to a loss in mobility and function of both transmembrane [111, 112] and peripheral membrane proteins [112]. In addition, lipid-solid substrate interactions can result in reduced lipid mobility and modified phase behavior [116]. Addressing those challenges, a variety of model membrane systems have been developed that decouple the lipid membrane from the solid substrate using a range of small molecule and polymer based surface chemical approaches [54, 117–121].

To be useful for biological NR a model membrane system has to meet several criteria. As a technical requirement it needs to be planar, of low interfacial roughness, long-time stable, and homogenous over a large sample area (cm^2). High interfacial roughness and a curved interface negatively affect the effective resolution of the measurement [82]. Due to the relatively low flux at current neutron sources, long measurement times (amounting to several hours per condition) are needed, thus a membrane system that is long-time stable is required. For the same reason, large sample sizes are advantageous as they make better use of the neutron beam. Homogenous samples are required primarily to ensure a unique analysis of the NR data. Inhomogeneous bilayers, even on length scales below the coherence of the neutron beam, require a more complex modeling and therefore lower the certainty with which structural features of interest can be determined. For example, a high density of defects in the lipid bilayer constitutes a significant disadvantage for the structural characterization of membrane-associated proteins.

For biological relevance a model membrane has to be representative of a lipid membrane *in vivo* and is ideally accessible to buffer and protein exchange during the measurement. A flexible model membrane system supports a wide range of relevant lipid compositions while maintaining lipid diffusion rates that are comparable to biological membranes. It should also be structurally inert towards changes in environmental conditions, such as temperature, ionic strength, and pH, to help retain a focus on structural changes induced by protein membrane-association. stBLMs, introduced in Chapter 2, meet these criteria and have been optimized for NR experiments [63–65].

A standard technique for bilayer formation on tethered systems is rapid solvent exchange (RSE) where a functionalized substrate is incubated with lipids dissolved in an organic solvent, such as ethanol or methanol, followed by rapid replacement of the solvent by aqueous buffer [63, 67]. stBLMs formed by RSE that consist of one or two lipid components have been well characterized and found to be both defect-free and highly reproducible [63–65]. However, an increased number of components leads to more defect-rich membranes. In addition, since individual lipid components are dissolved in the organic solvent, the lipid composition in the solvent might not translate to the composition of the prepared membrane (unpublished data). Both deficiencies are likely due to different solubilities of distinct components in the organic solvent used for RSE.

Fusion of lipid vesicles to tether molecule SAMs has long been considered as an alternative to RSE that provides a better controlled process for membrane preparation but was previously found to yield lipid bilayers with higher defect density in comparison to RSE [63, 122]. Planar membrane formation by vesicle fusion can be aided using osmotic stress [116, 123], and exposing lipid vesicles to a higher external salt concentration before fusing to a SAM of lipopolymers yielded more homogenous lipid bilayers as probed by AFM [116]. In the method we use, an initial exposure of the SAM to vesicles prepared in high salt aqueous buffer solution is followed by a slow rinse with low salt buffer. The difference in ionic strength between the buffer solutions promotes vesicle rupture and bilayer completion via osmotic stress/shock and results in electrochemical properties equivalent to those formed by RSE.

In our group most studies of protein-membrane interactions with stBLMs have been conducted using compositions consisting of two or three lipid components with the aim to capture the essential features of a lipid membrane relevant for the biological context. These simple mixtures have been key for characterizing the interactions that drive membrane binding for a variety of membrane-associated proteins and determining the structures of the proteins in their membrane-bound form(s) [21, 24, 81]. However, in order to bridge the gap to complementary studies in a cellular context, solid supported membranes that more closely mimic the lipid compositions found in cellular membranes are desirable. Here we report the development of an osmotic shock vesicle fusion (OSVF) method to prepare complex stBLMs that mimic the inner leaflet of the PM while still fulfilling the discussed requirements of a model membrane system.

3.2 Methods

3.2.1 Liposome Preparation

The lipid films were hydrated with a range of salt concentrations, 0.05 M to 2 M NaCl with 10 mM $NaPO_4$ at pH 7.4, for the OSVF optimization. For all PE-containing stBLMs the vesicle internal buffer was 2 M NaCl, 10 mM $NaPO_4$ at pH 7.4.

3.2.2   Preparation of stBLMs

The system was rinsed with a low ionic strength buffer, 50mM NaCl, 10mM NaPO$_4$ pH 7.4, to complete stBLM formation regardless of the salt concentration used for vesicle formation.

3.3   Results and Discussion

3.3.1   Ionic Strength Dependence of Anionic stBLMs

Anionic lipid species play an important role in driving protein-membrane interactions through electrostatic attraction and are represented at the inner leaflet of the PM at approximately 25-30% based on studies of human erythrocytes [23,124,125]. However incorporating anionic lipids in stBLMs while retaining a low defect density using RSE is challenging [64]. Therefore, a binary DOPC:DOPS mixture was chosen to optimize salt concentrations for the OSVF method before moving to mixtures with more components. Other parameters that are commonly manipulated for supported lipid bilayer formation using vesicle fusion are summarized in [123] and include vesicle size, vesicle concentration, temperature, and buffer pH.

Table 3.1: Capacitance and Resistance Values of 30:70 DOPS:DOPC stBLMs Formed with Increasing Differences in Salt Concentration

Formation Salt Concentration	Capacitance (μFcm^{-2})	Resistance (kΩcm^2)
50 mM NaCl*	$\approx$ 9.1	< 0.17
250 mM NaCl*	0.98	17.45
500 mM NaCl*	0.87	84.76
1 M NaCl*	0.92	185.6
2 M NaCl	0.9	3441.9

Measurements denoted with * were collected by Dr. Marilia Barros

stBLMs were formed via OSVF using 70:30 DOPC:DOPS vesicles prepared in buffer from 50 mM to 2 M NaCl and incubated on SAM-covered gold-coated slides for 2 h. The system was then rinsed with low ionic strength buffer (50 mM NaCl), and the quality of the bilayer was assessed. Greater differences in ionic strength between the internal and rinse buffers resulted in better stBLM completion and higher resistances based on EIS (Table 3.1). When the vesicle and rinse buffers both contained 50 mM NaCl the electrical impedance spectra resembled that of a SAM indicating, at best, a highly defective bilayer. At an internal ionic strength of 250 mM the characteristic stBLM spectra was observed. However, the long tail at low frequencies in the Cole-Cole plot implies a low resistance to ion mobility and, therefore, a large defect denisty.
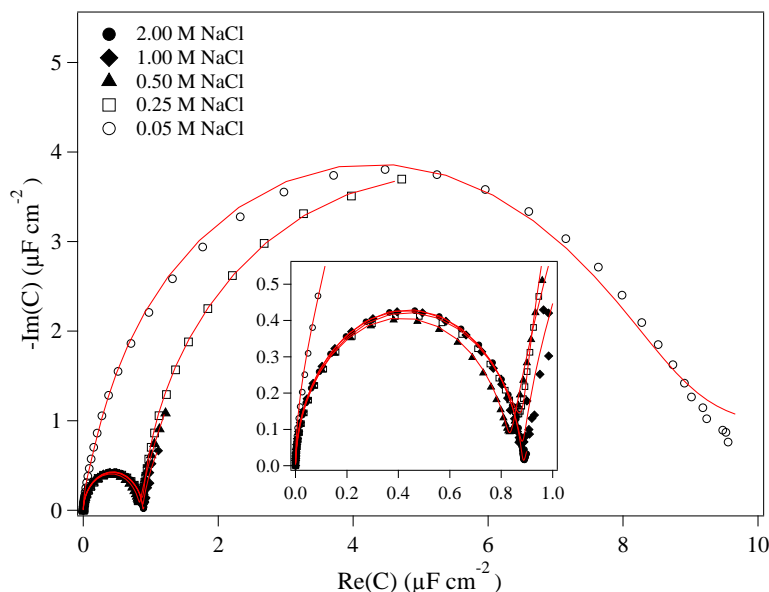
Figure 3.1: Cole-cole plots of 70:30 DOPC:DOPS stBLMs prepared at different ionic strengths. The ionic strength used for vesicle formation was increased from 50 mM to 2 M NaCl while the rinse buffer was held at 50 mM NaCl. Osmotic shock resulted in more complete, highly insulating stBLMs, which is qualitatively reflected in the Cole-Cole plot by the closeness to the x-axis and a short tail at high frequencies. The inset is zoomed in to highlight the spectra for the optimized 1 and 2 M NaCl conditions.

A highly insulating bilayer was formed at 500 mM NaCl with low defect density. Increasing the ionic strength to 1 M and 2 M NaCl improved the bilayer with almost no tail present for the 2 M NaCl condition (Figure 3.1).

3.3.2 Developing a stBLM Mimic of the Inner Leaflet of the PM

Incorporating PE into stBLMs

The mammalian inner leaflet of the PM contains >50% zwitterionic lipids with PE as the primary lipid at ∼40% followed by PC at a level of ∼14% in human erythrocyte membranes [23, 124, 125]. Even though PC is not the primary neutral lipid in the inner PM, it is easily incorporated into planar model membranes. Therefore, PC is a widely used lipid in artificial model membranes. PE can be more difficult to incorporate into planar bilayer systems due to its small headgroup size [102, 126] that can promote negative curvature in membranes [127] depending on temperature and chain saturation. To test the extent to which a curvature-promoting lipid such as PE
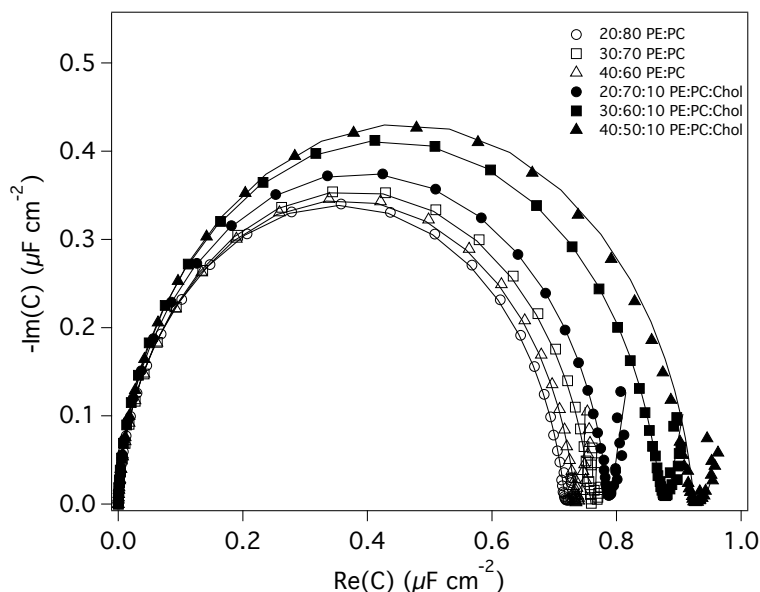
Figure 3.2: Cole-Cole plot of EIS data and fit for PE:PC and PE:PC:Cholesterol stBLMs formed with OSVF. The amount of PE was increased from 20 mol% to 40 mol%. The cholesterol was held at 10 mol%. The internal buffer salt concentration was 2 M NaCl and the rinse buffer salt concentration was 50 mM NaCl. This data was collected by Chris Kervick (without cholesterol) and Dennis Michalak (with cholesterol).

can be incorporated into stBLMs, for which a planar geometry is imposed by a solid support, simple zwitterionic stBLMs containing DOPC and DOPE were tested. The effect of cholesterol on PE-containing stBLM formation was also tested by including cholesterol in the PE:PC mixtures. Cholesterol has been found to destabilize PE and PE:PC bilayers and induce non-planar geometries [128] so it was important to test if defect-free stBLMs could be formed using mixtures that contain PE and cholesterol. stBLMs could be readily produced with these simple mixtures based on qualitative features, such as length of the low-frequency tail, semi-circular shape, and distance from the x-axis (Figure 3.2). However, the standard ECM model [63] did not describe the data well.

Incorporating anionic lipids into PC/PE/cholesterol stBLMs

In addition to being enriched in PE, the inner leaflet of the PM is also enriched in anionic phosphatidylserine (PS) compared to other cellular membranes [102, 129]. PS is involved in protein targeting to the PM and drives membrane association through non-specific electrostatic interactions, as well as selective interactions, for example with C2 domains [130]. Consequently, mixtures of DOPE, DOPC, DOPS, and cholesterol
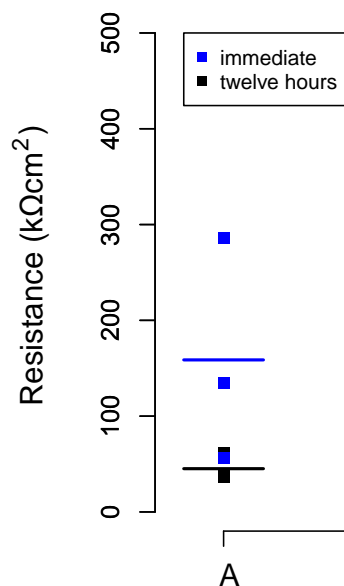
Figure 3.3: Resistance values for PE:PC:PS:chol stBLMs. Three measurements were taken for each condition immediately after stBLM formation (blue) and 12 hrs later (black). The resistance values have been normalized for the surface area of the measurement well. All stBLMs contained 20 mol% PS and 30 mol% Chol with (A) 20 mol% DOPE, 30 mol% DOPC (B) 20 mol% DOPE, 20 mol% DOPC, 10 mol% DMPC (C) 20 mol% POPE, 20 mol% POPC, 10 mol% DMPC (D) 30 mol% POPE, 14 mol% POPC, 6 mol% DMPC. The points represent the individual measurements and the lines represent the average.

were tested for stBLM formation. Physiologically relevant levels of PE (40 mol%), PS (20 mol%), PC (10 mol%) [23] and cholesterol (30 mol%) did not form defect-free lipid bilayers (data not shown). Lowering the content of DOPE to 20 mol% while increasing the content of DOPC yielded membranes of high resistance, however, the resistance decreased dramatically over a 12 h time period indicating these stBLMs are not stable (Figure 3.3). Stable membranes of higher DOPE content were achieved when adding a small fraction ($\leq$ 10 mol%) of saturated DMPC to the mixture. Inclusion of DMPC resulted in the formation of defect-free and stable stBLMs even when PE was the main zwitterionic lipid (30 mol%) with both dioleoyl and the more physiologically relevant palmitoyl-oleoyl tails (Figure 3.3). The amount of DMPC was further reduced, since inclusion of a fully saturated lipid is not as biologically relevant for the inner leaflet of the PM, to obtain an optimized complex PE composition that contains 30 mol% PE, 19.5 mol% PC, 0.5 mol% DMPC, 20 mol% PS, and 30 mol% cholesterol (Figure 3.4) with an average resistance of $\sim$1000 kΩcm^2.
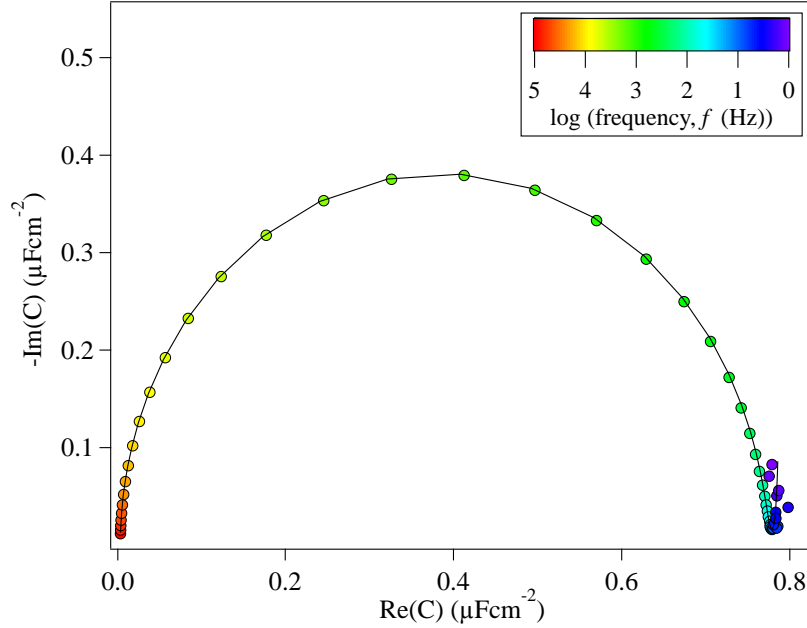
Figure 3.4: Cole-cole plot of EIS data and fit for the optimized PE-based stBLM. The stBLM was formed by vesicle fusion using an internal salt concentration of 2 M NaCl and rinse salt concentration of 50 mM NaCl. The optimized composition contained 30 mol% PE, 19.5 mol% PC, 0.5 mol% DMPC, 20 mol% PS, and 30 mol% cholesterol, and a representative stBLM formed using palmitoyl-oleoyl lipids is shown.

Table 3.2: Capacitance and Resistance Values for the PM mimic formed with dioleoyl and palmitoyl-oleoyl lipids

stBLM Composition	Time Point	Capacitance (μFcm^{-2})	Resistance (kΩcm^2)
dioleoyl PM mimic	Immediate	0.69 ± 0.04	2964 ± 895
	12 h	0.65 ± 0.02	3393 ± 336
palmitoyl-oleoyl PM mimic	Immediate	0.67 ± 0.06	1856 ± 380
	12 h	0.68 ± 0.06	2884 ± 882

The PM mimic, 27 mol% PE, 19.5 mol% PC, 0.5 mol% DMPC, 20 mol% PS, 2 mol% PI, 1 mol% PI(4,5)P$_2$, and 30 mol% cholesterol, was formed using either dioleoyl (DO–) or palmitoyl-oleoyl (PO–) lipids.

Phosphoinositides (PIPs) are anionic phospholipids that are present in minor amounts in eukaryotic cellular membranes. They are important for targeting of membrane-associated proteins since each cellular membrane is enriched in characteristic phosphoinositides specific to that membrane [131, 132]. The inner leaflet of the plasma membrane contains phosphotidylinositol (PI) and phosphatidylinositol-4,5-

bisphosphate ($PI(4,5)P_2$) present at ~1.2% [23,133] and ~1.4% [133], respectively, in human erythrocyte membranes. Proteins that target the PM often bind specifically to $PI(4,5)P_2$ [134] making it an important lipid to include in a PM mimic model membrane. PI and $PI(4,5)P_2$ were added to the optimized membrane composition in small quantities while reducing the amount of the PE resulting in a composition of 27 mol% PE, 19.5 mol% PC, 0.5 mol% DMPC, 20 mol% PS, 2 mol% PI, 1 mol% $PI(4,5)P_2$, and 30 mol% cholesterol for the PM mimic. Both dioleoyl and palmitoyl-oleoyl lipids resulted in the formation of complete stBLMs as indicated by the high resistances (Table 3.2). The resistances of these membranes were so high that the low frequency tail was absent, and the ECM could not describe the defects since essentially there were no defects.

3.4 Conclusions

We used an osmotic shock vesicle fusion method for stBLM formation to develop model membrane mimics for the inner leaflet of the PM. stBLMs were developed with PE as the majority lipid species and relevant mol% of PS and cholesterol. These PE-based stBLMs exhibited high resistances, which indicates a low density of defects. To achieve stability over time a small mol% of saturated lipid, DMPC, was included in the membrane. The relevant phosphoinositides, PI and PIP_2, were added to the optimized PE mixture to form the PM mimic. Complex (four or more components) stBLMs, such as the PM mimic, allow us to examine how membrane properties as a whole influence membrane/protein interactions which complements measurements conducted using two to three-component stBLMs that probe individual interactions (electrostatic, hydrophobic, specific).

Chapter 4

Membrane Association of myrMA

For HIV-1, and other retroviruses, capsid formation of the daughter virus requires trafficking of the Gag polyprotein to the plasma membrane. Membrane targeting of the Gag polyprotein is driven by a myristoylated N-terminal domain—MA (matrix). This chapter focuses on method development with applications to the study of the membrane-association of HIV-1 Gag MA. In this chapter we discuss the application of NR to determine the membrane-bound structure of myristoylated MA, focusing on the challenges associated with studying a protein that utilizes multiple motifs for membrane binding. We then reveal the structural organization of myrMA on charged membranes and compare it to the previously determined membrane-bound structure of –myrMA. Finally we report the effect of a PE-containing membrane mimic on myrMA binding affinity.

Text and figures in this chapter are reproduced from R. Eells, M. Barros, K.M. Scott, I. Karageorgos, F. Heinirch and M. Lösche (2017) Biointerphases 12, 02D408 with the permission of AIP Publishing.

4.1   Introduction

The Gag polyprotein is the structural factor essential for capsid formation of the nascent daughter virus of HIV-1 and other retroviruses [11]. Expressed in the infected host cell, capsid formation of the daughter virus requires Gag trafficking and binding to the PM, interactions between neighboring Gag proteins, and the binding of the viral RNA genome. To perform these functions HIV-1 Gag contains four major structural domains from the N-terminus to the C-terminus: MA, capsid (CA), nucleocapsid (NC), and p6, as well as connecting spacer peptides [12]. Membrane targeting of Gag is mediated by the myristoylated N-terminal MA domain. In solution –myrMA adopts a compact globular fold with the N-terminal consisting of 5 α helices while the C-terminal is more flexible (Figure 4.1) [18, 96–99]. The myristoylated protein contains 129 residues (Glycine 2 to Tyrosine 130; following removal of the N-terminal methionine during the myristoyl attachment process [100]) with residues 10-16 forming helix I, 31-41 forming helix II, 54-64 forming helix III, 73-89 forming helix IV, and 97-112 forming helix V [18]. Myristoylation does not result in large conformational
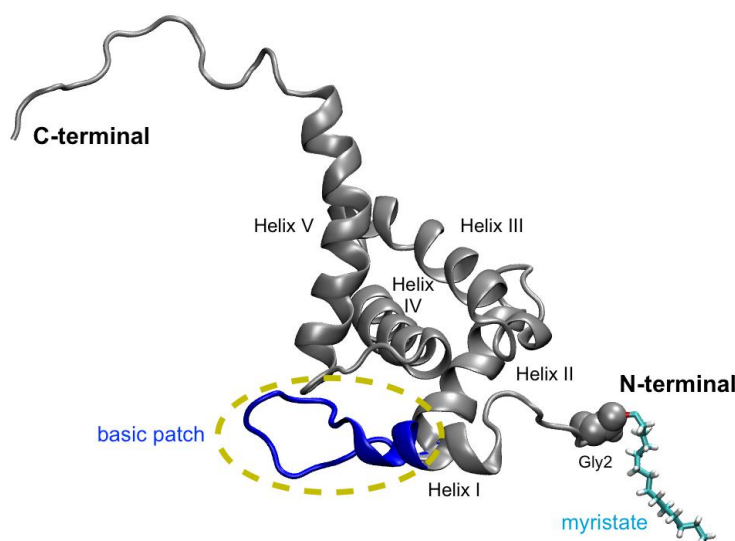
Figure 4.1: Solution structure of MA. In solution MA adopts a compact globular fold consisting of 5 α helices and a flexible C-terminal. Two motifs used in membrane interactions are highlighted: the basic patch (dark blue) and the myristate (in cyan), which was added to the protein structure to highlight its location. The image was rendered in VMD using PDB 2H3F (a solution NMR ensemble of –myrMA [18]).

changes even though the protein can adopt two states in which the myristate is either sequestered or exposed to the cytosol. Based on NMR, residues 3-18 exhibit spectral differences between the two states which are the result of minor structural differences in the first loop (residues 3-9) and helix I (residues 10-18) [18, 101].

MA recognizes specific components of the PM and binds to the membrane surface by several physical interactions. The myristate group serves as a hydrophobic anchor [13–15] while a conserved patch of basic residues (highly basic region (HBR); residues 15-31) interacts electrostatically with anionic lipids in the inner leaflet of the PM [14,16,17]. The HBR contains 5 lysine residues (K15, 18, 26, 27, and 30) and two arginine residues (R20 and 22), and residue 32 adjacent to the defined HBR region is also a lysine. In addition to hydrophobic and electrostatic interactions, MA also exhibits specificity for phosphoinositol-4,5-diphosphate (PI(4,5)P$_2$)) [18–20], a characteristic marker of the inner leaflet of the PM [102]. The interaction between MA and PI(4,5)P$_2$, which is found exclusively in the PM, prevents Gag from non-productive association with other cellular membranes. The fully assembled Gag lattice, which forms the protein backbone of the viral capsid, has been studied by electron tomography [103]. However, to dissect the molecular mechanisms that attract the protein to the lipid surface requires a comparative study of the smaller MA domain in a well-controlled environment.

Previously the structure of –myrMA on charged bilayers was measured using NR and revealed the orientation of membrane-bound MA when association is driven by purely electrostatics since neither the myristoyl moiety (hydrophobic) or PI(4,5)P$_2$ (specific) were present [21]. The observed orientation was favorable for Gag lattice formation, but it was unclear from this study if myristoylation would modulate the structural organization of MA on the membrane. In the work presented here NR was used to measure myrMA on charged stBLMs (that did not contain PI(4,5)P$_2$) to determine the effect of myristoylation on the orientation of MA. We first review the challenges associated with studying a protein with multiple membrane binding motifs and reduced solubility due to the myristoyl moiety and discuss the conditions needed to overcome these obstacles. Then we report the structural organization of myrMA on charged membranes and compare its orientation with that of –myrMA [21]. Our results support the conformational flexibility of myrMA and show the effect of pH on the dynamics of the myristoyl sequestration pocket. The combination of hydrophobic and electrostatic interactions leads to a protein orientation that is distinct from purely electrostatic association. The protein re-orientation positioned key residues favorably for engagement of PI(4,5)P$_2$ (even though it was not present).

In addition to the structural work, myrMA was used in the first application of the PE-based stBLMs for binding measurements. Recent free energy calculations of MA binding to membranes of varying composition revealed how individual bilayer components and protein myristoylation contribute to MA membrane association [22]. The study showed that efficient membrane-association is driven not only by lipids that directly engage the protein but by membrane properties as a whole, based on the effect of cholesterol on binding affinity. The lipid compositions used in were relatively complex (three to four components) [22], but they lacked PE–the main zwitterionic component of the inner leaflet of the PM [23]. In this work stBLMs with PE as the majority lipid species were developed (Chapter 3) to better mimic the inner leaflet of the PM. Inclusion of PE, while maintaining the same mol% of PS and cholesterol, increased the membrane binding affinity of myrMA by a factor of $\sim$2.

This work advances previous studies on the membrane-association of HIV-1 matrix presented in Nanda *et al.* (2010) [21] and Barros *et al.* (2016) [22]. Dr. Marilia Barros conducted the SPR measurements for –myr and myr MA binding to non-PE containing stBLMs [22] with the exception of the 50:20:30 PC:PS:chol measurement. In addition, Dr. Barros used NR to measure myrMA on stBLMs containing 30% PS at pH 7.4 and pH 8. However, due to the difficulties that will be presented in this work, a conclusive structural characterization of membrane-bound myrMA could not be determined from this data. For all myrMA work, Dr. Ioannis Karageorgos performed the protein purification. The hydrogen/deuterium exchange with mass spectrometry experiments were conducted by Drs. Karageorgos and Kerry M. Scott. My contribution to the MA project includes overcoming obstacles that previously prevented a structural characterization of myrMA, determining the membrane-bound structure of myrMA which revealed the effect of myristoylation of the orientation of
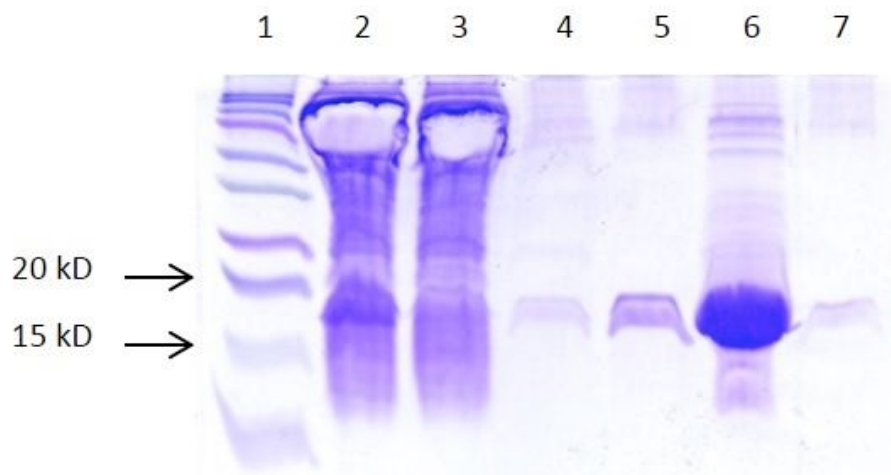
Figure 4.2: Coomassie-stained SDS-PAGE profile of purified myrMA. Lane 1: Protein standard. Lane 2: Soluble myrMA from *E. coli* cells. Lane 3: Proteins that did not bind the IMAC resin. Lane 4: Proteins washed from IMAC resin by lysis and 10 mM imidazole buffers. Lanes 5-7: Final elutions from IMAC resin using 300 mM imidazole buffer.

membrane-bound MA, the development of PE-based stBLMs and a PM mimic, and probing the effect of PE on the binding affinity of myrMA.

4.2   Materials and Methods

4.2.1   Protein Expression   2

Standard laboratory chemicals, culture media, myristic acid, isopropyl-b-D-thio-galacto pyranoside (IGTP), and phenylmethylsulphonylfluoride (PMSF) were purchased from Sigma Aldrich (St. Louis, MO), unless otherwise noted. Tris(2-carboxyethyl)phosphine hydrochloride (TCEP-HCl) was purchased from Thermo Fisher Scientific (Waltham, MA). The plasmid used for myrMA preparation via coexpression of MA protein and N-myristoyltransferase was kindly provided by Michael Summers (University of Maryland at Baltimore County). Transformed E.Coli BL21 (DE3) cells containing the expression vector were grown while shaking (250 rpm) at 37°C to $OD_{600} = 0.4$. Cells were supplemented with 1 mL of myristic acid (10 mg/mL) per liter of culture and kept growing to $OD_{600} = 0.8$. At this point protein expression was induced by adding IPTG to a concentration of 1mmol/L (1 mM), and the cells were kept at 30°C overnight.
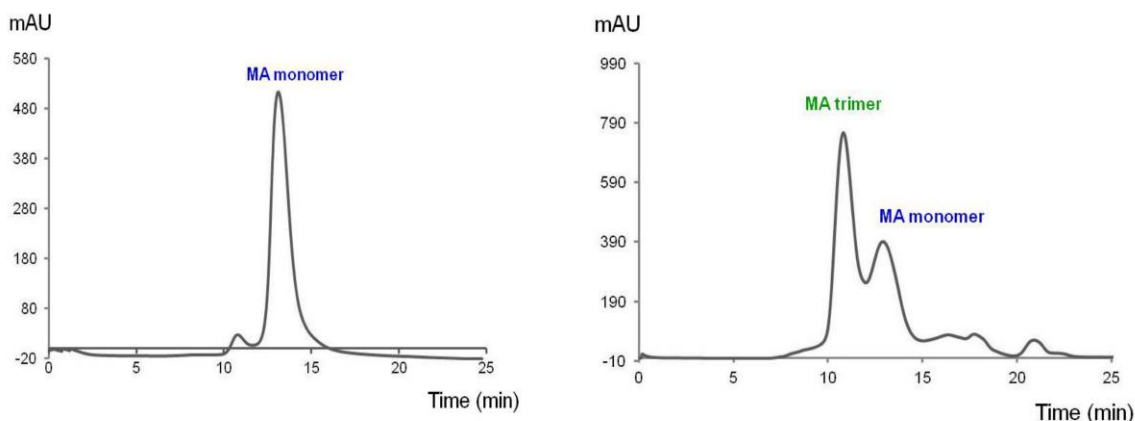
Figure 4.3: Size exclusion chromatography of myrMA on a 75 10/30 GL column. (Right) Chromatogram of protein purified via IMAC revealing both a monomer and trimer population. (Left) Chromatogram of the isolated monomer.

The cells were harvested by centrifugation at 6000 g for 15 min at 4°C, washed with PBS, and held frozen at -80°C. Five grams (wet-weight) of cells were re-suspended in 30 mL lysis buffer (20 mM Tris, 300 mM NaCl, 10% glycerol, 1 mM PMSF, 1X protease inhibitor mixture set I (Calbiochem; EMD Millipore, Billerica, MA), 1 mM TCEP, pH 7.4) and disrupted on ice by sonication. The cell lysate was centrifuged at 10000 g for 30 min at 4°C, and the protein was purified by immobilized metal affinity chromatography (IMAC). Monomeric MA was separated by size exclusion chromatography on a superdex-75 10/30 GL column using an AKTA purifier system (Amersham Biosciences, Little Chalfont, UK).

myrMA protein was overexpressed in a prokaryotic system, which offers greater ease and economy of protein generation than an eukaryotic system. A 6-His-tag was incorporated into the C-terminus of the protein to facilitate isolation using IMAC. BL21(DE3)/pLysS strain was selected for large scale expression of the myrMA. SDS-PAGE followed by Coomassie staining revealed that the IMAC [104] based purification affords mainly a single band under reducing conditions, suggesting purity (Figure 4.2). The proteins molecular mass, 15 kDa as estimated from comparison to protein standards, corresponds well to myrMA calculated molecular mass of 15.745 kDa. However, further size exclusion chromatography (SEC) measurements (Figure 4.3) demonstrate that myrMA forms a mixture of trimer and monomer at ∼50 kDa and 15 kDa, respectively. The monomer population was isolated and remained stable.

4.2.2 Mass Spectrometry

Mass spectrometry (MS) was used for protein identification and to establish purity via an electrospray ionization (ESI) interface on an Agilent 6550 quadrupole time
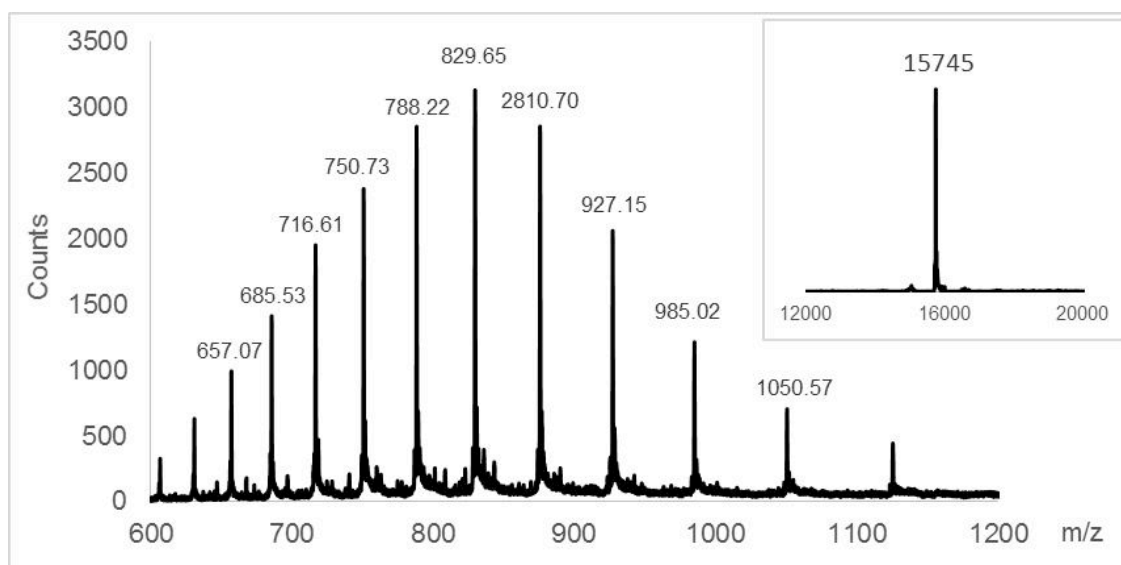
Figure 4.4: ESI mass spectrum of myrMA. LC-ESI-Q-TOF analysis of myrMA produced a 15,745 (±1) m/z ion peak, which is assigned to the [M+H]+ peak. Homogenity of the isolated monomer as evidenced by an absence of other ion peaks in the mass spectrum.

of flight (QTOF) mass spectrometer coupled with an Agilent 1200 high performance liquid chromatography column (Santa Clara, CA). Protein was eluted from a C18 column (3 μm, 3 mm x 150 mm; Waters, Milford, MA) over a 30 minute gradient from 3% to 60% acetonitrile containing 0.1% formic acid at a flow rate of 9 μL/min. Data was acquired in positive ion mode with the following settings: capillary temperature, 290°C; capillary voltage, 3500 V; fragmentor, 300 V; and a m/z 300-3200 mass range. Mass deconvolution was performed using the Agilent MassHunter (version B.06) software. Peptic peptides of myrMA (Figure 4.5) were generated by passing 17 pmol of protein through an Enzymate pepsin column (Waters, Milford, MA) and identified using tandem MS (MS/MS) on a Thermo LTQ Orbitrap Elite unit (Thermo Fisher Scientific, Waltham, MA). One full mass spectral acquisition triggered six scans of MS/MS with activation by collision-induced dissociation (CID) on the most abundant precursor ions. Peptides were identified by the MASCOT (Matrix Science, Oxford, UK) database search engine with the following parameters: enzyme, none; oxidation (M) as a variable modification; MS tolerance, 20 ppm; MS/MS tolerance, 0.6 Da; peptide charge of +2, +3, and +4. Homogeneity of the isolated monomer by SEC is evidenced by an absence of any other ion peaks in the ESI mass spectrum (Figure 4.4). LC-ESI-QTOF analysis of myrMA showed a 15,745 (±1) m/z ion peak, which is assigned to the [M+H]+ peak.
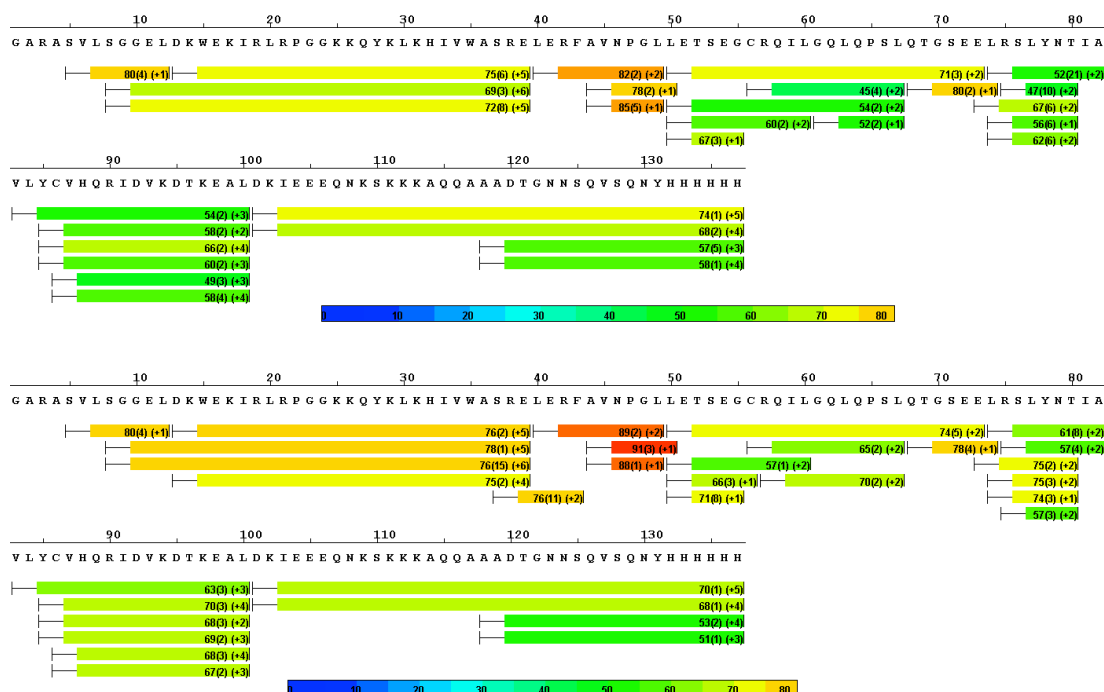
Figure 4.5: Sequence coverage map for peptic peptides of myrMA. (Top) Peptides of myrMA in pH 7.4 and (Bottom) pH 8.0 that were identified by MS/MS. The HDX-MS kinetic results are plotted for each peptide with colors ranging from blue to red for low to high deuterium uptake, respectively.

4.2.3 HDX-MS and HDX Data Processing

D_2O was obtained from Cambridge Isotope Laboratories Inc. (Andover, MA). For the hydrogen/deuterium exchange with mass spectrometry (HDX-MS) analyses, the myrMA protein stock was diluted in H_2O buffer (20 mmol/L Tris, 150 mmol/L sodium chloride, 2 mmol/L TCEP at pH 7.4 and 8.0) to prepare a 5 μmol/L final concentration and equilibrated at 1° C. HDX was conducted on a HDX PAL robot (LEAP Technologies, Carrboro, NC). Protein solutions (5 μL) were diluted into 25 μL D_2O buffer (20 mmol/L Tris, 150 mmol/L sodium chloride, 2 mmol/L TCEP at pH 7.4 and 8.0) at 25° C. At selected times (0 s, 30 s, 5 min, 15 min, 1 h, and 4 h) the HDX sample was quenched by mixing with 35 μL quench buffer (3 mol/L urea, 0.1 mol/L sodium phosphate at pH 2.5) at 1° C. The quenched solution was injected into an on-line immobilized pepsin column for 3 min. The digested protein solution was trapped on a C18 guard column (1.0 mm diameter x 10 cm length, 5 μm; Grace Discovery Sciences, Deerfield, IL) and separated with a C18 analytical column (1.0 mm diameter x 5 cm length, 1.9 μm, Hypersil GOLD; Thermo Fisher Scientific, Waltham, MA)

47
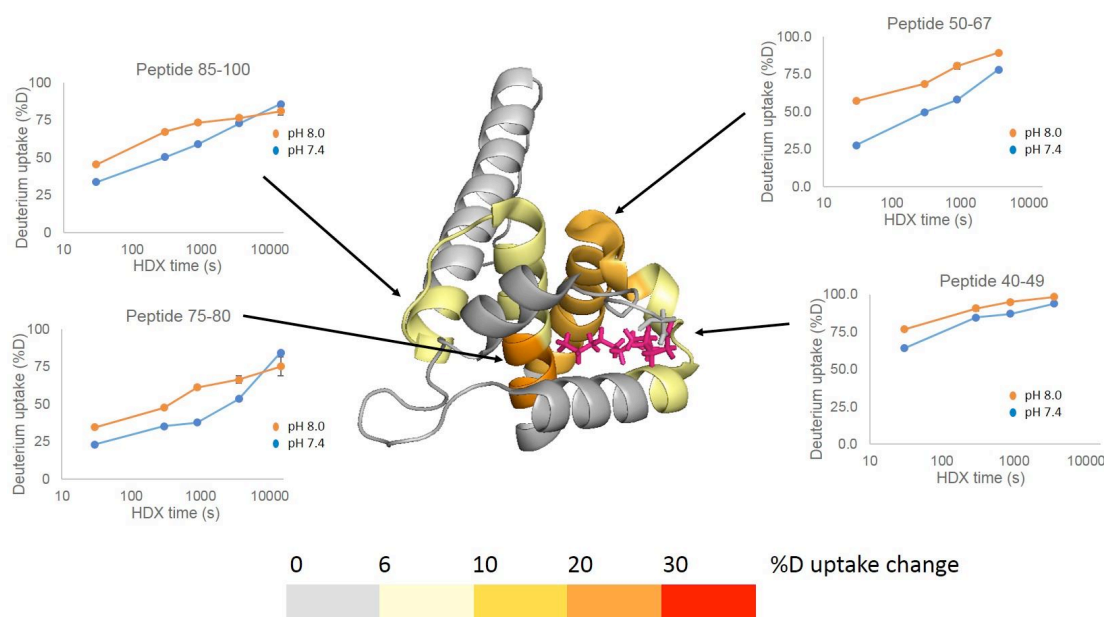
Figure 4.6: Plot of deuterium uptake vs. time for 5 peptides of myrMA. The differential deuterium profiles for protein at pH 7.4 and pH 8.0 at 30 min are mapped onto the crystal structure of myrMA. Increased differential uptakes were color-coded from light yellow to red. Gray denotes regions were peptic peptides present no difference in deuterium uptake.

via a Dionex Ultimate 3000 UPLC with a 9.5 min gradient operated with a binary mixture of solvents, A (water containing 0.1% formic acid) and B (80% acetonitrile and 20% water containing 0.1% formic acid), at 50 μL/min flow rate. The gradient settings were: 5% to 35% solvent B for 3 min, 35% to 60% solvent B for 5 min, 60% to 100% solvent B for 0.5 min, isocratic flow at 100% solvent B for 0.5 min, and a return in 5% solvent B for 0.5 min. LC connection lines and valves were housed in a refrigerated compartment at 2°C. Peptides were analyzed on a Thermo Orbitrap Elite unit (Thermo Fisher Scientific, Waltham, MA). The instrument settings were: spray voltage, 3.7 kV; sheath gas flow rate, 25 (arbitrary units); capillary temperature, 275° C; resolution set at 60000. Three replicates for each ion-exchange time point were obtained.

From mass spectra obtained in the HDX-MS experiments, the centroid of each deuterated peptide envelope and the relative deuterium uptake by each peptide were calculated using HDX WorkBench (Scripps Research Institute, Jupiter, FL; Figure 4.6). Corrections for back exchange were made by considering the values of 80% deuterium content of the exchange buffer and an estimated 70% deuterium recovery. Paired t-tests were used to verify deuterium uptake differences.

4.2.4   Liposome and stBLM Preparation

The vesicles and stBLMs were prepared using a 1 M NaCl, 10 mM NaPO4 at pH 7.4 high salt aqueous buffer for vesicle formation and a 50 mM NaCl, 10 mM NaPO$_4$, pH 7.4 low salt buffer to complete stBLM formation for membrane compositions that did not contain PE. For PE-containing stBLMs, a 2 M NaCl, 10 mM NaPO4 at pH 7.4 high salt aqueous buffer was used for vesicle formation. The same low salt buffer (50 mM NaCl) was used to complete bilayer formation.

4.2.5   NR and SPR

A low ionic strength buffer composed of 50 mM NaCl, 10 mM NaPO$_4$ was used for all measurements. Initially a pH of 7.4 was used for both SPR and NR studies, however NR revealed overlayers of protein at the interface for this condition. For the NR experiments we increased the pH to 8.0 to shift the MA monomer/trimer equilibrium entirely to monomer in order to obtain a monolayer of bound protein.

4.3   Results and Discussion

4.3.1   myrMA Membrane Binding Depends on pH

Biophysical studies of protein binding to membranes are ideally conducted under physiological conditions to allow for an extrapolation of the experimental results to the *in vivo* situation. In practice, however, this is often impossible. As a truncation product of full-length Gag the isolated MA domain lacks the self-interaction mechanisms that promote Gag multimerization at the membrane via CA dimerization and RNA binding by the NC [105]. Therefore a reduction in the ionic strength of the buffer used for measurements was necessary to shift the binding equilibrium of MA for characterization of the membrane bound state [21, 22]. Other techniques, such as NMR, required a low pH to permit measurements of protein-lipid interactions [20]. Based on a comprehensive set of data for myrMA binding to lipid membranes [22], optimal buffer conditions for a structural characterization using NR were found to be pH 7.4 and 50 mM NaCl where the K_d (binding affinity) is ~ 5 μM. While SPR measurements indicated Langmuir binding behavior, NR revealed membrane remodeling and proteinaceous multilayers at the membrane interface under these conditions (Figure 4.7), which prohibited a conclusive structural characterization of membrane-bound myrMA in contrast to –myrMA that formed well-defined protein monolayers at the membrane [21].

NMR studies of myrMA showed the myristate group can adopt sequestered and exposed states with only minor conformational changes to the N-terminal region and helix I [18, 101]. MA oligomerization has been associated with myristate exposure and also depends on protein concentration and pH [101, 106]. At pH 7.0 the
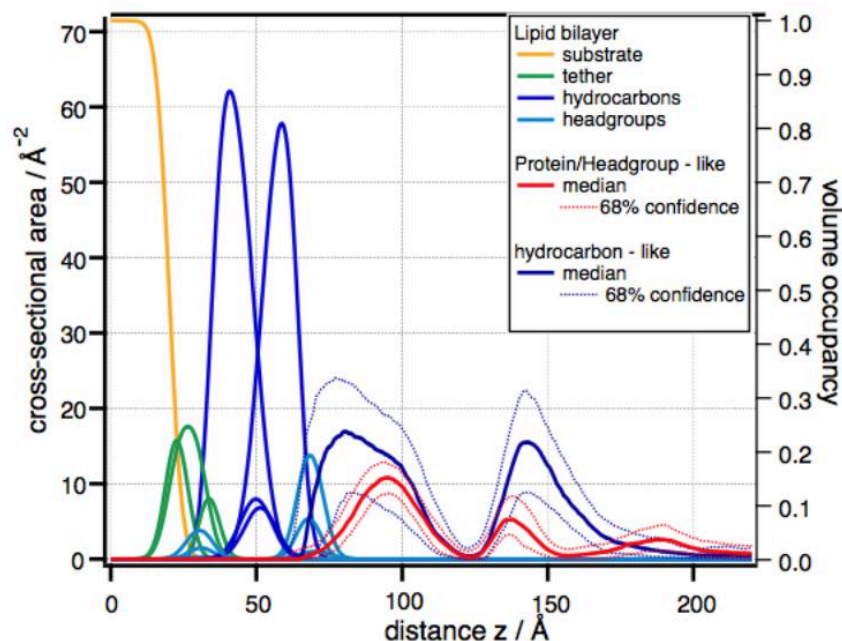
Figure 4.7: NR profile of myrMA on a 70:30 DOPC/DOPS stBLM at pH 7.4. While SPR measurements identified 50 mM NaCl at pH 7.4 as optimal buffer conditions, NR revealed the presence of protein overlayers and membrane remodeling under these conditions. The median envelopes with 68% confidence intervals are shown for protein (red) and hydrocarbon-like material (blue). The data and figure were produced by Dr. Barros and more information can be found in her thesis, *Revealing the structural and molecular basis of retroviral assembly and endolysin PlyC membrane translocation using surface plasmon resonance and neutron reflectometry.*

monomer/trimer dissociation constant is $(1.4 \pm 0.2) \times 10^{-8}$ M^2, whereas at pH 8.0 myrMA was purely monomeric within detection limits [106]. For a protein concentration of 10 μM, used for the NR measurements, the trimer concentration is < 50 nM, which should be insignificant for membrane binding based on the binding affinity determined for the monomer using SPR. However, if the membrane binding motifs from all three monomer subunits in the trimer engage the membrane, then the trimer would bind the membrane with a signficantly higher affinity (sub-micromolar).

We increased the buffer pH from 7.4 to 8.0 to shift the monomer/trimer equilibrium entirely towards monomer. SPR experiments on a 70:30 POPC/POPS stBLM showed a reduction in the binding affinity by a factor of $\sim$4 (Figure 4.8), consistent with a shift towards the myristoyl sequestered state [20, 106] and a change in protein charge from $+3.7e$ to $+2.9e$ [107]. The saturation surface coverage was not significantly affected by the pH change, and the binding curve is well described by the Langmuir model.
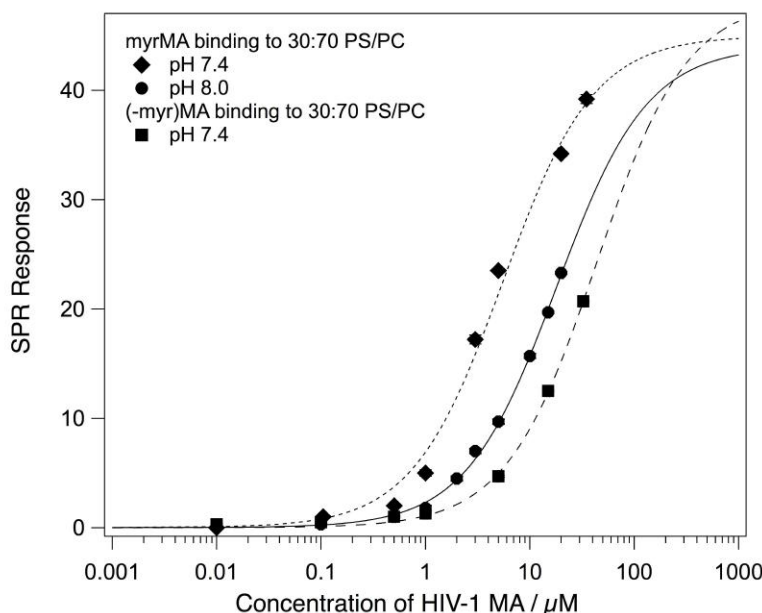
Figure 4.8: MA binding to stBLMs containing 30% PS at 50 mM NaCl.
The equilibrium response is plotted as a function of MA monomer concentration and
fit to the Langmuir isotherm, and the binding curve for –myrMA at pH 7.4 is included
for comparison. The K_d of myrMA increases from ∼5 to ∼ $18\mu M$ between pH 7.4
and 8.0 but remains significantly lower than for –myrMA at either pH. This shows
that the myristate still contributes to membrane binding at pH 8.0.

4.3.2 pH Dependence of myrMA Conformational Flexibility

HDX-MS was used to probe the effect of pH on the conformational flexibility of
myrMA in solution and to correlate dynamic changes with myristic acid exposure.
Such experiments detect the exchange of backbone amide hydrogen atoms of indi-
vidual amino acids and reveal the extent of amide hydrogen bonding and solvent
accessibility of a protein. By comparing measurements for different conditions, such
as varying pH, changes in protein conformation and/or dynamics can be determined.
The data revealed that 34% of the reporting amides were affected by pH changes
from 7.4 to 8.0 and exhibited higher deuterium uptake rates over time (between 6
and 30%). The remaining 66% of the protein was not affected by pH changes. The
overall deuterium uptake rate increase suggests that myrMA becomes more dynamic
in a number of distinct regions at pH 8.0, and the majority of these regions belong to
the helices that form the myristate pocket (Figure 4.9). From this evidence it appears
that the higher pH increases the flexibility of the pocket.

Based on NMR, helix I is tightly packed against helices II and V in the myristoyl
exposed state, and this conformation is stabilized by a salt bridge between Glu12 and
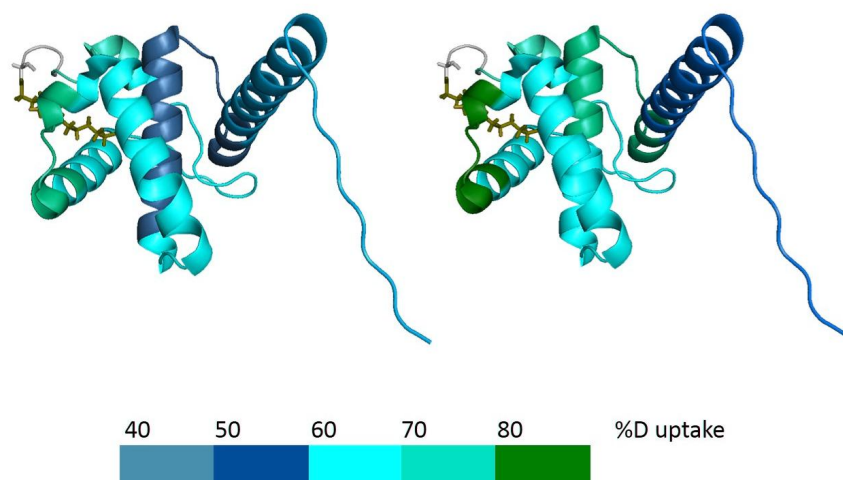
Figure 4.9: Deuteration profile of myrMA. The deuteration profile of myrMA was collected after 30 min of incubation in D_2O at pH 7.4 (left) and pH 8.0 (right). The higher pH appears to increase the flexibility of the myristate pocket.

His89 and a hydrogen bond between Glu12 and Ser9. However, these contacts are lost upon myristoyl sequestration as helix I shifts to accommodate the myristate [106]. The loss of the stabilizing salt bridge and hydrogen bond is consistent with the increased flexibility observed by HDX-MS. This in turn promotes myristate sequestration at pH 8.0 in accordance with the SPR binding data and literature [101, 106].

4.3.3 myrMA Membrane Association Under Optimized Conditions

To probe if the optimized conditions prevented the formation of overlayers 10 μM myrMA was studied with NR at 70:30 d_{31}-POPC/POPS stBLM at pH 8 and 50 mM NaCl. The free-form protein CVO profile was consistent with a single layer of protein at the membrane interface (Figure 4.10), but a detailed analysis revealed that this profile is inconsistent with a single protein conformation at the membrane, as it exhibits a broad maximum that exceeds the dimensions of a single MA molecule by $\approx$ 50%. Rinsing the sample with buffer did not result in significant changes, indicating stable and irreversible protein binding. The result agrees with coarse-grained MD simulations of myrMA [108] and electrostatic modeling [109] that suggest dynamic binding of myrMA to the membrane in multiple conformations. We concluded that a slight tendency for protein multimerization at the interface remains a possibility. In addition, the low volume occupancy of the protein (5-10%) left the analysis vulnerable to systematic errors, which may be as large as 3% in the CVO profile.
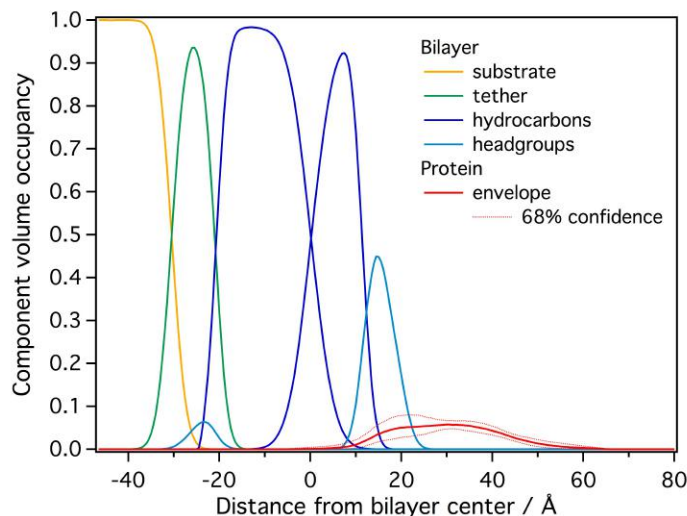
Figure 4.10: NR profile of myrMA on a 70:30 d$_{31}$-POPC/POPS stBLM at pH 8.0. The stBLM was incubated with 10 μM protein. The median protein envelope, shown with 68% confidence intervals (red traces), is inconsistent with a single MA conformation at the membrane interface.

In a subsequent NR experiment we increased the fraction of PS to 50% to obtain a higher protein surface coverage and provide a more homogeneous binding interface, thereby potentially reducing the propensity of the protein to adopt multiple conformations at the membrane. These conditions yielded a CVO profile compatible with a single MA conformation at the membrane (Figure 4.11). The orientation of myrMA at the interface was determined using the ensemble average of the NMR structures in PDB 2H3F [18]. A comparison of the free-form CVO spline profile with the result of the rigid body modeling shows very good agreement for the folded core. This indicates the protein does not undergo major conformational changes upon membrane association. However, there is imperfect agreement for the flexible termini, which suggests the ensemble of solution structures from PDB 2H3F does not describe the conformations of the N and C-terminal regions measured by NR. The observed extra density of the protein spline CVO at the bilayer interface is consistent with membrane insertion of the myristate and N-terminal residues. Insertion of the N-terminal region of myrMA is supported by recent NR measurements of a peptide that represents myrMA truncated to residues 2-32 which revealed insertion of this peptide into the bilayer [110]. The observed discrepancy between the free-form spline CVO profile and the profile based on PDB 2H3F in the flexible C-terminal region shows the ensemble of solution structures is too compact. While the orientation of myrMA at the membrane is largely constrained by the asymmetric and compact globular core, some uncertainty in the final result remains due to the discrepancies in the termini.
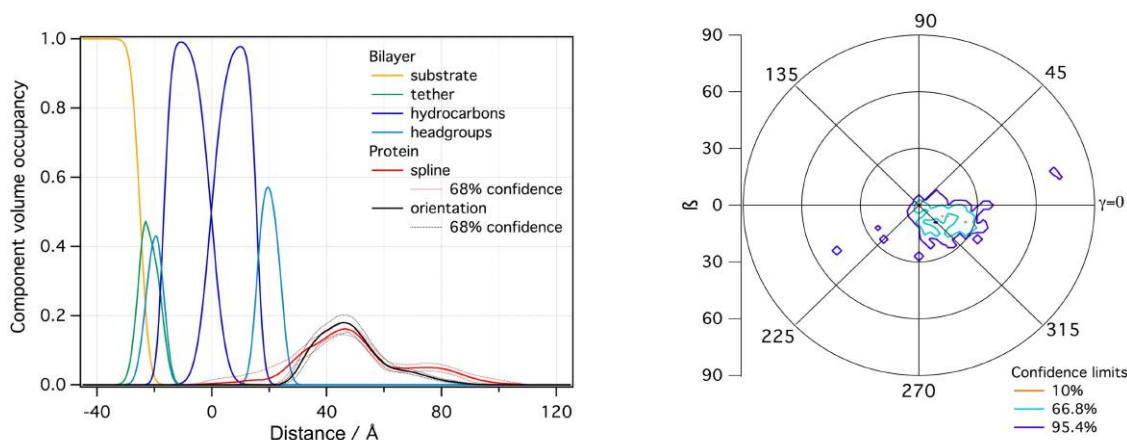
Figure 4.11: NR results from myrMA on a 50:50 DOPC/DOPS stBLM at pH 8.0. (Left) NR CVO profile after incubation with 10 μM protein. The median protein envelope is shown with 68% confidence intervals (red traces). The median orientation fit using the MA NMR structure (PDB 2H3F) is shown for comparison (black trace). (Right) The probability distribution of myrMA orientations with respect to the 50:50 DOPC/DOPS bilayer normal.

For the most likely orientation of myrMA at the membrane ($\beta \approx 20°$, $\gamma \approx 335°$, Figure 4.11), helix I and residues 31-35 of helix II are in close contact with the lipid membrane surface. While the overall membrane penetration is shallow, residues in the HBR penetrate more deeply into the bilayer. In particular lysine residues K26, K27, K30, and K32 penetrate deeply into the headgroup layer. Based on simulations [108] and previous NR measurements of –myrMA [21], these residues mediated membrane interactions via electrostatics when PIP_2 was not present in the membrane model. When PIP_2 was included in the membrane model, these residues were still involved in membrane interactions, and K30 and K32, specifically, were shown to be important for PIP_2 binding [20]. Mutation of these residues to glutamate retargeted Gag to intracellular compartments instead of the PM [17]. In addition, R4 was also identified as interacting with the membrane [20, 21], but rigid body modeling of the NR data does not place this residue in direct contact with the headgroup region. However, with the proposed flexibility of the N-terminus, R4 may penetrate the lipid headgroups as well.

Other HBR residues also interact closely with the membrane in our NR model: K15 and K18 from helix I and R20 and R22 from the loop connecting helix I and II. Based on rigid body modeling, K18 and R20 penetrate slightly into the headgroup layer, and K15 and R22 may also insert into the headgroup region depending on side-chain conformations. The earlier NR characterization of –myrMA also identified these residues as interacting with the membrane, albeit more peripherally [21]. Notably,
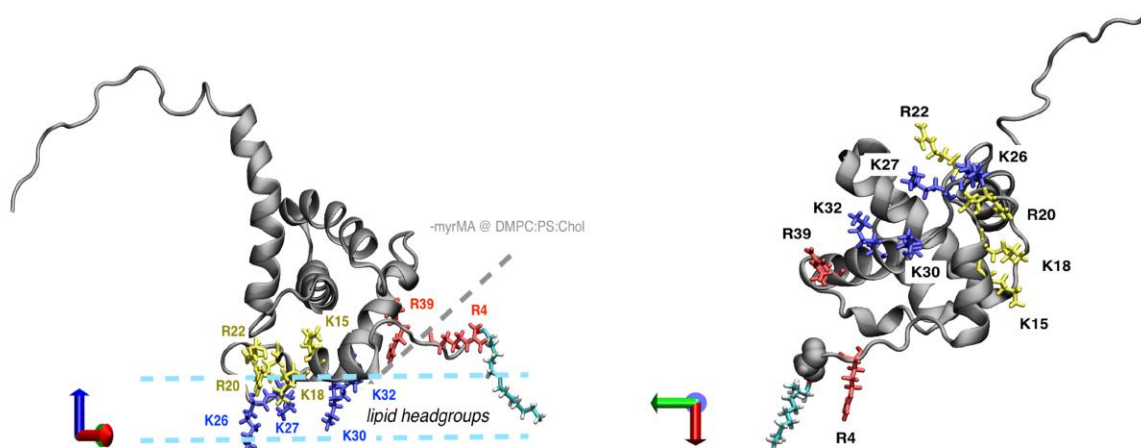
Figure 4.12: Mostly likely orientation of myrMA on a 50% PS stBLM.
(Left) Lysine residues (K26, K27, K30, K32) that penetrate deeply into the lipid
headgroup region are highlighted in blue. Basic residues with peripheral interaction
(K15, R22) or slight penetration (K18, R20) are shown in yellow. Arginine residues
(R4, R39) that were previously shown with –myrMA to interact closely with the
membrane but are more peripheral for myrMA are shown in red. A myristate group,
shown in cyan, was added to the protein structure to highlight its location (Right)
Bottom view of myrMA in its membrane bound orientation.

R39, which showed significant overlap with the headgroup region for –myrMA, is fur-
ther away from the membrane surface for myrMA. The change in orientation between
the –myrMA and myrMA structures brings helix I and the HBR into more direct con-
tact with the membrane surface while positioning R39 on helix II further away (Figure
4.12). In MD simulations a similar change in orientation was observed between the
myristate exposed and myristate sequestered states, and myristate-membrane inter-
actions resulted in a similar shift in membrane contacts from helix II to helix I [108].
The re-orientation of MA due to the myristate positions the HBR favorably for en-
gagement of PIP$_2$.

4.3.4   Binding of myrMA to a PE-based stBLM

Recently the individual interactions (electrostatic, hydrophobic, and PI(4,5)P$_2$ spe-
cific) driving MA binding to stBLMs containing mixtures of PC, PS, cholesterol, and
PI(4,5)P$_2$ were quantified [22]. Cholesterol was found to have a significant impact on
MA binding even though there is no known mechanism that promotes direct interac-
tion between Gag and cholesterol. Instead, cholesterol appeared to increase protein
affinity by promoting PI(4,5)P$_2$ binding and efficient insertion of the myristate [22].
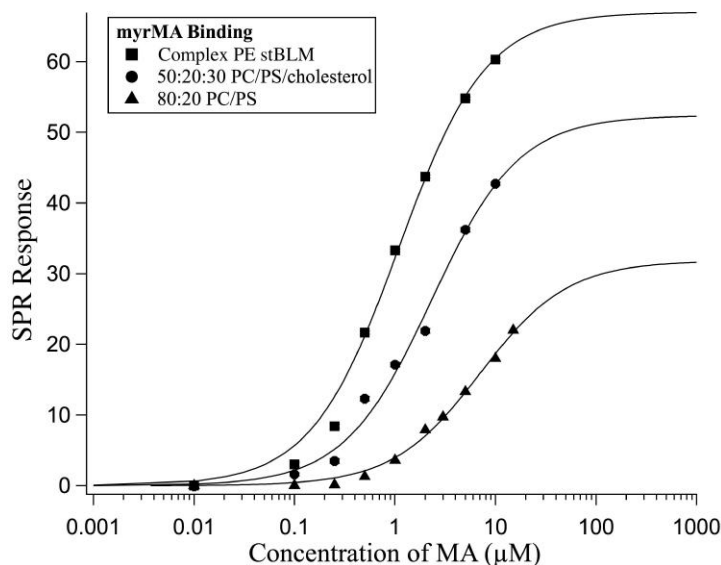
Figure 4.13: MA binding to stBLMs that contain 20% PS of increasing complexity. As measured previously [22], cholesterol enhances binding to PS-containing stBLMs and also increases the surface coverage. In the PE complex membrane the amount of PS and cholesterol is also 20 mol% and 30 mol%, respectively, thus it is the inclusion of PE that further enhances both the binding affinity and surface coverage.

This is a prime example that membrane-association is not only driven by lipids that directly engage the protein but by the membrane properties as a whole. Since the inner leaflet of the PM contains a significant amount of PE [23], inclusion of this lipid may also impact MA binding even if MA does not directly interact with PE.

NMR studies of MA in solution with truncated, soluble PC, PS, and PE showed direct interactions between these lipids and MA with the protein exhibiting a similar binding affinity for each lipid [135]. From this study a trio-engagement model was proposed in which MA is anchored to the PM via PI(4,5)P$_2$, the myristoyl moiety, and either PS, PC, or PE. However, more recent NMR studies found PE had no significant effects on liposome binding when present at physiological concentrations or in combination with other lipids [20]. Instead, binding was enhanced to liposomes containing both PS and cholesterol, in agreement with the stBLM data in which cholesterol enhances MA binding to PS-containing bilayers [22]. To probe if inclusion of PE in stBLMs could promote more efficient MA binding, we measured the binding of myrMA to the complex PE membrane (30 mol% POPE, 19.5 mol% POPC, 0.5 mol% DMPC, 20 mol% POPS, and 30 mol% cholesterol) without PI and PI(4,5)P$_2$.

Inclusion of PE increased the binding affinity by a factor of ∼2 and also increased the surface coverage of myrMA (Figure 4.13 and Table 4.1). This result differs from

liposome measurements where inclusion of PE did not effect binding [20]. However, it is not definitive from the current SPR measurements if the increase in affinity is due to a direct interaction between myrMA and PE, as suggested by the trio engagement model [135]. Previous SPR measurements provide evidence against this model as no interaction was observed between myrMA and PC [22]. PE may increase the binding affinity and surface coverage in a similar-manner as cholesterol [22] by facilitating the insertion of the myristate through an overall change to the physical properties of the membrane due to its small headgroup size. To probe for a direct interaction, the binding affinity of myrMA for PC:PE stBLMs should be measured.

Table 4.1: Binding Affinity of myrMA to stBLMs with Progressively More Complex Lipid Compositions

	myrMA	
Membrane composition	K_d (μM)	R_∞ (pixels)
100 % DOPC*	no binding detected	
DOPC:DOPS=80:20*	7 ± 0.9	33 ± 1
DOPC:DOPS=70:30*	5 ± 0.4	45 ± 0.5
DOPC:DOPS:cholesterol=50:20:30	2.3	53
DOPC:DOPS:cholesterol=40:30:30*	2.1 ± 0.1	84 ± 0.6
POPE:POPC:DMPC:POPS:chol=30:19.5:0.5:20:30	1.04 ± 0.1	64 ± 4

Measurements denoted with * were collected by Dr. Marilia Barros and are published in [22]

4.4   Conclusions

The current structural study of myrMA is an important step towards a full structural characterization of HIV-1 Gag membrane binding and viral assembly. We identified experimental conditions (50 mM NaCl pH 8.0, highly charged stBLM) that overcame the challenges presented by the conformationally dynamic peripheral membrane protein myrMA. Our results for membrane-bound myrMA showed minor deviations of the membrane-bound protein structure from the high-resolution NMR structural ensemble in solution. These deviations were localized to the flexible termini regions with agreement between the structures for the well-folded core. By comparing the membrane-bound structure of myrMA with the previously determined structure of –myrMA [21], we observed that their membrane complexes are similar. However, the presence of the myristate resulted in a re-orientation of MA that shifted the membrane contacts from helix II to helix I. This myristate driven re-orientation of the protein positions the HBR favorably for engagement of PIP$_2$ by bringing it into direct contact with the membrane.

To better mimic the inner leaflet of the plasma membrane stBLMs were developed with PE as the majority lipid species and relevant amounts of PS and cholesterol (Chapter 3). Inclusion of PE resulted in a modest increase in the membrane binding affinity of myrMA compared to PC:PS:chol stBLMs with the same mol% of PS and cholesterol. Similar to cholesterol [22], PE may increase the binding affinity and membrane surface coverage of myrMA by facilitating the insertion of the myristate due to an overall change in the physical properties of the membrane instead of by direct interaction with the protein. While a stBLM mimic for the inner leaflet of the PM, which includes the relevant phosphoinositides PI and PIP_2, has been developed, SPR measurements still need to be conducted. We hypothesize that the PM mimic will result in a further increase of the binding affinity to the sub-micromolar range due to the inclusion of PIP_2, which was previously shown to increase the binding affinity in two and three-component stBLMs [22].

For the MA project, inclusion of PIP_2 is important for the next steps. In the cell MA engages with the inner leaflet of the PM via hydrophobic, electrostatic, and PIP_2 interactions, thus it is important to capture these interactions in the model system to mimic the cellular environment and extrapolate the experimental results to the *in vivo* situation. In terms of structure, PIP_2 should be added to the PC:PS membrane to determine if further structural re-arrangements are induced, even though myrMA appears to be oriented favorably with key residues already positioned for interactions with PIP_2 on the PC:PS stBLM measured here. For the binding studies, the next measurements should be conducted using myrMA and the PM mimic since inclusion of PE-alone was already shown to increase the binding affinity, and the effect of PIP_2 on myrMA binding for PC-based stBLMs (ranging from two to four components) has already been determined.

Chapter 5

Characterization of HIV-1 Nef at a Lipid Membrane Interface

Nef is an accessory protein—meaning it has no intrinsic catalytic activity, no direct role in viral reproduction, and is not a structural factor for viral assembly. However, its function is essential for HIV-1 infectivity, immune evasion, and the progression to AIDS, for which membrane association is crucial. Here we used SPR to determine the binding affinity of several Nef constructs, including myristoylated and non-myristoylated wildtype Nef and a dimerization-defective mutant, to charged stBLMs. NR was then used to determine the membrane-bound conformations of myrNef and a dimerization-defective mutant.

5.1 Introduction

Nef is a viral accessary protein unique to primate lentiviruses HIV and SIV [137]. The name "negative factor" is a result of initial studies with the Nef protein which suggested that it suppressed viral replication and transcriptional activity of the HIV-1 long terminal repeat (LTR) responsible for gene expression [138–141]. However, it is a misnomer as Nef has been shown to be essential for high-titer viral replication and AIDS progression [25, 26, 29, 136, 142–145]. A critical role has also been established for Nef in HIV disease in both animal models and AIDS patients. Nef alone is able to induce a severe AIDS-like syndrome in transgenic mice [146]. In Rhesus monkeys infected with SIV in which the *nef* gene has been deleted viral loads remain low and infection rarely leads to AIDS [25], and in human patients with long-term, non-progressive HIV infection *nef* defective viruses have been isolated [147, 148].

Nef lacks enzymatic activity and instead functions via interactions with host cell proteins, including proteins involved in trafficking and signaling [26]. It is through these interactions that Nef plays its role in disease, including: prevention of super-infection and immune evasion through down-regulation of cell surface viral (CD4) and immune (MHC-1) receptors [149–151], enhanced viral replication and infectiv-
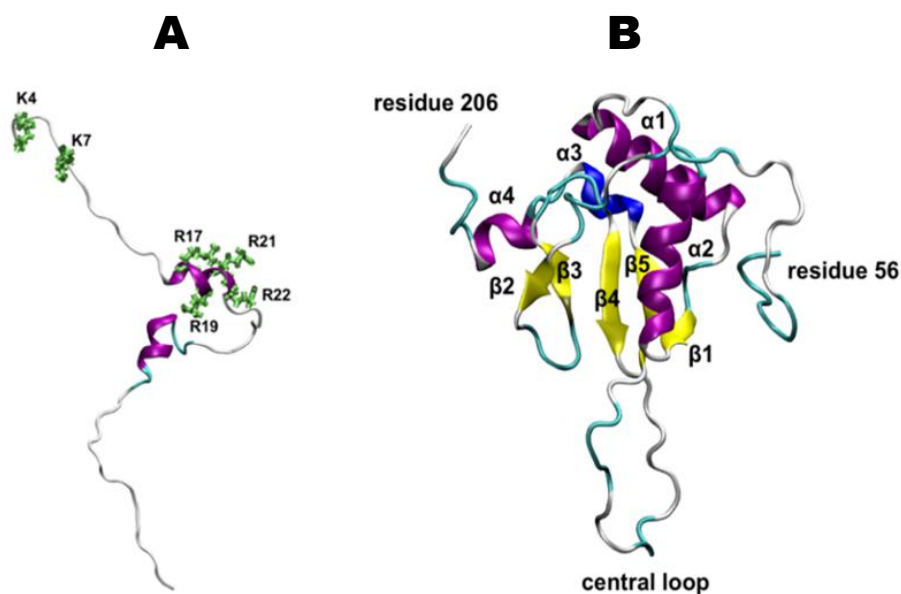
Figure 5.1: NMR Structures of the N-terminal Arm and Core of Nef. (A) Structure of the myristoylated N-terminal arm (PDB 1QA5 [35]) with basic residues (K4, K7, R17, R19, R21, R22) implicated in membrane interactions highlighted in green. (B) Refined solution structure of the Nef core (PDB 2NEF [36]) with central loop residues 159-173 missing. The core structure consists of a type II polyproline helix (residues 69-79), three α-helices (α1, residues 81-94; α2, residues 105-114; α4, residues 194-198), a 3/10 helix (α3, residues 187-190), and a five-stranded anti-parallel β-sheet (β1, residues 100-102; β2, residues 126-128; β3, residues 133-137; β4, residues 143-147; β5, residues 181-186). The structure is colored based on secondary structure with α helices in purple, β sheets in yellow, 3/10 helices in blue, turns in cyan, and coils in white.

ity through constitutive activation of non-receptor tyrosine kinases [41, 152], and increased infectivity by suppressing the incorporation of mammalian SERINC proteins into the viral membrane [153]. Shortly after viral infection Nef is expressed in high concentration [154] and leads to high viral loads in vivo [25]. Nef has been found in both cytosolic and membrane-associated fractions, suggesting that the protein may travel back and forth between the cytosol and membrane [155].

The structure of Nef can be separated into two domains: a genetically diverse and structurally flexible N-terminal arm (residues 2-54) and a well-conserved folded core domain (residues 55-206) that contains a central flexible loop (residues 149-179) [34]. The disorder in the N-terminal arm and the central loop present challenges for determining the structure of full-length Nef using traditional structure determination methods, although structures have been solved for the N-terminal and core

regions separately. The structure of the N-terminal region (residues 2-57) for non-myrisotylated and myristoylated protein was determined using NMR [35], while the structure of the folded core domain has been determined using crystallography and NMR in both its free-form [36, 161, 163] and bound to protein partners, primarily SH3 domains [160, 161]. The refined structure for the core in its free form [36] contains residues 56 to 158 and 174-206 with residues 159-173 of the central flexible loop missing. The central loop appears to adopt a well-ordered structure, however, when it directly interacts with protein binding partners such as AP-2 (clathrin-associated adapter protein 2) [156].

The Nef core is primarily responsible for interactions with protein binding partners [136] and does not contribute to membrane targeting based on live cell imaging results [164]. Membrane association is driven by myristoylation and lysine (K4, K7) and arginine (R17, R19, R21, R22) residues on the N-terminal arm [157,164]. *In vivo*, myristoylation is essential for Nef function [30,31], and its deletion resulted in significantly reduced infectivity, decreased CD4 [30] and MHC-1 down-regulation [158], and prevented the formation of an AIDS-like disease in mice transfected with Nef [159]. Based on the importance of myristoylation, membrane-association is implicated in Nef function.

Nef dimerization may also be essential for Nef function *in vivo*. Dimerization was first observed in bacteria and eukaryotic cells in 1993 [168], and dimers, trimers, and higher order oligomers were seen on CD4$^+$ HeLa cells [169]. There is extensive evidence that Nef forms dimers, and Nef dimerization has been implicated in Nef function [37,38,166,167,170]. Both crystal [160,161] and NMR structures [36] suggest multiple contact points between Nef monomers primarily within the α2 helix of the Nef core. This region contains a hydrophobic interface (Ile109 to Phe121) flanked by charged residues Arg105 and Asp123 [37]. The residues in the dimerization interface are highly conserved between HIV-1 Nef isolates, which suggests that dimerization has biological significance and is not just the result of crystal packing. In addition, mutation of Asp123, which inhibited dimer formation, also resulted in a loss of enhanced viral infectivity and cell surface receptor (CD4 and MHC-1) downregulation [38]. The Nef dimerization interface is distinct from the PxxPxR motif needed for interactions with several binding partners, in particular SH3 domains [36,37,161]. Futhermore loss of Nef function when dimerization is impaired is not due to an inability of Nef to bind its partners [37,167]. Both cell-based [37] and solution-based [162] assays suggest Nef dimers can form in the cytosol or solution, respectively, for non-myristoylated Nef. For myristoylated Nef, however, dimers were found only at the membrane in the cell-based assay [37] and in solution myrNef was entirely monomeric [162]. These results suggest the dimerization interface is not exposed in solution for myrNef, and instead membrane-association triggers exposure of the dimer interface (Figure 5.2).

Previous NR and x-ray reflectivity measurements of full-length Nef in a lipid monolayer environment [32] were consistent with the hypothesis that the N-terminal arm separates from the core following the membrane association of myrNef. Upon
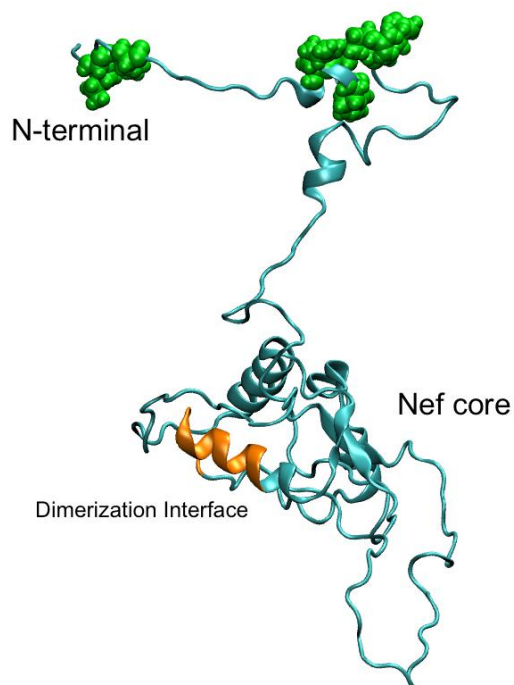
Figure 5.2: Modeled Structure of Full-Length myrNef in an Open Conformation. Based on previous NR results [32], lipid interactions results in a transition from a closed form to an open form of myrNef. In the open form the dimerization interface, residues 109-121 (highlighted in orange), is exposed. Basic residues (k4, K7, R17, R19, R21, and R22) implicated in membrane interactions are shown as green spheres. This model was adapted from [26] and produced by combining structures of the core (PDB 2NEF [36]) and N-terminal arm (PDB 1QA5 [35]) then the structure was relaxed using MD [32] (provided by Dr. Thomas E. Smithgall at the University of Pittsburgh).

insertion of the myristate group, Nef was found to undergo a conformational change from a "closed form" where the core is in contact with the monolayer to an "open form" where the core is displaced approximately 70 Å away from the lipid headgroups with some variability in the distance between the core and membrane [32]. While reflectivity methods cannot detect structural changes in the plane of the membrane, such as dimerization, the observed open form conformation of Nef would result in exposure of the dimerization interface. However, in order to validate the structural model produced from the monolayer data, measurements on a more physiologically relevant model system – such as a lipid bilayer – were necessary.

Here we used SPR to determine the affinity of full length myristoylated and non-myristoylated Nef, a dimerization defective mutant, and Nef core to charged mem-

branes and optimize conditions for NR measurements. NR was then used to probe the structure of myrNef on lipid bilayers and the resulting structural model was compared to the monolayer-bound structure. For all SPR and NR measurements the stBLMs contained PG as the charged lipid species for direct comparison with the previous NR measurements. A dimerization defective mutant (D123N) was also measured to provide evidence (albeit indirect) for dimerization by comparing the membrane-bound structures of wildtype and mutant Nef to probe for conformational changes. As expected, myristoylation was essential for membrane interactions with anionic stBLMs for both the wildtype and mutant protein. The folded Nef core was displaced from the bilayer in a position that is presumably amenable for the engagement of membrane-bound kinases while the N-terminal myristate and basic patch anchored the protein on the membrane, consistent with the previous NR measurements of myrNef on Langmuir monolayers [32]. The distance of the Nef core from the membrane depended on surface concentration of the protein and appears to differ slightly for wild-type Nef and D123N mutant.

In this work the full-length Nef (myristoylated and non-myristoylated) and D123N mutant constructs were purified by Kindra Whitlatch in the Smithgall lab at the University of Pittsburgh. The Nef core was provided by Dr. John Jeff Alvarado, also in the Smithgall lab. Mass spectrometry experiments to confirm purity, as well as the ratio of myristoylated:non-myristoylated, were conducted by Dr. Jamie A. Moroco in the Engen Lab at Northeastern University.

5.2   Results and Discussion

5.2.1   SPR Measurements of Nef Constructs to stBLMs

To probe the electrostatic contribution of the basic residues in the N-terminal arm to membrane binding, full-length –myrNef was measured on stBLMs containing 30% charge using SPR (Figure 5.3). A low salt (50 mM NaCl) buffer was required to reduce electrostatic screening and observe binding. A protein concentration range between 0.5 and 50 μM was used, and while an exact K_d could not be determined from this range, the estimated K_d is > 50 μM.

The Nef core was also measured to determine if it contributes to membrane binding in the stBLM system. Purified Nef core was measured in low salt buffer on stBLMs containing 30% negatively charged lipids (Figure 5.3). Similar to full length –myrNef, the estimated K_d is > 50 μM. However, the observed SPR response ($\sim$8 pixels) for the core was less than the response observed for full length –myrNef ($\sim$ 15 pixels). Since the SPR response is proportional to the mass at the interface, the reduced response for the core suggests there is less membrane-bound protein, although the core is also less massive than full-length Nef ($\sim$ 18 kDa vs. $\sim$ 24 kDa).
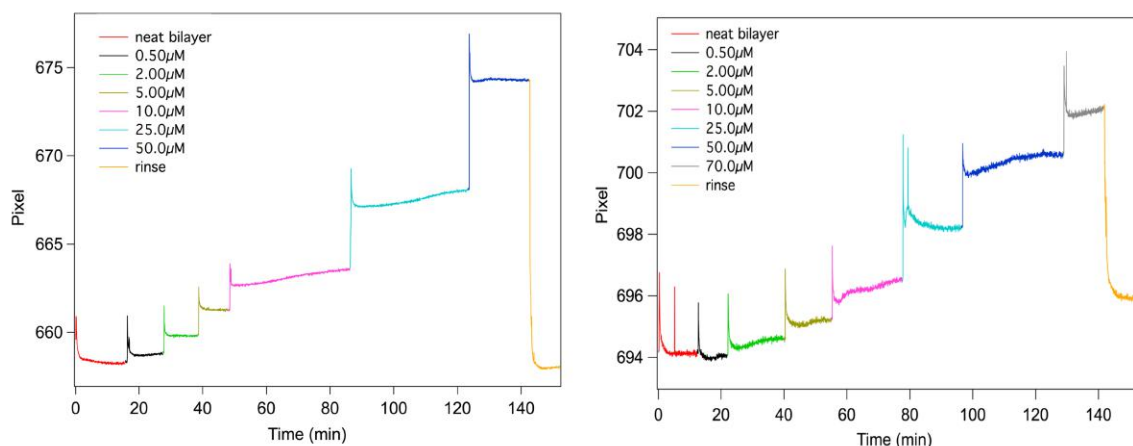
Figure 5.3: Binding of –myrNef and Nef core to stBLMs containing 30 % charge (DOPG). The contribution of the N-terminal basic residues (–myrNef; left) and the core (right) to membrane binding were measured. Both measurements were conducted in low salt, 50 mM NaCl, buffer to minimize electrostatic screening.
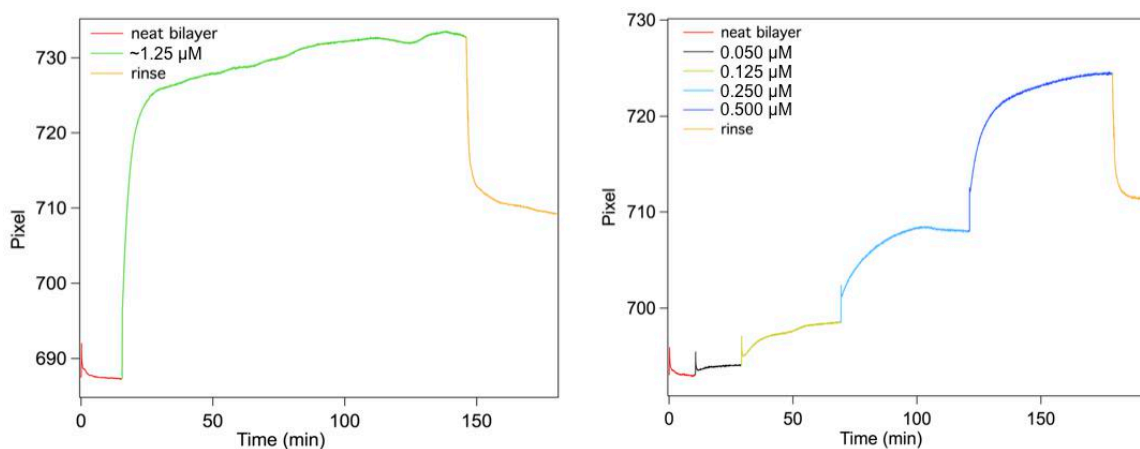
Figure 5.4: Binding of myrNef to stBLMs containing 30 % charge (POPG). Significant signal changes (binding) were observed for myrNef at concentrations in the low micromolar range. While the protein is from a mixed stock of ∼1:1 –myr:myrNef, for the range of concentrations tested –myrNef does not contribute to membrane binding. As such, all concentrations have been adjusted to represent the concentration of myrNef added to the system.

To obtain myristoylated protein, Nef was coexpressed with N-myristoyltransferase (NMT), and the E. coli cells containing the expression vector were supplemented with myristic acid. NMT catalyzed the transfer of the myristate to glycine residue 2 on the N-terminal of Nef. However, for Nef this transfer was not 100% efficient. As a result, the purified protein was a mixture of myristoylated and non-myristoylated Nef. For the wildtype protein, the mixture was ~1:1 –myrNef:myrNef with a total protein concentration of 10 μM. Since the stock contains a mixture of protein it is important to consider the lipidation state of the membrane-bound protein in our measurements. Only myristoylated Nef has biological relevance. Based on SPR, the membrane affinity of –myrNef is weak ($>$50 μM). For protein concentrations in the low micromolar range, no membrane binding was observed for –myrNef. As a result, even though the stock was not 100% myrNef, only the myristoylated fraction contributes to membrane binding for the concentration range used in our measurements.

Measurements were conducted using low salt buffer and stBLMs containing 30% negative charge. All protein concentrations have been corrected to represent the concentration of myristoylated protein added to the system. Due to limited protein availability, the initial SPR measurement consisted of only one titration of protein at ~1.25 μM. The SPR response was significant, ~45 pixels (Figure 5.4), and larger than the responses observed at much higher concentrations of Nef core and –myrNef. A range of myrNef concentrations, 0.05-0.5 μM, was also measured (Figure 5.4) and resulted in an observed SPR response of ~30 pixels. The K$_d$ could not be determined due to the limited titrations measured but is predicted to be in the low micromolar range.

5.2.2   Structural Characterization of Membrane-Bound myrNef

myrNef was measured with NR using the same conditions as for the SPR measurements (50 mM NaCl, stBLM with 30% PG). Three protein concentrations were used: 0.25, 0.5, and 1.25 μM. As in the interpretation of the SPR results, these concentrations have been corrected to reflect the concentration of myristoylated protein added to the system. 1.5 mL was used for each protein injection, and the protein was introduced to the flow cell manually. The protein was allowed to incubate the stBLM for one hour, then the system was rinsed and measured in D$_2$O and H$_2$O based buffers to detect tightly bound protein. For 0.25 μM myrNef there was not a significant amount of protein at the bilayer interface. For both the 0.5 and 1.25 μM concentrations protein was detected at the interface (Figure 5.5) although the surface coverage for the 0.5 μM concentration was fairly low ($<$ 10%). The CVO profile of the protein is too broad to represent a single conformation of myrNef at the bilayer interface. Instead, the protein appears to be dynamic with the majority of the protein mass—presumably the folded core—displaced from the membrane interface. Our result is consistent with previous measurements of myrNef on a highly charged Langmuir monolayers [32]. The shape of the NR profile changes slightly between the
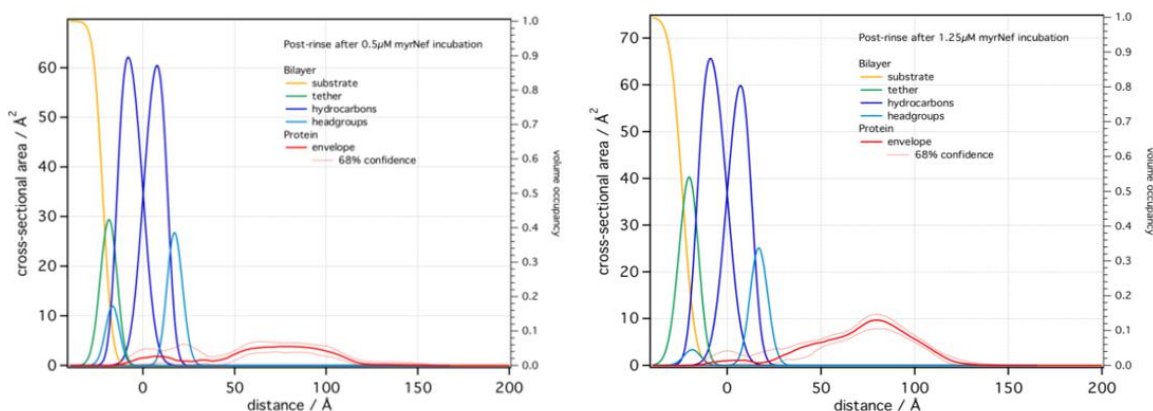
Figure 5.5: NR profiles of myrNef on a 70:30 DOPC/DOPG stBLM at 50 mM NaCl. The stBLM was incubated with 0.25, 0.5, and 1.25 μM myrNef with rinse steps in between. (Left) NR profile for 0.5 μM protein and (Right) NR profile for 1.25 μM protein. The median protein envelopes are shown with 68% confidence intervals (red trace).

two concentrations (0.5 and 1.25 μM) and may represent a concentration-dependent conformational change (Figure 5.5).

5.2.3   Nef Dimerization

Analytical gel filtration [162] and a cell-based bimolecular fluorescence complementation (BiFC) assay [37] suggest –myrNef dimers can form in solution or the cytosol (membrane association not required), respectively. For myrNef, however, dimers are not found in solution [162] or the cytosol [37]. Instead, dimers of myrNef were exclusively membrane-associated [37]. These results imply that membrane interactions are needed for myrNef dimerization. In solution, the myristoylated N-terminal arm may inhibit dimerization by interacting with the Nef core to sequester the myristoyl moiety. At the membrane, however, insertion of the myristate and the electrostatic interactions between basic residues on the N-terminal arm and charged lipid headgroups result in a separation of the core from the N-terminal region based on the NR results presented here and in [32]. This separation between the N-terminal and core would expose the dimerization interface and may lead to myrNef dimer formation on the membrane [26, 136].

With NR we are not sensitive to structural changes within the plane of the membrane, thus cannot directly determine if monomers or dimers (or both) are present at the membrane interface. To obtain evidence for the oligomerization state of myrNef at the stBLM interface, two schemes may be envisoned: (1) use a myristoylated Nef mutant defective for dimer formation ensuring a monomer species at the membrane interface or (2) measure Nef in complex with the Hck regulatory region (Unique-
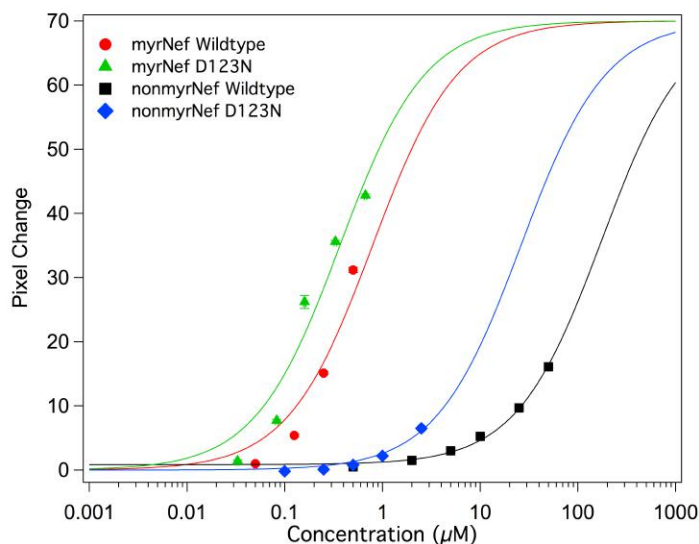
Figure 5.6: Binding curves for wildtype and D123N Nef on stBLMs containing 30% PG at 50 mM NaCl. The equilibrium response is plotted as a function of Nef concentration and fit to the Langmuir isotherm. The saturation SPR response was held at a constant value for all data sets for comparison. The binding affinity of the mutant was tighter than wildtype for both the non-myr and myr conditions.

SH3-SH2-linker) which has been shown to stabilize Nef dimers [183]. For (relative) simplicity, we used scheme one with the dimerization defective mutant. Scheme two would require deuteration of one of the proteins in order to distinguish between the two proteins (Hck vs. Nef) in the complex. In the dimerization defective mutant D123N, aspartate residue 123—which flanks the dimerization interface—is mutated to asparagine. In cells this mutation resulted in a loss of enhanced viral infectivity and CD4 and MHC-1 downregulation [38]. Differences in the NR profiles of the mutant and wildtype protein, such as difference in the displacement of the core from the stBLM interface, may be indicative of Nef dimer formation.

The binding of myristoylated and non-myristoylated D123N to charged membranes was measured. Similar to the wildtype measurements, myristoylation was essential for membrane interactions. For the measurements of myristoylated mutant the stock protein had a ∼1:2 mixture of –myr:myrD123N. For the concentration range measured all membrane binding is due to myristoylated protein. Thus, the SPR and NR measurements have been adjusted to reflect the concentration of myristoylated D123N added to the system. While the measurement needs to be repeated, the binding affinity for myrD123N also appears to be in the low micromolar range (K_d ∼1.5 μM). To compare the binding data for the D123N mutant with wildtype Nef, a Langmuir isotherm was used to fit the binding curves for the myristoylated and

non-myristoylated wildtype and D123N proteins (Figure 5.6). The saturation SPR response, which is one of the parameters typically determined from the fit, was held at a constant value for all data sets. Thus the only parameter determined by the fit was the membrane binding affinity, K_d. Unexpectedly, the mutant appears to bind the membrane tighter than wildype Nef for both non-myristoylated and myristoylated conditions (Figure 5.6). Dimerization should lead to the opposite trend. While these experiments should be repeated to validate the trend, the current SPR data does not provide evidence for dimer formation.
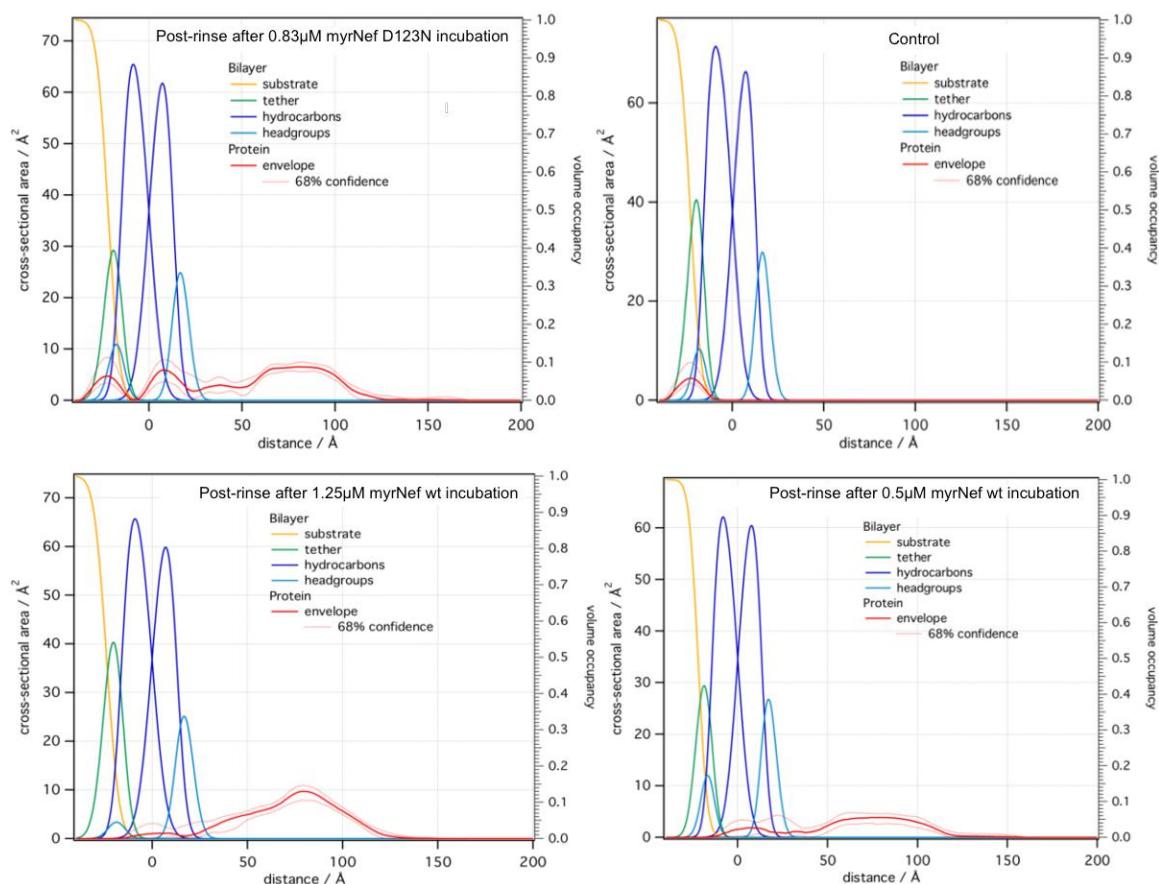
Figure 5.7: NR profiles of myristoylated D123N and wildtype Nef on a 70:30 DOPC/DOPG stBLM at 50 mM NaCl. The stBLM was incubated with protein for 1 h then the system was rinsed and any remaining, tightly bound protein was measured. The median protein envelopes are shown with 68% confidence intervals (red traces). The control fit for the mutant measurement is also shown to highlight the systematic fitting error resulting in density in the submembrane region. For all measurements the bulk of the protein is displaced from the membrane surface although the protein envelopes differ.

For wildtype Nef the dimerization interface is hydrophobic between residues Ile109 and Phe121. This hydrophobic region is flanked by two charged residues, Arg105 and Asp123 [37]. Mutation of one or both of these charged residues may result in a membrane binding interface on the Nef core, in addition to the membrane binding regions on the N-terminal arm. If an additional membrane binding interface was present on the D123N mutant, it could explain the higher affinity of the mutant for the membrane compared to wildtype. However, the NR results for the myristoylated D123N mutant do not support a secondary binding site on the Nef core. If the Nef core was binding to the membrane, the bulk of the protein should be localized on the membrane surface. Instead we observe the bulk of the protein displaced from the membrane, similar to what was observed for the wildtype myrNef (Figure 5.7).

5.3 Conclusions

For both wildtype Nef and the D123N mutant we found the folded Nef core displaced from the bilayer in a position presumably favorable for interactions with membrane-bound kinases, such as Itk and Hck, in agreement with previous NR measurements on Langmuir monolayers. While the NR profiles differ slightly between the mutant and wildtype proteins, it is difficult to conclude if this is due to the mutant adopting a different conformation on the membrane or if the differences are simply concentration-dependent. Perhaps these interpretations are not mutually exclusive as dimerization is concentration-dependent. For wildtype myrNef there was a change in the protein envelope at the higher concentration ($\sim$1.25 μM) while the lower concentration ($\sim$0.5 μM) is similar to the mutant profile. Only one concentration of myrD123N has been measured ($\sim$0.83 μM after the correction) so far. While inconclusive from the currently available data, it is possible that the observed concentration-dependent conformational change for the wildtype protein is related to dimerization. To investigate this further, higher concentrations of D123N should be measured to determine if a similar concentration-dependent conformational change is observed for the mutant. If the mutant exhibits the same behavior, this would suggest the change is purely concentration dependent and independent of dimerization. If only the wildtype protein undergoes concentration-dependent conformational changes, however, it may be indicative of dimerization.

Chapter 6

Toward a Membrane-Bound Structure of the Nef:Itk Complex

Itk, the predominant Tec kinase in T-cells, appears to be exploited by HIV-1 during multiple steps in the viral lifecycle. The role of Itk in HIV-1 infection and propagation has been linked to its interaction with Nef, a viral accessory protein. To characterize the biophysical aspects of Nef function via kinase interaction, we aim to reconstitute complexes of Nef with Itk at a membrane interface using stBLMs. However, before probing the complex, the interaction between Itk and stBLMs should first be characterized. Due to difficulties with expression and purification of the isolated membrane binding (PH) domain of Itk, two alternative constructs were investigated to optimize experimental conditions.

6.1 Introduction

Protein tyrosine kinases (PTK) are involved in signal transduction leading to cellular responses such as cell growth and differentiation in multicellular eukaryotes [39, 171]. PTKs catalyze the transfer of a phosphate group to tyrosine residues of target proteins which regulates the activity of the target protein through changes in conformation, subcelluar localization, or protein-protein interactions [39]. PTKs can be divided into two groups: receptor or non-receptor tyrosine kinases depending on whether they contain receptor-like features, such as extracellular ligand-binding and transmembrane domains [171]. Tec family kinases (TFKs) are non-receptor tyrosine kinases expressed primarily in hematopoietic cells that regulate lymphocyte development, activation, and differentiation [172–175] and serve as critical mediators of immune response in B and T-cells [176].

The Tec family is the second largest family of non-receptor tyrosine kinases and consists of five members [172, 175]. Interleukin-2 (IL-2)-inducible T-cell kinase (Itk), Tec, and Txk are expressed in T-cells while Bruton's tyrosine kinase (Btk) and Bmx (bone marrow tyrosine kinase gene on chromosome X) are expressed in B-cells and
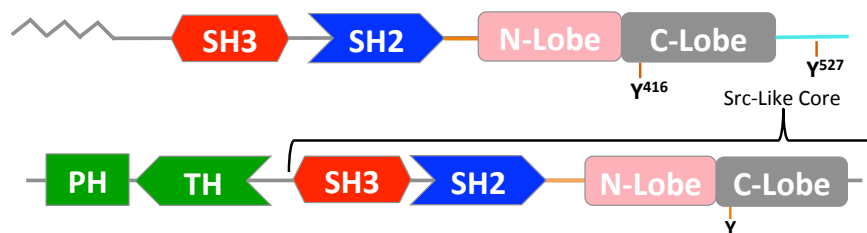
Figure 6.1: Domain organization of Src and Tec family kinases. SFK domain organization is shown on top and TFK organization is shown on bottom. (Figure provided by Kindra Whitlatch, Smithgall Lab, University of Pittsburgh).

macrophages [177]. The domain architecture of TFKs is modular with series of discrete domains connected by linker regions [171]. The domain organization of Tec kinases is similar to Src family kinases (Figure 6.1) with SH3 and SH2 regulatory domains followed by a kinase domain (Src homology 1 domain; SH1), which is divided into an N-terminal and C-terminal lobe [39, 173].

Tec kinases are expressed in HIV-1 target cells, and Itk—the predominant Tec kinase in T-cells [173, 174, 182]—has been implicated in the HIV-1 lifecycle. Loss of Itk activity with siRNA or pharmacological inhibitors resulted in decreased viral spread, transcription, and particle assembly [46], but the mechanism linking Itk and HIV-1 viral activity was not elucidated in this study. A well-understood interaction occurs between Nef and Src family kinases via the kinase SH3 domain and a Nef PxxPxR motif [40, 152, 180] and hydrophobic pocket [179] that results in constitutive kinase activation [180,181]. Since Tec kinases also contain SH3 domains, are expressed in HIV-1 target cells, and there is a link between Itk activity and viral replication, our collaborators in the Smithgall lab at the University of Pittsburgh Medical School investigated the direct interaction between Nef and Tec kinases.

Based on BiFC assays, three members of the Tec family, Bmx, Btk, and Itk, interact with Nef [41]. Since HIV-1 targets CD^+ T-cells, where Itk is the predominant Tec kinase [173,174,182], the interaction between Nef and Itk was probed further with the BiFC assay. A strong interaction was found between Itk and allelic variants of Nef from all major HIV-1 subtypes. In addition, a small molecule inhibitor selective for Itk was shown to block HIV-1 infectivity and replication in a Nef-dependent manner but did not affect replication of Nef-defective HIV-1 [41]. As such, recruitment of Itk appears to be a conserved and important feature of Nef mediated HIV-1 infection, and this signaling pathway presents a potential target for anti-retroviral drug development.

Both Itk and Nef target the the plasma membrane, and, based on the BiFC assay, the Nef:Itk complex is also localized at the plasma membrane [41]. Unlike Nef (and Src family kinases), Tec kinases are not N-terminally lipidated. Instead, with the exception of Bmx, they contain an N-terminal PH domain that binds

to phosphatidylinositol-3,4,5-triphosphate (PIP_3) on the inner leaflet of the plasma membrane [173, 174]. Therefore, membrane localization of Tec kinases is sensitive to the activities of phosphatidylinositol 3-kinase (PI3K), which produces PIP_3, and lipid phosphatases, such as phosphatase and tensin homologue (PTEN) and SH2-domain containing inositol-5-phosphatase (SHIP), which catalyze the breakdown of PIP_3 [174]. Multiple structures have been solved for individual domains of Tec kinases (PH, SH3, SH2, kinase; summarized in [39]). However, no structure has yet been solved for a full-length Tec kinase. In addition, no structure has been solved for full-length Nef (as discussed in Chapter 5). Crystal structures do exist for the SH3-SH2 domain of Src family kinases in complex with the Nef core [183] and provide a foundation for understanding the Nef:kinase interaction. However, crystal structures cannot elucidate the role of the membrane in complex formation or address how the membrane modulates the Nef:kinase interaction.

To characterize the biophysical aspects of Nef function via kinase interaction, we aim to reconstitute complexes of Nef with Tec kinases at a membrane interface utilizing the stBLM system. Before probing the Nef:Itk complex, the interaction between Itk and stBLMs—addressed in this chapter—should first be characterized. Due to difficulties with expression and purification of the isolated Itk PH domain, two alternative constructs were investigated to optimize experimental conditions: all domains preceding the kinase domain (PH-TH-SH3-SH2) and just the SH3-SH2 domains. Both constructs were generally aggregation prone, although conditions were identified for which the SH3-SH2 construct did not appear to aggregate. In the preliminary collaborative work presented here the Itk constructs were purified by Kindra Whitlatch in the Smithgall lab at the University of Pittsburgh.

6.2 Results and Discussion

6.2.1 SPR Measurements of Itk PH-TH-SH3-SH2

Ideally measurements would be conducted with Itk constructs of increasing length starting with the PH domain, which is essential for membrane targeting [174], then adding one domain at a time (PH-TH-SH3, PH-TH-SH3-SH2) before characterizing full-length kinase. However, the aggregation prone nature of the Itk PH domain [184] precluded the study of this isolated domain. The only construct containing the PH domain that was amenable for overexpression and purification was a PH-TH-SH3-SH2 construct. While this construct is more complex with its four domains, it allows the membrane interactions of the PH domain to be probed. The PH-TH-SH3-SH2 construct was measured on stBLMs containing 50 mol % PA (50:50 DOPA:DOPC) at a physiologically relevant salt concentration of 150 mM NaCl. DOPA was chosen as the anionic component based on a Lipid Strip assay which showed a minor "hit" for PA. Lipid Strips are commercially available assays in which biologically relevant
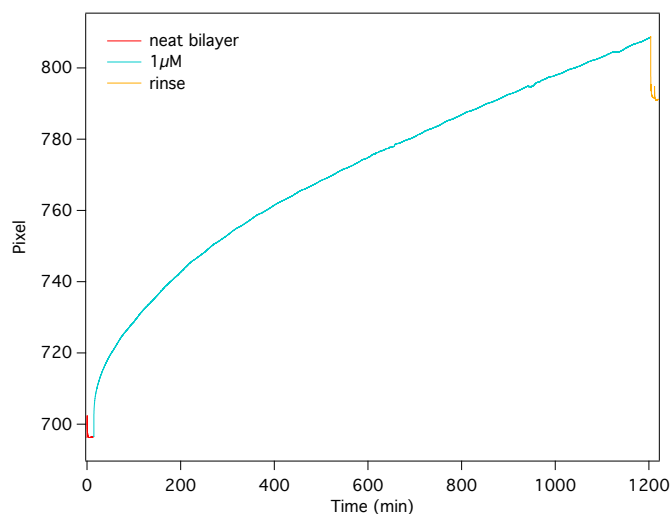
Figure 6.2: Binding of Itk PH-TH-SH3-SH2 to stBLMs containing 50% DOPA at 150 mM NaCl. A single concentration, 1 μM PH-TH-SH3-SH2, titrated into the system and allowed to incubate the stBLM for ~20 hrs before the system was rinsed. The signal continuously increased over the entire measurement time. The overall signal change is ~100 pixels. Rinsing resulted in only a slight decrease in the signal, suggesting the aggregates remain on the interface.

lipids are dotted onto a cellulose blotting membrane. The purified protein is allowed to incubate the cellulose membrane followed by a buffer rinse. Lipid-bound protein (remains after the buffer rinse) is then detected using primary and secondary antibodies. Since the interaction appeared weak on the Lipid Strip, membrane charge beyond what is physiologically relevant, was used to enhance the electrostatic attraction. It should be noted, however, PS is the main anionic lipid in the inner leaflet of the PM [102,129]. Incubation of the construct with the PA-containing stBLM resulted in large SPR responses, ~80-100 pixels, for relatively low concentrations (≤ 1 μM). The signal did not plateau over the course of a full day (Figure 6.2) to two days (data not shown), which suggests the protein is aggregating at the membrane interface under these conditions.

6.2.2 SPR Measurements of Itk SH3-SH2

While the PH-domain has been implicated in recruitment of Itk to the plasma membrane in cells [174], the SH2 domain may also engage in membrane interactions. Recently it has been reported that SH2 domains are also capable of lipid interactions via charged patches on their surface which are distinct from the known phosphotyrosine binding pocket [47, 185]. Tec kinases Itk, Btk, and Bmx were shown to have high nanomolar affinity (200-500 nM) for PM mimetic vesicles containing
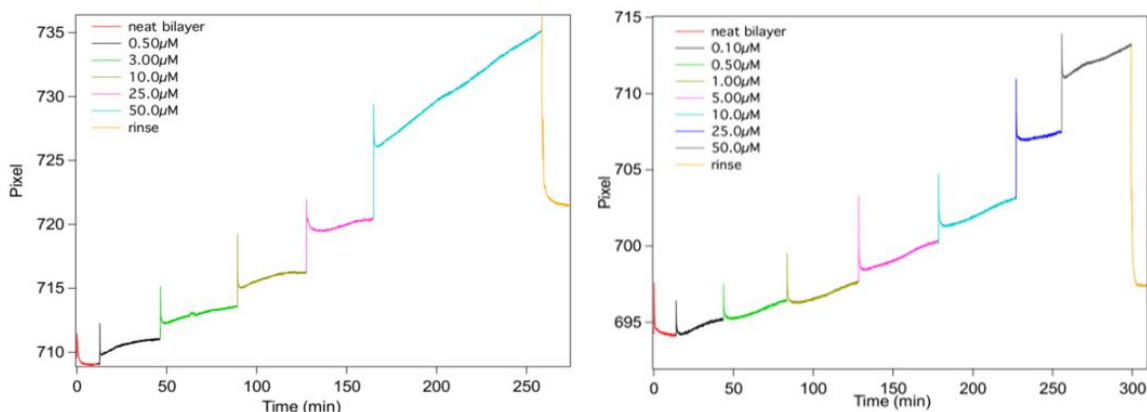
Figure 6.3: Binding of Itk SH3-SH2 to stBLMs containing PIP lipids at 50 mM NaCl. (Left) Binding of SH3-SH2 to stBLMs containing 75:20:5 DOPC:DOPS:PI(3,4,5)P_3. (Right) Binding of SH3-SH2 to stBLMs containing 75:23:2 DOPC:DOPS:PI(4,5)P_2. On the PIP$_3$ containing stBLMs the aggregation signal was not observed until relatively high concentrations > 25 μM of protein, whereas the aggregation signal was observed for all titrations on the PIP$_2$ containing stBLMs.

POPC/POPE/POPS/PI/Cholesterol/PI(4,5)P_2 12:35:22:8:22:1 [47].

Using POPC/POPS/PIP (77:20:3) vesicles, Park *et al.* (2016) also measured the specificity of the SH2 domains for specific PIPs. The SH2 domains of Itk and Btk exhibited low selectivity for PIPs while Bmx was selective for PI(4,5)P_2 over PI(3,4,5)P_3 followed by other PIP lipids [47]. Since the SH2 domain also appears to have membrane binding capability, a soluble SH3-SH2 construct was used to optimize buffer and stBLMs compositions as an alternative to the aggregation prone PH-containing construct.

At physiological salt concentrations on 50:50 DOPA:DOPC stBLMs the signal continuously increased over the measurement time, similar to what was observed for the PH-containing construct. The stBLM composition was adjusted to replace PA with PS, decrease the charge to a more physiologically relevant amount (20 mol%), and include PI(3,4,5)P_3 (5 mol%). While the SPR response was minimal, ∼6 pixels for 30 μM SH3-SH2, the aggregation behavior of the construct was reduced for the PC:PS:PIP$_3$ stBLM composition. To decrease electrostatic shielding the salt concentration of the buffer was decreased from 150 mM to 50 mM NaCl. For concentrations ≤ 25 μM the signals plateaued, indicating equilibrium was achieved (Figure 6.3). The SPR response, however, remained small (∼10 pixels). Higher concentrations, 40 or 50 μM, resulted in a continuously increasing signal, again indicating slow aggregation on the system. When PIP$_3$ was replaced with PI(4,5)P_2 (2 mol%) an "aggregation signal" was observed for all protein additions (Figure 6.3).
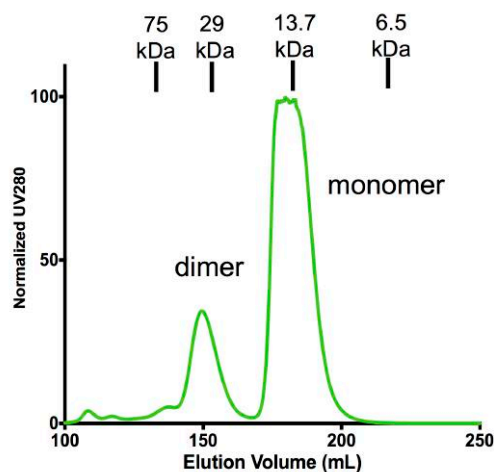
Figure 6.4: The Itk SH3-SH2 construct forms two species in solution. The purified recombinant Itk SH3-SH2 protein was run on a Superdex 75 HiLoad 26/60 prep column and eluted as two peaks consistent with monomeric and dimeric forms. The elution peaks of the calibration standards are shown at the top. (Figure provided by Kindra Whitlatch, Smithgall Lab, University of Pittsburgh).

In solution the SH3-SH2 domain is in an equilibrium between a monomeric and dimeric state based on gel filtration chromatography (Figure 6.4). Membrane interactions, however, appear to induce further oligomerization/aggregation based on the observed SPR signals. In our measurements this aggregation often prohibited a detailed analysis of the protein/membrane interactions. However, one condition was identified for which aggregation was not observed: PIP_3 containing stBLMs at protein concentrations ≤ 25 μM. From the data set presented here a K_d could not be determined due to the limited measurement points. However, the data does not support a binding affinity in the nanomolar or even low micromolar range, as reported by Park *et al.* (2016) for isolated SH2 domains on PIP-containing vesicles [47]. Since our construct contained both the SH2 and SH3 domains, the difference in binding affinity may be due to the SH3 domain modulating the lipid binding behavior of the SH2 domain. The membrane interactions of the isolated SH2 domain should be measured using the stBLM system to validate this hypothesis.

6.3   Conclusions

The propensity of Itk to aggregate presents challenges for expression, purification, as well as biophysical measurements seeking to characterize membrane interactions. As an alternative to aggregation-prone Itk, another Tec kinase, Btk, may be used instead. Unlike Itk, the PH-TH domain of Btk is readily expressed as a soluble protein [184],

which should allow for measurements of lipid interactions of the isolated PH domain then constructs of increasing domain length. Like Itk, Btk is expressed in HIV-1 target cells and was shown to interact with Nef in the BiFC assay [41] making it an attractive and viable alternative for biophysical characterization.

Chapter 7

Lipid binding by the N-terminal Unique region of the Src family kinase Hck

The N-terminal disordered domains of Src family kinases are the only regions without high sequence and structural homology between family members, which suggests they are important for both cellular localization and, as a result, downstream signaling. The SFK Hck is naturally expressed as two isoforms that differ only in their N-terminal region, making Hck an ideal candidate to probe the mechanisms that drive localization/membrane targeting. Here we used SPR to probe the electrostatic interactions between SH4-U (the N-terminal region) of the p61 isoform of Hck in a non-myristoylated form and charged stBLMs to determine if charge alone is enough to drive membrane binding. NR was then used to measure the membrane-bound state. SPR was also used to obtain preliminary results on how the regulatory domains (SH3, SH2) modulate lipid interaction of the SH4-U region using a SH4-U-SH3 p61 Hck construct.

7.1 Introduction

SFKs are the largest family of non-receptor tyrosine kinases. The family is composed of nine members: Src, Lck, Lyn, Blk, Hck, Fyn, Yrk, Fgr, and Yes. These kinases are membrane-associated and act as signaling intermediates in a variety of pathways including cell proliferation, differentiation, apoptosis, migration and metabolism [48, 186, 187]. All SFK members share a common domain organization (Figure 7.1) with a large C-terminal kinase domain (SH1), two regulatory domains (SH2 and SH3), and a lipidated membrane-anchoring domain (SH4) at the N-terminal [48, 186]. An intrinsically disordered segment known as the Unique (U) domain, connects the SH4 and SH3 domains [48].

Fig. 1 Schematic representation of a full-length
membrane-associated SFK. SH4-U-SH3-SH2-
[kinase domain], in the down-regulated-inactive
conformation.
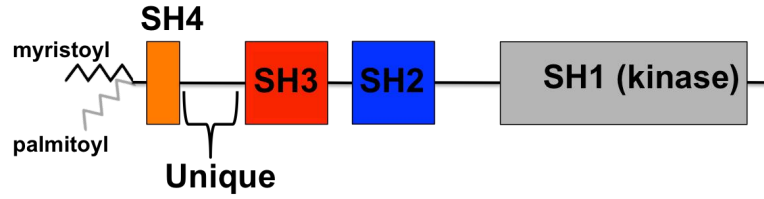
Figure 7.1: Domain organization of SFKs The N-terminus
of SFKs is myristoylated and can also be palmitoylated. This is followed
by an intrinsically disordered Unique domain that connects it to the regulatory SH3
(red) and SH2 (blue) domains. The C-terminal contains the kinase, or SH1, domain
(gray).

While the SH3, SH2, and kinase domains exhibit high amino acid sequence homology
and structural similarity among all SFK members, the SH4-Unique regions show large
sequence diversity (Figure 7.2) [48,186]. Yet, for each individual SFK, the sequence
of the Unique domains are well conserved across different species (Figure 7.2) [48],
suggesting a role for the Unique domain beyond just that of a simple spacer or linker.
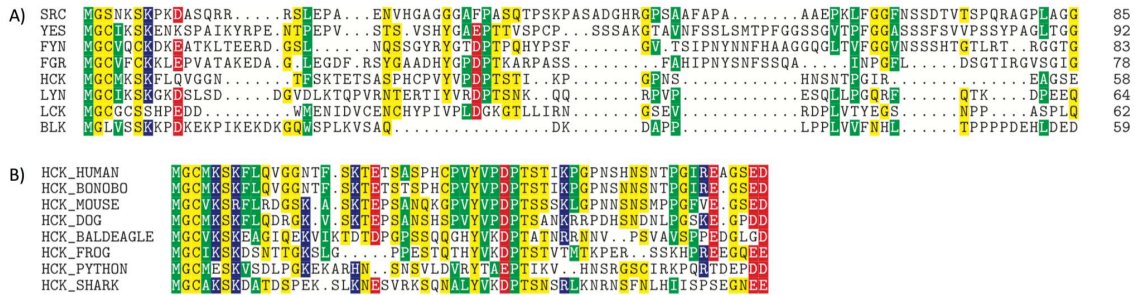
**Figure 7.2: Sequence comparison of the N-terminal disordered regions of
SFKs** (A) There is low sequence conservation in the SH4-Unique region between the
different Src kinases. (B) There is conservation of this region for each individual
SFK across different species with Hck (the p59 isoform) shown as an example. Acidic
residues are highlighted in red, basic in blue, polar in yellow, and hydrophobic in
green. (Figure from the Roux Lab, U. Chicago).

The high degree of similarity between the folded domains (SH1-3) and the diver-
sity of the SH4-Unique (SH4-U) region suggest that SFK localization, and as a result
function, is dictated by the disordered region (SH4-U). Recent studies with c-Src—the
prototypical SFK—confirmed the relevance of SH4-U for both localization and func-
tion [49,50]. A partially structured region was discovered in the Unique region [49]
that acts as a novel lipid binding site, distinct from the known SH4 lipid binding site,

with an affinity for acidic lipids [50]. Based on Lipid Strip assays, c-Src SH4-U interacts with PA, cardiolipin (CL), PS, phosphatidylinositol-4-phosphate (PI(4)P), and PI(3,4,5)P$_2$. Lipid binding was modulated by the presence of the SH3 domain. c-Src constructs that contained both the SH4-U region and the SH3 domain no longer interacted with PIP lipids on the Lipid Strips but still interacted with other acidic lipids. NMR experiments confirmed SH4-U lipid binding is modulated by interactions with the SH3 domain, as well as phosphorylation and binding to calcium-bound calmodulin [50]. Swapping the Unique domain of c-Src with that of other SFKs interchanged their functional specificity [188, 189]. These studies of c-Src support an active role for SH4-U in SFK regulation. However, due to the diversity of the disordered regions among the different SFKs, the mechanisms that regulate membrane association of the SH4-U region of c-Src cannot be generalized to other SFKs without validation. In addition, how the other domains (SH3, SH2, kinase) modulate the function of the SH4-U region requires further study.

In terms of probing the mechanisms of the SH4-U region, the SFK Hck is of particular interest because it is the only SFK naturally expressed as two isoforms: p59 and p61. These two isoforms are generated by alternative initiations of translation of a single mRNA [191] and only differ in their N-terminal region with the p61 isoform containing an additional 21 residues [186, 190]. While both isoforms can be myristoylated on glycine residue 2, with the p59 isoform more likely to be myristoylated than p61 [191], the p59 isoform can also be palmitoylated on cysteine 3 [190, 191]. The differences in the N-terminal residues and the acylation state for these two isoforms result in different cellular localization. The p59 isoform is found primarily at the plasma membrane while the p61 isoform is primarily associated with lysosomes [190, 191]. Both the inner leaflet of the PM and the lysosomal membrane are enriched in acidic lipids. The inner leaflet of the PM contains ∼25-30% negative charge based on studies of human erythrocytes [23], and the lysosome contains ∼15-20% based on the phospholipid analysis of rat liver lysosomes [192].

In general, Hck represents an important target for drug discovery since constitutive Hck activation occurs in several blood cancers [193, 194] and has also been implicated in HIV-1 infection through interactions with Nef. Hck, which is highly expressed in macrophages [195], is one of two SFKs that are expressed in HIV-1 target cells [195, 196]. Nef-mediated constitutive Hck activation occurs via interactions between the Nef PxxPxR motif and the Hck SH3 domain [152] and contributes to enhanced viral replication [42, 43] and immune evasion through the downregulation of MHC-1 [44, 45]. In addition, Nef skews the localization of Hck to the Golgi [195, 197] (in non-infected cells both Hck isoforms are found at the Golgi in low levels [190]) where it arrests the cytokine receptor Fms [195, 197]. Arresting Fms in the Golgi interferes with the M-CSF signaling pathway essential for macrophage survival and may contribute to loss of immune system homeostasis in HIV infection [195–197]. Since SH4-U is important for substrate specificity, which also influences downstream targets, understanding this region may lead to the discovery of new intermediate

states and drug targets to inhibit unregulated kinase activity.

Since the SH4-U region is intrinsically disordered, and thus does not adopt a single molecular structure, it is especially challenging for traditional structure determination methods. Inclusion of a lipid membrane, necessary to study the protein in its biologically relevant state, adds further challenges. Here we measured the interaction between the p61 isoform of Hck and stBLMs using constructs of increasing length (SH4-U, SH4-U-SH3) as a first step to determining the interactions that regulate membrane binding, including the modulation of SH4-U lipid interactions by the SH3 domain. In future work the SH4-U and SH4-U-SH3 regions of p59 isoform will be measured to characterize the differences in the membrane interactions for the two Hck isoforms. Even longer constructs of both isoforms will be investigated (SH4-U-SH3-SH2 and full length kinase) to determine if other domains, beyond the SH3 domain which has already been shown to modulate the lipid binding behavior of SH4-U [50], further modulate the membrane interactions of Hck.

7.2   Results and Discussion

7.2.1   Biochemical pre-characterization of Hck p61 SH4-U

Dr. Matthew Pond, a postdoctoral fellow in the Roux Lab (University of Chicago), has expressed, purified, and initiated biochemical characterization of the SH4-U region of the p61 isoform of Hck. SDS-PAGE, size exclusion chromatography, and circular dichroism confirm that the construct is intrinsically disordered (Figure 7.3) in solution, as expected. Lipid Strips (Echelon Biosciences, Salt Lake City, UT) were used to screen for lipid interactions, as was done for the SH4-U region of c-Src [50]. The SH4-U construct was expressed with a C-terminal strep-tag that binds to commercially available anti-strep antibodies. The strep-tagged protein was allowed to incubate the Lipid Strips and then detected using the antibody and enhanced chemiluminescence. The p61 SH4-U interacted with PA and to a lesser extent PI(4)P (data not shown). Both lipids are of potential biological importance for Hck p61 subcellular localization since PA is enriched in the lysosome [192] and has been reported to drive interactions of various proteins with the lysosome [192, 198]. PI(4)P is found in high concentrations in the Golgi [102].

7.2.2   SPR Measurements of the Membrane Interactions of Hck p61 SH4-U

In vivo, myristoylation is necessary for membrane association [191], but basic residues in the N-terminal region were also identified as important for high affinity lipid interactions for Src [199]. The construct we used was not myristoylated, which allows us to specifically probe the electrostatic contribution to membrane binding. However, this interaction alone (without the myristate) does not result in a high affinity binding, so
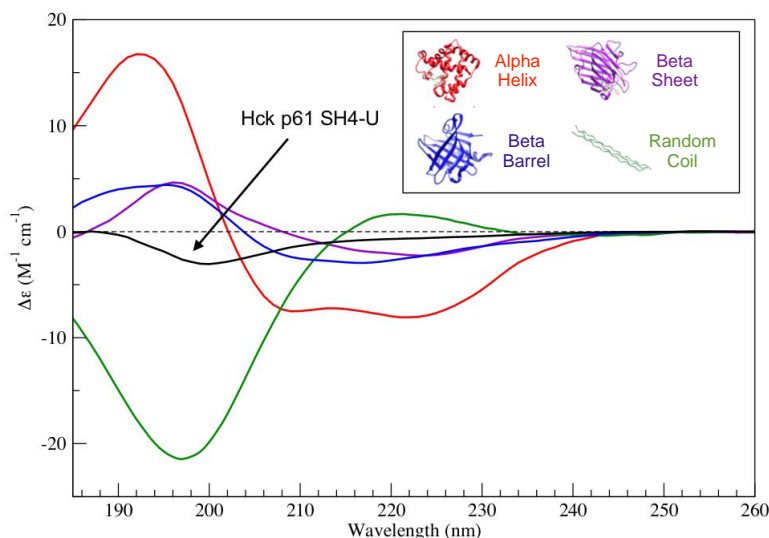
Figure 7.3: CD spectra of Hck p61 SH4-U Confirms Intrinsic Disorder
The molar circular dichroism ($\Delta\epsilon$) plotted as a function of wavelength. Examples of common protein secondary structures (α helix, β sheet, β barrel),as well as random coil, and the CD spectra associated with those structures are shown for comparison. The CD spectra of Hck p61 SH4-U indicates a lack of well-formed secondary structure. (Data from Dr. M. Pond, U. Chicago).

a low salt buffer (10 mM Tris) at pH 8 was used to decrease electrostatic screening. In addition, the charge on the membrane was increased to 50% for preliminary measurements. Even in low salt buffer and on highly charged membranes, Hck p61 SH4-U appeared to have low affinity for the membrane with only minimal SPR responses for protein additions in the low micromolar range. Thus, a wide range of protein concentrations reaching the upper micromolar range was used. SPR measurements were conducted with stBLMs containing DOPA and PI(4)P, as well as DOPS, cholesterol, and pure DOPC to test for lipid specificity. Since the SPR signal is proportional to the mass at the interface, the SPR responses for SH4-U, which is only ∼8 kDa, are smaller than for larger proteins discussed earlier (∼15-30 kDa).

SPR confirmed specificity of Hck p61 SH4-U to PA, in agreement with the Lipid Strip assay. However, Hck p61 SH4-U did not interact with PI(4)P—the other lipid identified in the Lipid Strip assay–based on SPR. Essentially no membrane binding was observed for stBLMs that did not contain PA. The PA interaction does not appear to be simply due to the small headgroup size or general charge since neither the inclusion of cholesterol nor another anionic lipid (PS) resulted in substantial membrane association (Figure 7.4). The largest SPR responses were observed for stBLMs con-
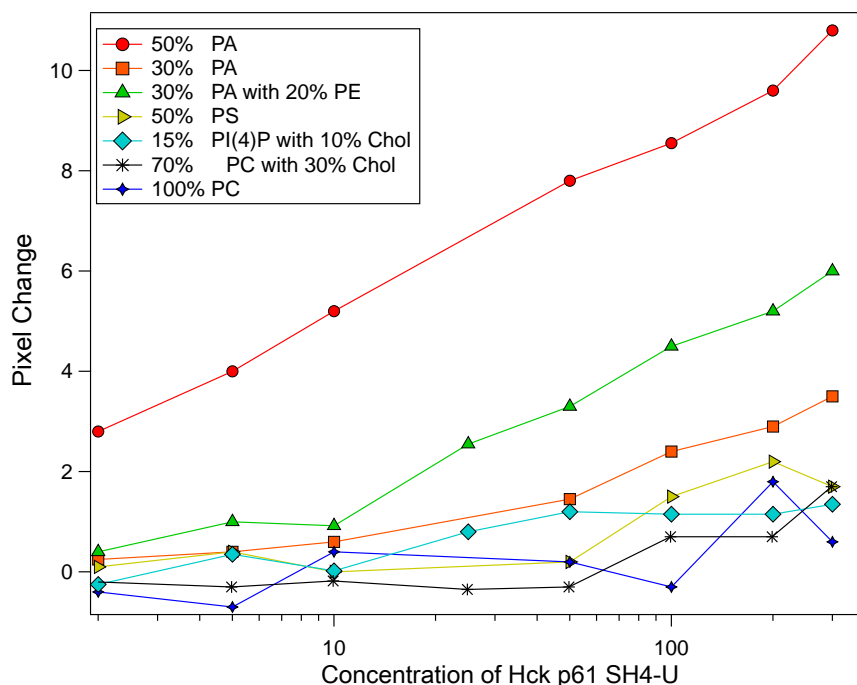
Figure 7.4: SPR response for Hck p61 SH4-U The SPR response was plotted as a function of p61 SH4-U concentration. The data has been corrected for the bulk effect on the response. Binding was observed for PA-containing membranes, however, the overall responses are small. The largest SPR responses were observed for 50% PA stBLMs. The symbols represent the measured data points, which did not fit to standard binding models. The lines connecting the data points have been added as a visual guide (do not represent a fit to the data).

taining 50% DOPA (Figure 7.4 and Table 7.1). While binding was observed for 30% DOPA, it was minimal. Inclusion of DOPE into a stBLM containing 30% DOPA, however, significantly increased the binding of p61 SH4-U with the SPR response doubling for 30% PA bilayers with 20% PE (Table 7.1). Increased affinity for PA when PE is present in the membrane has also been observed for other proteins that bind specifically to PA, such as the Raf kinase [200]. PE can act as a hydrogen bond donor and increase the charge on PA from -1 to -2 [201], and it may also facilitate the insertion of hydrophobic residues due to its small headgroup size [202].

The binding curves generated from the SPR measurements of Hck p61 SH4-U are shown in Figure 7.4, however, the data did not fit to standard binding models. In Le Roux *et al.* (2015), SPR was used to measure the binding of the N-terminal region of c-Src to liposomes. At concentrations > 20 μM a change in the binding behavior was observed, thus only concentrations ≤ 20 μM were included in the fit to the binding curve [204]. Due to the small SPR responses we observed for Hck

SH4-U, however, it is difficult to just use concentrations <20 μM in our analysis. In addition, Le Roux *et al.* (2015) observed a complex membrane binding behavior of the c-Src N-terminal with a labile and persistent binding mode. Based on these two binding modes, a "conformational-change"-like model was proposed in which the protein transitions from an initial membrane-bound state to a persistently-bound state that is irreversible [204]. A similar transition may be occurring during our measurements of Hck SH4-U, which would explain why standard binding models did not describe the data.

Table 7.1: SPR response for Hck p61 SH4-U on PA-containing stBLMs in low salt buffer

	SPR response (in pixels) for PA-containing stBLMs		
Concentration	50:50 PA:PC	30:70 PA:PC	30:20:50 PA:PE:PC
2 μM	2.8	0.25	0.4
5 μM	4	0.4	1
10 μM	5.2	0.6	0.92
50 μM	7.8	1.45	3.3
100 μM	8.55	2.4	4.5
200 μM	9.6	2.9	5.2
300 μM	10.8	3.5	6

Table 7.2: Measured and expected SPR response for Hck p61 SH4-U on 100% PC

	SPR response (in pixels) due to bulk changes	
Concentration	Measured	Expected
2 μM	-0.4	0
5 μM	-0.7	0
10 μM	0.6	0.2
50 μM	1.1	0.9
100 μM	1.5	1.8
200 μM	5.4	3.6
300 μM	6	5.4

The high concentrations of Hck SH4-U used for the SPR measurements impacted the bulk optical index resulting in signal changes that were not due to protein interactions with the membrane. A correction was applied to the SPR responses (as

described in Chapter 2) that takes into account the contribution from the bulk. Assuming the SPR response from p61 SH4-U with a pure zwitterionic stBLM (100% DOPC) is due entirely to bulk effects, and not protein adsorption, the measured pixel changes should be in agreement with the estimated pixel changes for the bulk contribution to the SPR signal, which is what we observe (Table 7.2). In addition, the refractive index increment for the protein is dn/dc =0.189 $\pm$ 0.07 mL/g from the measured SPR responses, which is consistent with expected value of 0.185 mL/g for proteins [203].

7.2.3 NR Measurements of the Membrane Interactions of Hck p61 SH4-U

NR also confirmed specificity of Hck p61 SH4-U to PA. For our measurements with PA-containing stBLMs a significant amount of protein was detected at the interface ($\geq$ 12% volume occupancy) under the conditions tested. Three concentrations of the protein, 10 μM, 50 μM, and 300 μM, were measured on stBLMs containing 50% DOPA. The protein was incubated on the membrane for a few hours (1-3 h) then the system was rinsed and any remaining protein was detected. The amount of protein at the interface was similar for all three concentrations with the peak density only increasing from $\sim$12% volume occupancy (at 10 μM) to $\sim$15% volume occupancy (at 300 μM). For the 30% DOPA, two concentrations, 10 μM and 50 μM, were measured during the protein incubation. The system was rinsed with buffer following the 50 μM incubation to detect any remaining, tightly bound protein. While instrumental difficulties introduced larger errors on our fit, the results appear similar to what was observed for 50% PA with volume occupancies around $\sim$12 % and only a slight increase in the amount of protein at the interface for the higher concentration. Rinsing the system did not decrease the amount of bound protein or result in a change in the shape of the profile. For both 50% PA and 30% PA the protein was partially inserted into the membrane and remained bound after a buffer rinse (Figure 7.5). When another anionic lipid was used (30% PG), however, no protein was detected at the interface for a 100 μM concentration. Thus, the interaction between p61 SH4-U and PA is not simply electrostatic.

7.2.4 Persistent Membrane Binding of the Hck p61 SH4-U domain

While the NR and SPR results agree on the specificity of Hck SH4-U for PA, the NR measurements yielded results in terms of surface coverage/saturation that were unexpected from the SPR data. From the SPR data we would expect an increase in the volume occupancy as the concentration of protein is increased. For the 50% PA NR measurement, the amount of protein at the interface increased only slightly from $\sim$12% volume occupancy at 10 μM to $\sim$15% volume occupancy at 300 μM even though
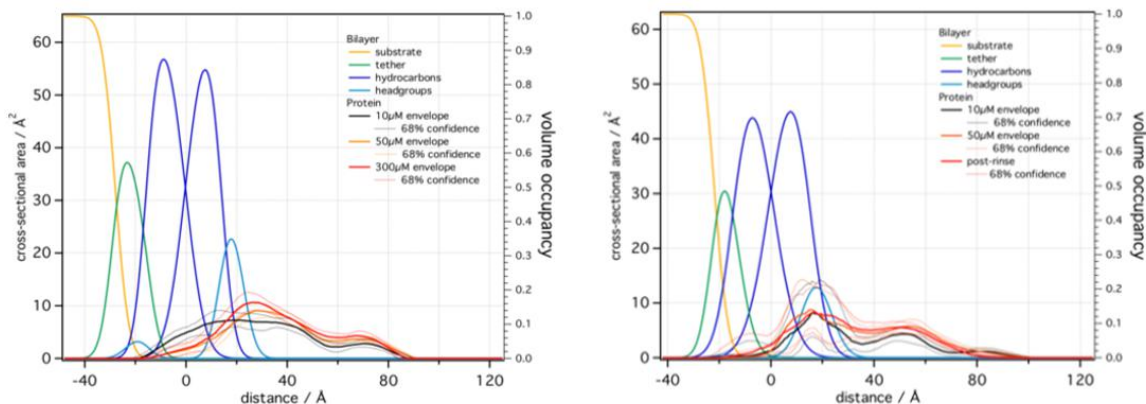
Figure 7.5: NR profiles for Hck p61 SH4-U on PA-containing stBLMs
(Left) Three concentrations, 10 μM (black), 50 μM (orange), and 300 μM (red), on
a 50:50 DOPA:DOPC stBLM measured after a rinse step. (Right) Two incubations,
10 μM (black) and 50 μM (orange), and a post-rinse measurement (red) on a 30:70
DOPA:DOPC stBLM. For all conditions there is a significant amount of protein at
the interface and it is partially inserted. However, instrumental difficulties introduced
a large uncertainty on the 30% PA measurement.

the SPR response doubled between these two concentrations (Table 7.1). The same
trend was observed for the 30% PA measurement with similar volume occupancies
for the two concentrations even though the SPR response more than doubled from
between 10 μM and 50 μM Hck SH4-U. Based on the NR data, it appears the system
is saturated, or close to saturation, at 10 μM SH4-U.

For the membrane binding measurements of the N-terminal of c-Src [204], the
system also appeared to be saturated at 10 μM protein. However, even larger SPR
responses were observed for 50 and 100 μM with a change in binding behavior that
deviates from equilibrium. Le Roux *et al.* (2015) postulated a slow binding process,
which occurs at every concentration, dominates the SPR signal at high concentra-
tions. This slow binding process was indicative of a persistent binding mode in which
the protein is irreversibly bound to the membrane. The rate of formation of the
persistently bound state was the same for charged and neutral liposomes at pro-
tein concentrations $\geq$10 μM even though the binding affinity was higher for charges
liposomes [204].

Our NR and SPR data support a slow binding process resulting in a persistently
bound state for the Hck p61 SH4-U. For the SPR measurements each concentration of
SH4-U was incubated on the stBLM for $\sim$10-20 min. Taking into account all protein
additions, the total amount of time protein was on the system was $\sim$60-70 min. For
the NR measurements, each protein addition was incubated on the system for at
least 60 min. For the 50% PA condition, the incubation time was 60 min for the 10

μM concentration and 3 hrs (each) for the 50 and 300 μM concentrations. For the 30% PA condition the incubation time was 6 hrs. The longer incubation times allow for accumulation of the protein at the interface through the slow binding/persistent binding mode such that saturation is reached by 10 μM for both 50% and 30% PA. It is clear from the NR data Hck SH4-U is persistently bound since protein remains at the stBLM interface after the system is rinsed with buffer.

For the N-terminal region of c-Src [204] myristoylation was required for the persistently bound state. When the myristic acid was replaced with lauric acid, which has a 12-carbon chain instead of a 14-carbon chain, the difference in acyl chain length was enough to eliminate the persistent state [204]. The Hck construct we used, however, is not myristoylated, yet we still observed a persistently bound state (at least in the low salt buffer used for measurements). In terms of lipid binding, c-Src and Hck p61 SH4-U exhibit differences in specificity. The N-terminal of c-Src binds to acidic lipids [50] while Hck p61 SH4-U exhibits specificity for PA based on the SPR data presented here. Several proteins have been identified that bind specifically to PA [205], but they are diverse and do not exhibit sequence homology [200]. The only commonality is the presence of basic amino acids [206], which is not unexpected since the phosphomonoester headgroup of PA is negatively charged. However, electrostatics cannot explain the specificity for PA, especially since PA is not the most abundant anionic lipid in eukaryotic cells [102]. In Kooijman *et al.* (2007) NMR revealed basic residues (lysine and arginine) are able to form hydrogen bonds with the PA phosphomonoester headgroup increasing the charge of PA from -1 to -2. From these results an electostatic/hydrogen bond switch mechanism was proposed in which the protein is first attracted to the membrane through electrostatics, then hydrogen bonds form with the PA headgroups which increases the charge on PA enhancing the electrostatic attraction. The coupling between electrostatics and hydrogen bonds locks the basic residues with PA and docks the protein on the PA-containing membrane [200]. The electrostatic/hydrogen switch mechanism used to attract PA-specific proteins to their target membranes offers an explanation for the differences in persistent binding for the N-terminal regions of c-Src and Hck. Even though the Hck p61 SH4-U was not myristoylated in these measurements, the formation of hydrogen bonds could act as an anchor keeping the protein at the interface long enough for change to the persistently bound state to occur even without the myristate.

7.2.5 Lipid Interactions of Hck p61 SH4-U-SH3

In addition to the novel lipid binding site on the Unique domain, Perez *et al.* (2013) found a lipid binding site on the SH3 domain of c-Src on the opposite face from the well-known PxxP binding site. Contacts were also identified between the SH3 and Unique domains on the same face as the lipid binding site. The interaction between the SH3 and Unique domains seems to modulate the lipid binding behavior of c-Src since SH4-U and SH4-U-SH3 constructs interacted with different lipids on the Lipid
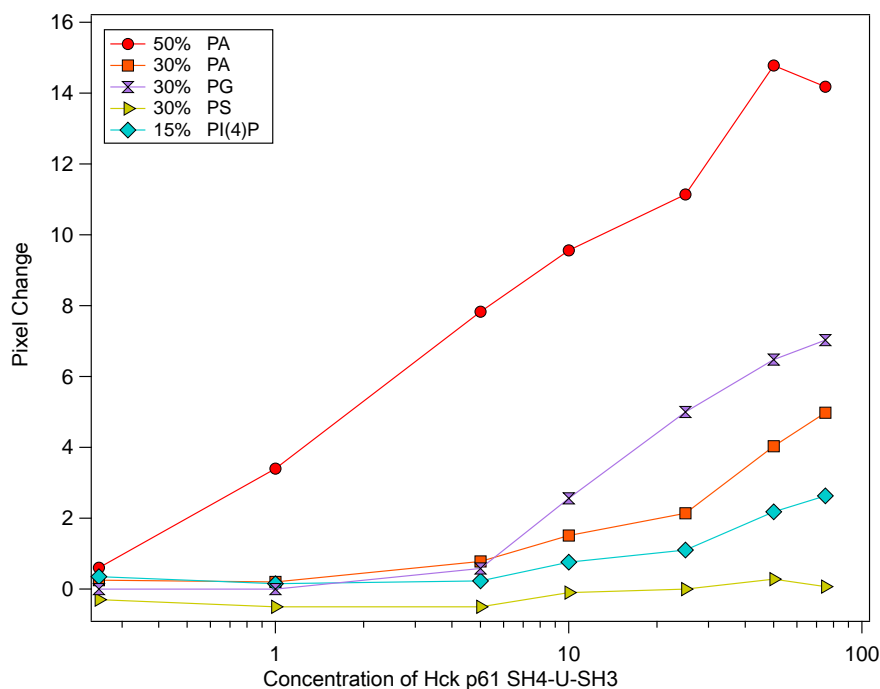
Figure 7.6: SPR response for Hck p61 SH4-U-SH3 The SPR response was plotted as a function of p61 SH4-U-SH3 concentration. The data has been corrected for the bulk effect on the response. Binding was observed for PA-containing membranes and not PS- or PI(4)P- containing membranes, which is consistent with the binding of the small SH4-U construct. For the longer construct, however, binding was also observed for PG-containing stBLMs. The symbols represent the measured data points, and the lines connecting them have been added as a visual guide.

Strip assay [50]. We conducted preliminary SPR measurements with a Hck p61 SH4-U-SH3 construct to determine if the SH3 domain changes the lipid interactions of the SH4-U domain previously measured (Figure 7.6). Inclusion of the SH3 domain did not alter the membrane binding behavior of the Hck SH4-U region to PA, PS, and PI(4)P containing stBLMs. Binding was observed between Hck SH4-U-SHU and PA-containing membranes but not PS and PI(4)P. However, the two constructs exhibited differences in binding for PG-containing stBLMs. Binding was observed to PG-containing stBLMs for Hck SH4-U-SH3 with SPR responses that were slightly larger than those observed for 30% PA stBLMs (Figure 7.6). Hck SH4-U was not detected on PG-containing stBLMs using NR under conditions that were identical to the measurements with PA. The interaction between SH4-U and PG was not measured using SPR. NR measurements should be conducted with Hck SH4-U-SH3 on PA and PG-containing stBLMs to confirm the lipid-interactions and determine if the interactions lead to the same conformation. In addition, the Hck SH4-U-SH3 NR

results can be compared to the SH4-U work presented here to determine if the SH3 domain modulates the membrane-bound structure of Hck SH4-U.

7.3   Conclusions

The SH4-U region of the Hck p61 isoform exhibited specificity for PA. This interaction led to a persistently-bound state, which we propose is due to an electrostatic/hydrogen switch mechanism. In the persistently bound state, which is not removed by rinsing, the protein is partially inserted into the membrane. The lipid binding behavior of the SH4-U region appears to be modulated by the SH3 domain resulting in interactions with PA and PG lipids, based on SPR measurements. In addition to their known role in regulatory the activity of the kinase domain, the regulatory domains (SH3 and SH2) may also modulate the lipid association of SFKs.

Conclusions

This work focused on membrane-associated proteins involved in the lifecycle of HIV-1: the myristoylated matrix domain of the Gag polyprotein (Chapter 4), the accessory protein Nef (Chapter 5), and two host cell tyrosine kinases constitutively activated by Nef (Chapters 6, 7). SPR and NR were used to measure the protein/membrane interactions and determine binding affinities and membrane-bound structures, respectively. Since membrane-association is key to the function of these proteins, elucidating their interactions with and at the membrane helps further our understanding of HIV-1 infection and propagation. The current study of myrMA is an important step toward a full structural characterization of HIV-1 Gag membrane-binding and viral assembly, and the work with Nef and associated tyrosine kinases represent a first step towards determining the structure(s) of a membrane-bound Nef:kinase complex.

For myrMA we showed the effect of pH on the dynamics of the myristoyl sequestration pocket and determined the effect of myristoylation on the structural organization of MA bound to a charged membrane. The combination of hydrophobic and electrostatic interactions resulted in a protein orientation that is distinct from the purely electrostatic association, and this re-orientation positioned key residues favorably for engagement of PI(4,5)P$_2$ (Chapter 4). Complex, PE-based stBLMs were also developed as model membrane mimics of the inner leaflet of the PM using an adapted osmotic shock vesicle fusion method for bilayer formation (Chapter 3). As an application of these complex membranes, the effect of the complex PE stBLM on the binding affinity of myrMA was measured. Inclusion of PE was found to modestly increase the affinity of myrMA for cholesterol containing charged membranes (Chapter 4). A PM mimic containing relevant phosphoinositides was also developed to be used in future MA work (Chapter 3).

For wildtype Nef and a dimerization defective mutant, we found the folded Nef core displaced from the bilayer in a position presumably favorable for interactions with membrane-bound kinases, such as Itk and Hck, in agreement with previous NR measurements on Langmuir monolayers. The distance of the Nef core from the membrane was dependent on the surface concentration of the protein and appeared to differ slightly between the wildtype and mutant, although repeat measurements are needed (Chapter 5). The long-term goal of the Nef project is to determine the membrane-bound structure(s) of Nef in complex with Tec (or Src) kinases. Before probing the complex, the interactions of the kinase with the membrane (in the ab-

sence of Nef) should be measured. Unfortunately, the Tec kinase Itk was difficult to purify and aggregation prone (Chapter 6). Alternatives to Itk, such as another Tec kinase with better solution behavior or a Src kinase, may be needed for future work. While the Src kinase Hck is of general interest due to its interactions with Nef, the N-terminal disordered region (SH4-U) of Src kinases warrant their own study. The SH4-U region is the only region without high sequence and structural homology between the different Src kinases, and studies have shown this region is important for localization and downstream function, although the mechanisms have not been fully elucidated. For the p61 isoform of Hck, it appears the SH4-U region specifically targets PA lipids, and the PA/protein interaction can result in a persistently bound state through an electrostatic/hydrogen bond switch mechanism. The persistently bound state is not removed after rinsing and results in partial membrane-insertion. Inclusion of other regulatory domains, such as SH3, may modulate the interactions of the SH4-U region, and the membrane interactions of constructs of increasing length should be measured (Chapter 7).

Beyond their role in HIV-1 infection, the proteins studied here are connected because they are soluble peripheral membrane proteins. Soluble peripheral membrane proteins, also known as "conditional membrane proteins" [208], transition from the cytosol to a membrane-bound state(s) under specific conditions in order to perform their function. These proteins bind selectively to cellular membranes by recognizing specific lipid components in the target membrane (such as PIPs), as well as physical properties of the membrane itself (charge and curvature). Membrane interactions, even transient ones, can lead to structural rearrangements or conformational changes in the protein, which means the solution structure of these proteins may not provide sufficient information to fully understand how the protein performs its function. To gain a full-understanding of the biological processes in which these proteins are involved, it is essential to study the proteins in a membrane environment that mimics the cell. However, the transient nature of the membrane interaction, and the variety of protein conformations that can occur during the interaction, pose unique challenges for the structure determination. Detailed knowledge of the membrane binding characteristics and aggregation behavior of the protein, such as through SPR experiments, can be used to optimize experimental conditions before structural characterization is pursued. The name "conditional membrane protein" is apt as conditions often need to be manipulated, for example by decreasing the ionic strength or altering the pH of the buffer, to stabilize one particular conformation.

To determine the structure of the peripheral protein in its membrane-bound state, NR offers distinct advantages including: the ability to incorporate model membranes of biologically relevant lipid compositions; a fully-buffer immersed sample with a high flexibility in regards to buffer conditions (pH, ionic strength, and temperature) including, but not limited to, physiologically relevant ranges; the ability measure disordered or partially disordered proteins; and non-destructive measurements that allow the sample to be manipulated during a measurement such that biological processes

can be simulated *in situ*. In addition, even though the intrinsic resolution of NR is lower than traditional structure determination methods, a fully atomistic interpretation can be achieved with integrated modeling strategies that utilize complementary experimental data and MD simulations. With the development of in-plane fluid tethered membranes optimized for NR and the implementation of molecular modeling strategies, NR can be routinely applied to the study of membrane-associated proteins.

Acronyms

β**ME** β-mercaptoethanol. 9

−**myr** non-myristoylated. 4

AIDS acquired immune deficiency syndrome. 2

BiFC bimolecular fluorescence complementation. 66

Btk Bruton's tyrosine kinase. 70

CPE constant phase element. 14

CVO component volume occupancy. 28

d$_{31}$-POPC 1-palmitoyl-d31-2-oleoyl-sn-glycero-3-phosphocholine. 11

D123N dimerization defective Nef mutant. 62

DMPC 1,2-dimyristoyl-sn-glycero-3-phosphocholine. 11

DOPA 1,2-dioleoyl-sn-glycero-3-phosphate. 72

DOPC 1,2-dioleoyl-sn-glyero-3-phosphocholine. 11

DOPE 1,2-dioleoyl-sn-glycero-3-phosphoethanolamine. 11

DOPS 1,2-dioleoyl-sn-glyero-3- phospho-L-serine. 11

ECM equivalent circuit model. 14

EIS electrochemical impedance spectroscopy. 9

ESI electrospray ionization. 45

HBR highly basic region. 42

HC18 Z20(Z-octadec-9-enyloxy)-3,6,9,12,15,18,22-heptaoxatetracont-31-ene-1-thiolacetate. 9

Hck Hemopoietic Cell Kinase. 6

HDX-MS hydrogen deuterium exchange with mass spectrometry. 46

HIV human immunodeficiency virus. 2

Itk Interleukin-2 Inducible T-Cell Kinase. 6

$\mathbf{K}_d$ equilibrium dissociation constant (binding affinity). 18

LTR long terminal repeat. 59

MA matrix. 3

MHC-1 class I major histocompatibility complex. 59

MS mass spectrometry. 45

myr myristoylated. 4

Nef negative regulatory factor. 4

NR neutron reflectometry. 2

nRTK non-receptor tyrosine kinases. 6

nSLD neutron scattering length density. 23

OSVF osmotic shock vesicle fusion. 34

PA phosphatidic acid. 72

PC phosphatidylcholine. 36

PDB protein data bank. 30

PE phosphatidylethanolamine. 4

PG phosphatidylglycerol. 62

PH pleckstrin homology domain. 6

PI L-α-phosphatidylinositol. 11

PI(3,4,5)P$_3$; PIP$_3$ phosphatidylinositol-3,4,5-triphosphate. 11

PI(4)P phosphatidylinositol-4-phosphate. 11

PI(4,5)P$_2$; PIP$_2$ L-α-phosphatidylinositol-4,5-bisphosphate. 11

PIP phosphoinositide. 38

PM plasma membrane. 1

POPC 1-palmitoyl-2-oleoyl-sn-glycero-3-phosphocholine. 11

POPE 1-palmitoyl-2-oleoyl-sn-glycero-3-phosphoethanolamine. 11

POPS 1-palmitoyl-2- oleoyl-sn-glycero-3-phospho-L-serine. 11

PS phosphatidylserine. 37

PTK protein tyrosine kinases. 70

RSE rapid solvent exchange. 34

SAM self-assembled monolayer. 10

SERINC serine incorporator. 59

SFKs Src family kinases. 6

SH1 Src homology 1. 70

SH2 Src homology 2. 6

SH3 Src homology 3. 6

SH4 Src homology 4. 77

SH4-U Src homology 4 and Unique domains. 77

SPR surface plasmon resonance. 2

stBLM sparsely tethered bilayer lipid membrane. 9

TFKs Tec family kinases. 6

U Unique domain. 77

Bibliography

[1] W. Fu, B.E. Sanders-Beer, K.S. Katz, D.R. Maglott, K.D. Pruitt, and R.G. Ptak (2009) "Human immunodeficiency virus type 1, human protein interaction database at NCBI." Nucleic Acids. Res. **37**, D417.

[2] J.W. Pinney, J.E. Dickerson, W. Fu, B.E. Sanders-Beer, R.G. Ptak, and D.L. Robertson (2009) "HIV-host interactions: a map of virtual perturbation of the host system." AIDS **23**, 549.

[3] R.G. Ptak, W. Fu, B.E. Sanders-Beer, J.E. Dickerson, J.W. Pinney, D.L. Robertson, M.N. Rozanov, K.S. Katz, D.R. Maglott, K.D. Pruitt, and C.W. Dieffenbach (2008) "Cataloguing the HIV type 1 human protein interaction network." AIDS Res. Hum. Retroviruses **24**, 1497.

[4] C. Baum, A. Schambach, J. Bohne, and M. Galla (2006) "Retrovirus vectors: toward the plentivirus." Molecular Therapy **13**, 1050.

[5] S.P. Goff (2007) "Host factors exploited by retroviruses." Nat. Rev. Microbiol. **5**, 253.

[6] R.A. Dick and V.M. Vogt (2014) "Membrane interaction of retroviral Gag proteins." Front. Microbiol. **5**, 187.

[7] J.M. Coffin, S.H. Hughes, and H.E. Varmus, eds. (1997) *Retroviruses* Cold Spring Harbor Laboratory Press, Cold Spring Harbor, NY.

[8] S. Nyamweya, A. Hegedus, A. Jayne, S. Rowland-Jones, K.L. Flanagan, and D.C. Macallan (2013) "Comparing HIV-1 and HIV-2 infection: lessons for viral immunopathogensis." Rev. Med. Virol. **23**, 221.

[9] S. Scarlata and C. Carter (2003) "Role of HIV-1 Gag domains in viral assembly." Biochim. Biophys. Acta. **1614**, 62.

[10] H.M. Temin (1982) "Function of the retrovirus long terminal repeat." Cell **28**, 3.

[11] I.M. Jones and Y. Morikawa (1998) "The molecular basis of HIV capsid assembly." Rev. Med. Virol. **8**, 87.

[12] A. Ono (2009) "HIV-1 assembly at the plasma membrane: Gag trafficking and localization." Future Virol. **4**(3), 241.

[13] M. Bryant and L. Ratner (1990) "Myristoylation-dependent replication and assembly of human immunodeficiency virus 1." Prot. Natl. Acad. Sci. U.S.A. **87**(2), 523.

[14] W. Zhou, L.J. Parent, J.W. Wills, and M.D. Resh (1994) "Identification of a membrane-binding domain with the amino-terminal region of human immunodeficiency virus type 1 Gag protein which interacts with acidic phospholipids." J. Virol. **68**(4):2556.

[15] P. Spearman, R. Horton, L. Ratner, and I. Kuli-Zade (1997) "Membrane binding of human immunodeficiency virus type 1 matrix protein in vivo supports a conformational myristyl switch mechanism." J. Virol. **71**(9):6582.

[16] E.O. Freed, G. Englund, and M.A. Martin (1995) "Role of the basic domain of human immunodeficiency virus type 1 matrix in macrophage infection." J. Virol. **69**(6):3949.

[17] A. Ono, J.M. Orenstein, and E.O. Freed (2000) "Role of the Gag matrix domain in targeting human immunodeficiency virus type 1 assembly. J. Virol. **74**(6):2855.

[18] J.S. Saad, J. Miller, J. Tai, A. Kim, R.H. Ghanam, and M.F. Summers (2006) "Structural basis for targeting HIV-1 Gag proteins to the plasma membrane for virus assembly." Prot. Natl. Acad. Sci. U.S.A. **103**(30), 11364.

[19] W. Zhou, and M.D. Resh (1996) "Differential membrane binding of the human immunodeficiency virus type 1 matrix protein." J. Virol. **70**:8540.

[20] P.Y. Mercredi, N. Bucca, B. Loeliger, C.R. Gaines, M. Mehta, P. Bhargava, P.R. Tedbury, L. Charlier, N. Floquet, D. Muriaux, C. Favard, C.R. Sanders, E.O. Freed, J. Marchant, and M.F. Summers (2016) "Structural and molecular determinants of membrane binding by the HIV-1 matrix protein." J. Mol. Biol. **428**, 1637.

[21] H. Nanda, S.A.K. Datta, F. Heinrich, M. Löesche, A. Rein, S. Krueger and J.E. Curtis (2010) "Electrostatic interactions and binding orientation of HIV-1 matrix studied by neutron reflectivity." Biophy. J. **99**(8), 2516.

[22] M. Barros, F. Heinrich, S.A.K. Datta, A. Rein, I. Karageorgos, H. Nanda, and M. Löesche (2016) "Membrane binding of HIV-1 matrix protein: dependence on bilayer composition and protein lipidation." J. Virol. **90**, 4544.

[23] J.A. Virtanen, K.H. Cheng, and P. Somrharju (1998) "Phospholipid composition of the mammalian red cell membrane can be rationalized by a super lattice model." Proc. Nat. Acad. Sci. **95**(9), 4964.

[24] R. Eells, M. Barros, K.M. Scott, I. Karageorgos, F. Heinrich, and M. Löesche (2017) "Structural characterization of membrane-bound human immunodeficiency virus-1 Gag matrix with neutron reflectometry." Biointerphases **12**, 02D408.

[25] H.W. Kestler, D.J. Ringler, K. Mori, D.L. Panicali, P.K. Sehgal, M.D. Daniel, and R.C. Desrosiers (1991) "Importance of the nef gene for maintenance of high virus loads and for development of AIDs." Cell **65**(4), 651.

[26] S.T. Arold, and A.S. Baur (2001) "Dynamic Nef and Nef dynamics: how structure could explain the complex activities of this small HIV protein." Trends Biochem. Sci. **26**(6), 356.

[27] A. Bauer (2004) "Functions of the HIV-1 Nef protein." Curr. Drug Targets Immune Endocr. Metabol. Disord. **4**(4), 309.

[28] G.H. Renkema and K. Saksela (2000) "Interactions of HIV-1 NEF with cellular signal transducing proteins." Front. Biosci. **5**, D268.

[29] J.W. Marsh (1999) "The numerous effector functions of Nef." Arch. Biochem. Biophys. **365**(2), 192.

[30] M.A. Goldsmith, M.T. Warmerdam, R.E. Atchison, M.D. Miller, and W.C. Greene (1995) "Dissociation of the CD4 downregulation and viral infectivity enhancement functions of human immunodeficiency virus type 1 Nef." J. Virol. **69**(7), 4112.

[31] M. Harris (1995) "The role of myristoylation in the interactions between human immunodeficiency virus type 1 Nef and cellular proteins." Biochem. Soc. Trans. **23**(3), 557.

[32] B. Akgun, S. Satija, H. Nanda, G.F. Pirrone, X. Shi, J.R. Engen, and M.S. Kent (2013) "Conformational transition of membrane-associated terminally acylated HIV-1 Nef." Structure **21**(10), 1822.

[33] G.F. Pirrone, L.A. Emert-Sedlak, T.E. Wales, T.E. Smithgall, M.S. Kent, and J.R. Engen (2015) "The membrane-associated conformation of HIV-1 Nef investigated with hydrogen exchange mass spectrometry at a Langmuir monolayer." Anal. Chem. **87**(14), 7030.

[34] E.A. Pereira and L.L.P. daSilva (2016) "HIV-1 Nef:Taking control of protein trafficking." Traffic **17**, 976.

[35] M. Geyer, C.E. Munte, J. Schorr, R. Kellner, and H.R. Kalbitzer (1999) "Structure of the anchor-domain of myristoylated and non-myristoylated HIV-1 Nef protein." J. Mol. Biol. **289** 123.

[36] S. Grzesiek, A. Bax, J.S. Hu, J. Kaufman, I. Palmer, S.J. Stahl, N. Tjandra, and P.T. Wingfield (1997) "Refined solution structure and backbone dynamics of HIV-1 Nef." Protein Sci. **6**, 1248.

[37] J.A. Poe and T.E. Smithgall (2009) "HIV-1 Nef dimerization is required for Nef-mediated receptor downregulation and viral replication." J. Mol. Bio. **394**, 329.

[38] L.X. Liu, N. Heveker, O.T. Fackler, S. Arold, S.L. Gall, K. Janvier, B.M. Peterlin, C. Dumas, O. Schwartz, S. Benichou, and R. Benarous (2000) "Mutation of a conserved residue (D123) required for oligomerization of human immunodeficiency virus type 1 Nef protein abolishes interaction with human thioesterase and results in impairment of Nef biological functions." J. of Virol. **74**, 5310.

[39] R.E. Joseph and A.H. Andreotti (2009) "Conformational snapshots of Tec kinases during signaling." Immun. Rev. **228**, 74.

[40] K. Saksela, G. Cheng, and D. Baltimore (1995) "Proline-rich (PxxP) motifs in HIV-1 Nef bind to SH3 domains of a subset of Src kinases and are required for the enhanced growth of Nef+ viruses but not for downregulation of CD4." EMBO J. **14**, 484.

[41] S. Tarafdar, J.A. Poe, and T.E. Smithgall (2014) "The accessory factor Nef links HIV-1 to Tec/Btk kinases in an Src homology 3 domain-dependent manner." J. Biol. Chem. **289**(22): 15718.

[42] L. Emert-Sedlak, T. Kodama, E.C. Lerner, W. Dai, C. Foster, B.W. Day, J.S. Lazo, and T.E. Smithgall (2009) "Chemical library screens targeting an HIV-1 accessory factor/host cell kinase complex identify novel antiretroviral compounds." ACS Chem. Biol. **4**, 939.

[43] P.S. Narute and T.E. Smithgall (2012) "Nef alleles from all major HIV-1 clades activate Src-family kinases and enhance HIV-1 replication in an inhibitor-sensitive manner." PLoS One **7**, 32561.

[44] C.H. Hung, L. Thomas, C.E. Ruby, K.M. Atkins, N.P. Morris, Z.A. Knight, I. Scholz, E. Barklis, A.D. Weinberg, K.M. Shokat, and G. Thomas (2007) "HIV-1 Nef assembles a Src family kinase-ZAP-70/Syk-PI3K cascade to downregulate cell-surface MHC-I." Cell Host & Microbe. **1**, 121.

[45] J.D. Dikeakos, K.M. Atkins, L. Thomas, L. Emert-Sedlak, I.J. Byeon, J. Jung, J. Ahn, M.D. Wortman, B. Kukull, M. Saito, H. Koizumi, D.M. Williamson, M. Hiyoshi, E. Barklis, M. Takiguchi, S. Suzu, A.M. Gronenborn, T.E. Smithgall, and G. Thomas (2010) "Small molecule inhibition of HIV-1 induced MHC-I down-regulation identifies a temporally regulated switch in Nef action." Mol. Biol. Cell **21**, 3279.

[46] J.A. Readinger, G.M. Schiralli, J-K. Jiang, C.J. Thomas, A. August, A.J. Henderson, and P.L. Schwartzberg (2008) "Selective targeting of ITK blocks muliple steps of HIV replication." Proc. Natl. Acad. Sci. U.S.A. **105**, 6684.

[47] M-J. Park, R. Sheng, A. Silkov, D-J. Jung, Z-G. Wang, Y. Xin, H. Kim, P. Thiagarajan-Rosenkranz, S. Song, Y. Yoon, W. Nam, I. Kim. E. Kim, D-G. Lee, Y. Chen, I. Singaram, L. Wang, M.H. Jang, C-S. Hwang, B. Honig, S. Ryu, J. Lorieau, Y-M. Kim, and W. Cho (2016) "SH2 domains serve as lipid-binding modules for pTyr-signaling proteins." Mol. Cell **62**, 7.

[48] I. Amata, M. Maffei, and M. Pons (2014) "Phosphorylation of unique domains of Src family kinases." Front. Genet. **5**, 181.

[49] Y. Pérez, M. Gairí, P. Berandó, and M. Pons (2009) "Structural characterization of the natively unfolded N-terminal domain of human c-Src kinase: insights into the role of phosphorylation on the unique domain." J. Biol. Chem. **391**, 136.

[50] Y. Pérez, M. Maffei, A. Igea, I. Amata, M. Gairí, A.R. Nebreda, P. Berandó, and M. Pons (2013) "Lipid binding by the Unique and SH3 domains of c-Src suggest a new regulatory mechanism." Sci. Reports **3**, 1295.

[51] S. Oellerich, S. Lecomte, M. Paternostre, T. Heimburg, and P. Hildebrandt (2004) "Peripheral and integral binding of cytochrome c to phospholipids vesicles." J. Phys. Chem. **108**(12), 3871

[52] A.M. Whited and A. Johs (2015) "The interactions of peripheral membrane proteins with biological membrane." Chem. Phys. Lipids **192**, 51.

[53] S.A. Tatulian (2017) "Interfacial enzymes: membrane binding, orientation, membrane insertion, and activity." Methods Enzymol. **583**, 197.

[54] H.P. Wacklin (2010) "Neutron reflection from supported lipid membranes." Current Opinion in Colloid & Interface Science **15**, 445.

[55] G. Fragneto (2012) "Neutrons and model membranes." Eur. Phys. J. Special Topics **213**, 327

[56] L.A. Clifton, C. Neylon, and J.H. Lakey "Examining protein-lipid complexes using neutron scattering." Methods Mol. Biol. **974**, 119.

[57] F. Heinrich and M. Lösche (2014) "Zooming in on disordered systems: neutron reflection studies of proteins associated with fluid membranes." Biochim. Biophys. Acta. **1838**(9), 2341.

[58] M. Belička, Y. Gerelli, N. Kučerka, and G. Fragneto (2015) "The component group structure of DPPC bilayers obtained by specular neutron reflectometry." Soft Matter **11**(31), 6275.

99

[59] S.A.K. Datta, F. Heinrich, S. Raghunandan, S. Krueger, J.E. Curtis, A. Rein, and H. Nanda (2011) "HIV-1 Gag Extension: conformational changes require simultaneous interaction with membrane and nucleic acid." J. Mol. Biol. **406**(2), 205.

[60] D.J. McGillivray, G. Valincius, F. Heinrich, J.W.F. Robertson, D.J. Vanderah, W. Febo-Ayala, I. Ignatjev, M. Lösche and J.J. Kasianowicz (2009) "Structure of functional *Staphylococcus auerus* α-Hemolysin C in tethered bilayer membranes." Biophys. J. **96**(4), 1547.

[61] F. Heinrich, H. Nanda, H.Z. Goh, C. Bachert, and M. Lösche (2014) "Myristoylation restricts the orienation of the GRASP domain on membranes and promotes membrane tethering." J. Biol. Chem. **289**(14), 9683.

[62] H. Nanda, F. Heinrich, and M. Lösche (2015) "Membrane association of the PTEN tumor suppressor: neutron scattering and MD simulations reveal the structure of protein-membrane complexes." Methods **77-78**, 136.

[63] D.J. McGillivray, G. Valincius, D.J. Vanderah, W. Febo-Ayala, J.T. Woodward, F. Heinrich, J.J. Kasianowicz, and M. Lösche (2007) "Molecular-scale structural and functional characterization of sparsely tethered bilayer lipid membranes." Biointerphases **2**(2), 21.

[64] F. Heinrich, T. Ng, D.J. Vanderah, P. Shekhar, M. Mihailescu, H. Nanda, and M. Lösche (2009) "A new lipid anchor for sparsely tethered bilayer lipid membranes." Langmuir **25**(7), 4219.

[65] R. Budvytyte, G. Valincius, and G. Niaura, V. Voiciuk, M. Mickevicius, H. Chapman, H-Z. Goh, P. Shekhar, F. Heinrich, S. Shenoy, M. Lösche, and D.J. Vanderah (2013) "Structure and properties of tethered bilayer lipid membranes with unsaturated anchor molecules." Langmuir **29**(27), 8645.

[66] S. Shenoy, R. Modovan, J. Fitzpatrick, D.J. Vanderah, M. Deserno, and M. Lösche (2010) "In-plane homogeneity and lipid dynamics in tethered bilayer lipid membranes (tBLMs). Soft Matter **2010**(6), 1263.

[67] B.A. Cornell, V.L. Braach-Maksvytis, L.G. King, P.D. Osman, B. Raguse, L. Wieczorek, and R.J. Pace (1997) "A biosensor that uses ion-channel switches." Nature **387**, 580.

[68] G. Valincius, T. Meškauskas, and F. Ivanauskas (2012) "Electrochemical impedance spectroscopy of tethered bilayer membranes." Langmuir **28**(1), 977.

[69] E. Barsoukov and J.R. Macdonald, eds. (2005) *Impedance spectroscopy: theory, experiment, and applications.* John Wiley & Sons, Inc., Hoboken, NJ.

[70] M.W. Kendig (1984) "Nonlinear current response of electrochemical systems." J. of the Electrochem. Soc. **131**(12), 2777.

[71] D.J. Vanderah, R.S. Gates, V. Silin, D.N. Zeiger, J.T. Woodward, C.W. Meuse, G. Valincius, and B. Nickel (2003) "Isostructural self-assembled monolayers. 1. Octadecyl 1-Thiaoligo(ethylene oxides)." Langmuir **19**(7), 2612.

[72] P. Shuck (1997) "Use of surface plasmon resonance to probe the equilibrium and dynamic aspects of interactions between biological macromolecules." Annu. Rev. Biophys. Biomol. Struct. **26**, 51

[73] J.R. Sambles, G.W. Bradberry, and F. Yang (1991) "Optical excitation of surface plasmons: an introduction" Contemp. Phys. **32**(3), 173.

[74] R. Schasfoort and A. Tudos, eds. *Handbook of Surface Plasmon Resonance.* Cambridge: The Royal Society of Chemistry (2008).

[75] W. Knoll (1998) "Interfaces and thin films as seen by bound electromagnetic waves." Ann. Rev. Phys. Chem. **49**, 569.

[76] E. Kretschmann and H. Raether (1968) "Radiative decay of non radiative surface plasmons excited by light." Z. Naturforsch. A. **23**, 2135.

[77] F. Heinrich (2016) "Deuteration in biological neutron reflectometry." Methods Enzymol. **566**, 211.

[78] T.L. Yap, Z. Jiang, F. Heinrich, J.M. Gruschus, C.M. Pfefferkorn, M. Barros, J.E. Curtis, E. Sidransky, and J.C. Lee (2015) "Structural features of membrane-bound glucocerebrosidase and α-synuclein probed by neutron reflectometry and fluorescence spectroscopy." J. Biol. Chem. **290**, 744.

[79] C.M. Pfefferkorn, F. Heinrich, A.J. Sodt, A.S. Maltsev, R.W. Pastor, and J.C. Lee (2011) "Depth of α-synuclein in a bilayer determined by fluorescence, neutron reflectometry, and computation." Biophys. J. **102**(3), 613.

[80] Z. Jiang, S.K. Hess, F. Heinrich, and J.C. Lee (2015) "Molecular details of α-synuclein membrane association revealed by neutrons and photons." J. Phys. Chem. B. **119**(14), 4812.

[81] S. Shenoy, P. Shekhar, F. Heinrich, M-C. Daou, A. Gericke, A.H. Ross, and M. Lösche (2012) "Membrane association of the PTEN tumor suppressor: molecular details of the protein-membrane complex from SPR binding studies and neutron reflection." PLoS One **74**, e32591.

[82] C.F. Majkrzak, E. Carpenter, F. Heinrich, N.F. Berk (2011) "When beauty is only skin deep; optimizing the sensitivity of specular neutron reflectivity for probing structure beneath the surface of thin films." J. Applied Physics **110**(10), 102212.

[83] J. Daillant and A. Gibaud, eds. *X-ray and Neutron Reflectivity: Principles and Applications* Berlin Heidelberg: Springer (2009)

[84] J.A. Dura, D.J. Pierce, C.F. Majkrzak, N.C. Maliszewskyj, D.J. McGillivray, M. Lösche, K.V. O'Donovan, M. Mihailescu, U. Perez-Salas, D.L. Worchester, S.H. White (2006) "AND/R: Advanced neutron diffractometer/reflectometer for investigation of thin films and multilayers for life sciences." Rev. Sci. Instrum. **77**(7): 74301.

[85] B.J. Kirby, P.A. Kienzle, B.B. Maranville, N.F. Berk, J. Krycka, F. Heinrich, and C.F. Majkrzak (2012) "Phase-sensitive specular neutron reflectometry for imaging the nanometer scale composition depth profile of thin-film materials." Current Opinion in Colloid & Interface Science **17**(1), 44.

[86] J. Penfold (2002) "Neutron reflectivity and soft condensed matter." Current Opinion in Colloid & Interface Science **7**, 139.

[87] J.F. Ankner and C.F. Majkrzak (1992) "Subsurface profile refinement for neutron specular reflectivity (Invited Paper)." Proc. SPIE **1738**, 260.

[88] P. Shekhar, H. Nanda, M. Lösche, and F. Heinrich (2011) "Continuous distribution model for the investigation of complex molecular architectures near interfaces with scattering techniques." J. of Applied Physics **110**, 102216.

[89] J.F. Nagle and S. Tristram-Nagle (2000) "Structure of lipid bilayers." Biochim. Biophys. Acta. **1469**, 159.

[90] H.I. Petrache, S.E. Feller, and J.F. Nagle (1997) "Determination of component volumes of lipid bilayers from simulations." Biophys. J. **72**(5), 2237.

[91] V.F. Sears (1992) "Neutron scattering lengths and cross sections." Neutron News **2**, 26.

[92] M.L. Connolly (1983) "Solvent accessible surfaces of proteins and nucleic acids." Science **221**(4612), 709.

[93] M.L. Connolly (1983) "Analytical molecular surface calculation." J. Appl. Cryst. **16**, 548.

[94] S.J. Perkins (1986) "Protein volumes and hydration effects. The calculations of partial specific volumes, neutron scattering matchpoints and 280-nm absorption coefficients for proteins and glycoproteins form amino acid sequences." Eur. J. Biochem. **157**(1), 169.

[95] J.E. Curtis, H. Zhang, and H. Nanda (2014) "SLDMOL: A tool for the structural characterization of thermally disordered membrane proteins." Comput. Phys. Commun. **185**, 3010.

[96] M.A. Massiah, M.R. Starich, C. Paschall, M.F. Summers, A.M. Christensen, and W.I. Sundquist (1994) "Three-dimensional structure of the human immunodeficiency virus type 1 matrix protein." J. Mol. Biol. **244**, 198.

[97] S. Matthews, P. Barlow, N. Clark, S. Kingsman, A. Kingsman, and I. Campbell (1995) "Refined solution structure of p17, the HIV matrix protein." Biochem. Soc. Trans. **23**(4), 725.

[98] S. Matthews, P. Barlow, J. Boyd, G. Barton, R. Russel, H. Mills, M. Cunningham, N. Meyers, N. Burns, and N. Clark (1994) "Structural similarity between the p17 matrix protein of HIV-1 and interferon-gamma." Nature **370**(6491), 666.

[99] C.P. Hill, D. Worthylake, D.P. Bancroft, A.M. Christensen, and W.I. Sundquist (1996) "Crystal structures of the trimeric human immunodeficiency virus type 1 matrix protein: implications for membrane association and assembly." Prot. Natl. Acad. Sci. U.S.A. **93**, 3099.

[100] M.D. Resh (1999) "Fatty acylation of proteins: new insights into membrane targeting of myristoylated and palmitoylated proteins." Biochimica et Biophysica **1451**, 1.

[101] C. Tang, E. Loeliger, P. Luncsford, I. Kinde, D. Beckett, and M.F. Summers (2004) "Entropic switch regulates myristate exposure in HIV-1 matrix protein." Prot. Natl. Acad. Sci. U.S.A. **101**(2), 517.

[102] G. van Meer., D.R. Voelker, and G.W. Feigenson (2008) "Membrane lipids: where they are and how they behave." Nat. Rev. Mol. Cell Biol. **9**, 112.

[103] G. Zhao, J.R. Perilla, E.L. Yufenyuy, X. Meng, B. Chen, J. Ning, J. Ahn, A.M. Gronenborn, K. Schulten, C. Aiken, and P. Zhang (2013) "Mature HIV-1 capsid structure by cryo-electron microscopy and all-atom molecular dynamics." Nature **497**(7451), 643.

[104] X. Sun, J.F. Chiu, and Q.Y. He. (2005) "Application of immobilized metal affinity chromatography in proteomics." Expert Rev. Proteomics **2**(2), 649.

[105] V. Chukkapalli and A. Ono (2011) "Molecular determinants that regulate plasma membrane association of HIV-1 Gag." J. Mol. Biol. **410**(4), 512.

[106] E.L. Fledderman, K. Fuji, R.H. Graham, K. Waki, P.E. Prevelige, E.O. Freed, and J.S. Saad (2010) "Myristate exposure in human immunodeficiency virus type 1 matrix protein is modulated by pH." Biochem. **49**(44), 9661.

[107] B. Bjellqvist, G.J. Hughes, C. Pasquali, N. Paquet, F. Ravier, J.C. Sanchez, S. Frutiger, and D. Hochstrasser (1993) "The focusing positions of polypeptides in immobilized pH gradients can be predicted from their amino acid sequences." Electrophoresis **14**(10), 1023.

[108] L. Charlier, M. Louet, L. Chaloin, P. Fuchs, J. Martinez, D. Muriauz, C. Favard, and N. Floquet. (2014) "Coarse-grained simulations of the HIV-1 matrix protein anchoring: revisiting its assembly on membrane domains." Biophys. J. **106**(3), 577.

[109] P.S. Murray, Z. Li, J. Wang, C.L. Tang, B. Honig, and D. Murray (2005) "Retroviral matrix domains share electrostatic homology: models for membrane binding throughout the viral life cycle." Structure **13**, 1521.

[110] L. O'Neil, K. Andenoro, I. Pagano, L. Carroll, L. Langer, Z. Dell, D. Perera, B.W. Treece, F. Heinrich, M. Lösche, J.F. Nagle, S. Tristram-Nagle (2016) "HIV-1 matrix-31 membrane binding peptide interacts differently with membranes containing PS vs. PI(4,5)P$_2$." Biochim. Biophys. Acta **1858**(12), 3071.

[111] Y.H. Chan and S.G. Boxer (2007) "Model membrane systems and their applications." Curr. Opin. Chem. Biol. **11**(6), 581.

[112] M.S. Khan, N.S. Dosoky, and J.D. Williams (2013) "Engineering lipid bilayer membranes for protein studies." Int. J. Mol. Sci. **14**(11), 21561.

[113] B.R. Dorvel, H.M. Keizer, D. Fine, J. Vuorinen, A. Dodabalapur, R.S. Duran (2007) "Formation of tethered bilayer lipid membranes on gold surfaces: QCM-Z and AFM study." Langmuir **23**, 7344.

[114] A.P. Serro, A. Carapeto, G. Paiva, J.P.S. Farinha, R. Colaço, and B. Saramago (2011) "Formation of an intact liposome layer adsorbed on oxidized gold confirmed by three complementary techniques: QCM-D, AFM, and confocal microscopy." Surf. Interface Anal. **44**(4), 426.

[115] I.K. Vockenroth, C. Rossi, M.R. Shah, and I. Köper (2009) "Formation of tethered bilayer lipid membranes probed by various surface sensitive techniques." Biointerphases **4**(2), 19.

[116] M. Seitz, E. Ter-Ovanesyan, M. Hausch, C.K. Park, J.A. Zasadzinski, R. Zentel, and J.N. Isaelachvili (2000) "Formation of tethered supported bilayers by vesicle fusion onto lipopolymer monolayers promoted by osmotic stress." Langmuir **16**(14), 6067.

[117] M. Tanaka and E. Sackmann (2005) "Polymer-supported membranes as models of the cell surface." Nature **437**, 656.

[118] W. Knoll, I. Köper, R. Naumann, and E-K. Sinner (2008) "Tethered biomolecular lipid membranes – a novel model membrane platform." Electrochimica Acta **53**(23), 6680.

[119] I. Köper (2007) "Insulating tethered bilayer lipid membranes to study membrane proteins." Mol. Biosyst. **3**(10), 651.

[120] A.V. Hughes, J.R. Howse, A. Dabkowska, R.A.L. Jones, M.J. Lawrence, and S.J. Rose (2008) "Floating lipid bilayers deposited on chemically grafted phosphatidylcholine surfaces." Langmuir **24**(5), 1989.

[121] C.W. Meuse, G. Niaura, M.L. Lewis, and A.L. Plant (1998) "Assessing the molecular structure of alkanethiol monolayers in hybrid bilayer membranes with vibrational spectroscopies." Langmuir **14**(7), 1604.

[122] B. Raguse, V. Braach-Maksvytis, B.A. Cornell, L.G. King, P.D.J. Osman, R.J. Pace, and L. Wieczorek (1998) "Tethered lipid bilayer membranes: formation and ionic reservoir characterization." Langmuir **14**(3), 648.

[123] G.J. Hardy, R. Nayak, and S. Zauscher (2013) "Model cell membranes: techniques to form complex biomimetic supported lipid bilayers via vesicle fusion." Curr. Opin. Colloid Interface Sci. **18**(5), 448.

[124] A. Zachowski (1993) "Phospholipids in animal eukaryotic membranes: transverse and movement." Biochem. J. **294**, 1.

[125] D.L. Daleke (2008) "Regulation of phospholipid asymmetry in the erythrocyte membrane." Curr. Opin. Hematol **15**, 191.

[126] J.N. Israelachvili (1992) *Intermolecular and surface forces.* 2nd ed. Academic, Santa Barbara, CA.

[127] D. Marsh (2007) "Lateral pressure profile, spontaneous curvature frustration, and the incorporation and conformation of proteins in membranes." Biophys. J. **93**(11), 3884.

[128] P.R. Cullis and B. De Kruijff (1978) "Polymorphic phase behavior of lipid mixtures as detected by ^{31}P NMR. Evidence that cholesterol may destabilize bilayer structure in membrane systems containing phosphatidylethanolamine." Biochimica et Biophysica Biomembranes **507**(2), 207.

[129] D.L. Daleke (2003) "Regulation of transbilayer plasma membrane phospholipid asymmetry." J. Lipid Res. **44**(2), 233.

[130] P.A. Leventis and S. Grinstein (2010) "The distribution and function of phosphatidylserine in cellular membranes." Annu. Rev. Biophys. **39**, 407.

[131] B.H. Falkenburger, J.B. Jensen, E.J. Dickson, B-C. Suh, and B. Hille (2010) "Phosphoinositides: lipid regulators of membrane proteins" J. Physiol. **588**, 3179.

[132] G.R.V. Hammond and T. Balla (2015) "Polyphosphoinositide binding domains: key to inositol lipid biology." Biochimica et Biophysica Acta **1851**, 746.

[133] J.E. Ferrell Jr. and W.H. Huestis (1984) "Phosphoinositide metabolism and the morphology of human erythrocytes." J. Cell Biol. **98**(6), 1992.

[134] S. McLaughlin, J. Wang, A. Gambhir, and D. Murray (2002) "PIP(2) and proteins: interactions, organization, and information flow." Annu. Rev. Biophys. Biomol. Struct. **31**. 151.

[135] J. Vlach and J.S. Saad (2013) "Trio engagement via plasma membrane phospholipids and myristoyl moiety governs HIV-1 matrix binding to bilayers." Proc. Natl. Sci. USA **110**(9), 3525.

[136] M. Geyer, O.T. Fackler, and B. Matija Peterlin (2001) "Structure-function relationships in HIV-1 Nef." EBMO *reports* **2**(71), 580.

[137] M. Harris (1996) "From negative factor to a critical role in virus pathogenesis: the changing fortunes of Nef." J. of Gen. Virol. **77**, 2379.

[138] N. Ahmad and S. Venkatesan (1988) "Nef protein of HIV-1 is a transcription repressor of HIV-1 LTR" Science **241**, 1481.

[139] C. Cheng-Mayer, P. Iannello, K. Shaw, P.A. Luciw, and J.A. Levy (1989) "Differential effects of nef on HIV replication: implications for viral pathogenesis in the host." Science **236**, 1629.

[140] P.A. Luciw, C. Cheng-Mayer, and J.A. Levy (1987) "Mutational analysis of the human immunodeficiency virus: the orf-B region down-regulates virus replication." Proc. Natl. Sci. USA **84**(5), 1434.

106

[141] T.M. Niederman, B.J. Thielen, and L. Ratner (1989) "Human immunodeficiency virus type 1 negative factor is a transcriptional silencer." Proc. Natl. Sci. USA **86**(4), 1128.

[142] C. Aiken and D. Trono (1995) "Nef stimulates human immunodeficiency virus type 1 proviral DNA synthesis." J. Virol. **69**(8), 5048.

[143] M.Y. Chowers, C.A. Spina, T.J. Kwoh, N.J. Fitch, D.D. Richman, and J.C. Guatelli (1994) "Optimal infectivity in vitro of human immunodeficiency virus type 1 requires an intact nef gene." J. Virol. **68**(5), 2906.

[144] M.D. Miller, M.T. Warmerdam, I. Gaston, W.C. Greene, and M.B. Feinberg (1994) "The human immunodeficiency virus-1 *nef* gene product: a positive factor for viral infection and replication in primary lymphocytes and macrophages." J. Exp. Med. **179**, 101.

[145] C.A. Spina, T.J. Kwoh, M.Y. Chowers, J.C. Guatelli, and D.D. Richman (1994) "The importance of nef in the induction of human immunodeficiency virus type 1 replication from primary quiescent CD4 lymphocytes." J. Exp. Med. **179**, 115.

[146] Z. Hanna, D.G. KAy, N. Rebai, A. Guimond, S. Jothy, and P. Jolicoeur (1998) "Nef harbors a major determinant of pathogenicity for an AIDS-like disease in transgenic mice." Cell **95**(2), 163.

[147] N.J. Deacon, A. Tsykin, A. Solomon, K. Smith, M. Ludford-Menting, D.J. Hooker, D.A. McPhee, A.L. Greenway, A. Ellet, C. Chatfield, V.A. Lawsone, S. Crowe, A. Maerz, S. Sonza, J. Learmont, J.S. Sullivan, A. Cunningham, D. Dwyer, D. Dowton, and J. Mills. (1995) "Genomic structure of an attenuated quasi species of HIV-1 from a blood transfusion donor and recipients." Science **270**, 988.

[148] F. Kirchhoff, T.C.Greenough, D.B. Brettler, J.L. Sullivan, and R.C. Desrosiers (1995) "Absence of intact nef sequences on long-term survivor with nonprogressive HIV-1 infection." N. Engl. Med **332**, 228.

[149] B.M. Peterlin and D. Trono (2003) "Hide, shield, and strike back: how HIV-infected cells avoid immune eradication." Nat. Rev. Immunol. **3**(2):97.

[150] E. O'Neill, L.S. Kuo, J.F. Krisko, D.R. Tomchick, J.V. Garcia, and J.L. Foster (2006) "Dynamic evolution of the human immunodeficiency virus type 1 pathogenic factor, Nef." J. of. Virol. **80**(3), 1311.

[151] A.M. Joseph, M. Kumar, and D. Mitra (2005) "Nef: "necessary and enforcing factor" in HIV infection." Curr. HIV Res. **3**(1), 87.

[152] R.P. Trible, L. Emert-Sedlak, and T.E. Smithgall (2006) "HIV-1 Nef selectively activates Src family kinases Hck, Lyn, and c-Src through direct SH3 domain interaction." J. Biol. Chem. **281**(37), 27029.

[153] A. Rosa, A. Chande, S. Ziglio, V. De Sanctis, R. Bertorelli, S.L. Goh, S.M. Mc-Cauley, A. Nowosielska, S.E. Antonarakis, J. Luban, F.A. Santoni, and M. Pizzato (2015) "HIV-1 Nef promotes infection by excluding SERINC5 from virion incorporation." Nature **526**(7572)212.

[154] M.E. Klotman, S. Kim, A. Buchbinder, A. DeRossi, D. Baltimore, and F. Wong-Staal (1991) "Kinetics of expression of multiply spliced RNA in early human immunodeficiency virus type 1 infection of lymphocytes and monocytes." Proc. Natl. Acad. Sci. U.S.A. **88**, 5011.

[155] K. Coates, S.J. Cooke, D.A. Mann, and M.P.G. Harris (1997) "Protein kinase C-mediated phosphorylation of HIV-1 Nef in human cell lines." J. Biol. Chem. **272**(19):12289.

[156] X.Ren, S.Y. Park, J.S. Bonifacino, and J.H. Hurley (2014) "How HIV-1 NEf hijacks the AP-2 clathrin adaptor to downregulate CD4." eLife **3**, e01754.

[157] M. Bentham, S. Mazaleyrat, and M. Harris (2006) "Role of myristoylation and N-terminal basic residues in membrane association of the human immunodeficiency virus type 1 Nef protein." J. Gen. Virol. **87**, 563.

[158] B. Peng and M. Robert-Guroff (2001) "Deletion of N-terminal myristoylation site of HIV Nef abrogates both MHC-1 and CD4 down-regulation." Immunol. Letter **78**(3), 195.

[159] Z. Hanna, E. Priceputu, D.G. Kay, J. Poudrier, P. Chrobak, and P. Jolicoeur (2004) "In vivo mutational analysis of the N-terminal region of HIV-1 Nef reveals critical motifs for the development of an AIDs-like disease in CD4/HIV transgenic mice." Virology **327**(2), 273.

[160] C-H. Lee, K. Saksela, U.A. Mirza, B.T. Chait, and K. Kuriyan (1996) "Crystal structure of the conserved core of HIV-1 Nef complexed with a Src family SH3 domain." Cell **85**, 931.

[161] S. Arold, P. Franken, M.P. Strub, F. Hoh, S. Benichou, R. Benarous, and C. Dumas (1997) "The crystal structure of HIV-1 Nef protein bound to Fyn kinase SH3 domain suggests a role for this complex in altered T cell receptor signaling." Structure **5**(10), 1361.

[162] S. Breuer, H. Gerlach, B. Kolaric, C. Urbanke, N. Optiz, and M. Geyer (2006) "Biochemical indication for myristoylation-dependent conformational changes in HIV-1 Nef." Biochem. **45**, 2339.

[163] S. Grzesiek, A. Bax, G.M. Clore, A.M. Gronenborn, J.S. Hu, J. Kaufman, I. Palmer, S.J. Stahl, and P.T. Wingfield. "The solution structure of HIV-1 Nef reveals an unexpected delineations of the binding site for the SH3 domain of Hck tyrosine kinase." Nat. Struct. Biol. **3**, 340.

[164] S.I. Giese, I. Woerz, S. Homann, N. Tibroni, M. Geye, and O.T. Fackler (2006) "Specific and distinct determinants mediate membrane binding and lipid raft incorporation of HIV-1$_{SF2}$ Nef." Virol. **355**, 175.

[165] R. Welker, M. Harris, B. Cardel, and H-G. Kräusslich (1998) "Virion incorporation of human immunodeficiency virus type 1 Nef is mediated by a bipartite membrane-targeting signal: analysis of its role in enhancement of viral infectivity." J. of Virol. **72**(11), 8833.

[166] S. Arold, F. Hoh, S. Domergue, C. Birck, M-A. Delsuc, M. Jullien, and C. Dumas (2000) "Characterization and molecular basis of the oligomeric structure of HIV-1 Nef protein." Prot. Sci. **9**, 1137.

[167] L.A. Emert-Sedlak, P. Narute, S.T. Shu, J.A. Poe, H. Shi, N. Yanamala, J.J. Alvarado, J.S. Lazo, J.I. Yeh, P.A. Johnston, and T.E. Smithgall (2013) "Effector kinase coupling high-throughput screens for direct HIV-1 Nef antagonists with anti-retroviral activity." Chem. Biol. **20**(1), 82.

[168] N. Kienzle, J. Freund, H.R. Kalbitzer, N. Mueller-Lantzsch (1993) "Oligomerization of the Nef protein from human immunodeficiency virus (HIV) type 1." FEBS **214**, 451.

[169] Y. Fujii, K. Otake, M. Tashiro, and A. Adachi (1996) "Soluble Nef antigen of HIV-1 is cyotoxic form human CD4+ T cells." FEBS Lett. **393**, 93.

[170] H. Ye, H-J. Choi, J. Poe, and T.E. Smithgall "Oligomerization is required for HIV-1 Nef-induced activation of the Src family protein-tyrosine kinase, Hck." Biochem. **43**, 15775.

[171] K. Neet and T. Hunter (1996) "Vertebrate non-receptor protein-tyrosine kinase families." Genes to Cells **1**, 147.

[172] L.J. Berg, L.D. Finkelstein, J.A. Lucas, and P.L. Schwartzberg (2005) "Tec family kinases in T lymphocyte development and function." Annu. Rev. Immunol. **23**, 549.

[173] J.A. Readinger, K.L. Mueller, A.M. Venegas, R. Horai, P.L. Schwartzberg (2009) "Tec kinases regulate T-lymphocyte development and function: new insights into the roles of Itk and Rlk/Txk." Immun. Rev. **228**, 93.

[174] P.L. Schwartzberg, L.D. Finkelstein, and J.A. Readinger (2005) "Tec-family kinases: regulators of T-helper-cell differentiation." Nat. Rev. Immun. **5**, 284.

[175] C.I. Edvard Smith, T.C. Islam, P.T. Mattsson, A.J. Mohamed, B.F. Nore and M. Vihenen (2001) "The Tec family of cytoplasmic tyrosine kinases: mammalian Btk, Bmx, Itk, Tec, Txk and homologs in other species." BioEssays **23**, 436.

[176] C.M. Lewis, C. Broussard, M.J. Czar, and P.L. Schwartzberg (2001) "Tec kinases: modulators of lymphocyte signaling and development." Curr. Opin. in Immun. **13**, 317.

[177] W.C. Yang, Y. Collette, J.A. Nunes, and D. Olive (2000) "Tec kinases: a family with multiple roles in immunity." Immunity **12**, 373.

[178] K. Saksela (2011) "Interactions of the HIV/SIV pathogenicity factor Nef with SH3 domain-containing host cell proteins." Curr. HIV Res. **9**(7), 531.

[179] H.J. Choi and T.E. Smithgall (2004) "Conserved residues in the HIV-1 Nef hydrophobic pocket are essential to recruitment and activation of the Hck tyrosine kinase." J. Mol. Biol. **343**, 1255.

[180] S.D. Briggs, M. Sharkey, M. Stevenson, and T.E. Smithgall (1997) "SH3- mediated Hck tyrosine kinase activation and fibroblast transformation by the Nef protein of HIV-1." J. Biol. Chem. **272**, 17899.

[181] I. Moarefi, M. LaFevre-Bernt, F. Sicheri, M. Huse, C-H. LEe, J. Kuriyan, and W.T. Miller (1997) "Activation of the Src-family tyrosine kinase Hck by SH3 domain displacement." Nature **385**, 650

[182] A.H. Andreotti, P.L. Schwartzberg, R.E. Joseph, and L.J. Berg (2010) "T-Cell signaling regulated by the Tec family kinase, Itk." Cold Spring Harb. Perspect. Biol. **2**(7), a002287.

[183] J.J. Alvarado, S. Tarafdar, J.I. Yeh, and T.E. Smithgall (2014) "Interaction with the SH3-SH2 region of the Src-family kinase Hck structures the HIV-1 Nef dimer for kinase activation and effector recruitment." J. Biol. Chem. **289**, 28539.

[184] S.E. Boyken, D.B. Fulton, and A.H. Andreotti (2012) "Rescue of the aggregation prone Itk Pleckstrin Homology domain by two mutations derived from the related kinases, Btk and Tec." Prot. Sci. **21**, 1288.

[185] R. Sheng, D-J. Jung, A. Silkov, H. Kim, I. Singaram, and Z-G. Wang, Y. Xin, E. Kim, M-J. Park, P. Thiagarajan-Rosenkranz, S. Smrt, B. Honig, K. Baek, S. Ryu, J. Lorieau, Y-M. Kim, and W Cho (2016) "Lipids regulate Lck activity through their interactions with the Lck SH2 domain." J. Biol. Chem. **291**(34), 17639.

[186] S.M Thomas and J.S. Brugge (1997) "Cellular functions regulated by Src family kinases." Annu. Rev. Biochem. **69**, 373.

[187] T.J. Boggon and M.J. Eck (2004) "Structure and regulation of Src family kinases." Oncogene **23**, 7918

[188] J.G. Hoey, J. Summy, and D.C. Flynn (2000) "Chimeric constructs containing the SH4/Unique domains of cYes can restrict the ability of Src(527F) to upregulate heme oxygenase-1 expression efficiently." Cell Signal **12**, 691.

[189] J.M. Summy, Y. Qian, B.H. Jiang, A. Koay-Guappone, A. Gatesman, X. Shi, and D.C. Flynn (2003) "The SH4-Unique-SH3-SH2 domains dictate specificity in signaling that differentiate c-Yes from C-Src." J. Cell Sci. **116**, 2585.

[190] S. Carréno, M-E. Gouze, S. Schaak, and L.J. Emorine (2000) "Lack of palmitoylation redirects p59$^{\text{Hck}}$ from the plasma membrane to p61$^{\text{Hck}}$-positive lysosomes." J. Biol. Chem. **275**(46), 36223.

[191] S.M. Robbins, N.A. Quintrell, and J.M. Bishop (1995) "Myristoylation and differential palmitoylation of the Hck protein-tyrosine kinases govern their attachment to membranes and association with caveolae." Mol. and Cell. Biol. **15**, 3507.

[192] K. Zhao, H. Zhou, X. Zhao, D.W. Wolff, Y. Tu, H. Liu, T. Wei, and F. Yang (2012) "Phosphatidic acid mediates the targeting of tBid to induce lysosomal membrane permeabilization and apoptosis." J. Lipid Research **53**, 2102.

[193] T. Pene-Dumitrescu and T.E. Smithgall (2010) "Expression of a Src family kinase in chronic myelogenous leukemia cells induces resistance to imatinib in a kinase-dependent manner." J. Biol. Chem. **285**, 21446.

[194] A. Klejman, S.J. Schreiner, M. Nieborowska-Skorska, A Slupianek, M. Wilson, T.E. Smithgall, and T. Skorski (2002) "The Src family kinase Hck couples BCR/ABL to STAT5 activation in myeloid leukemia cells." EMBO J. **21**, 5766.

[195] M. Hiyoshi, S. Suzu, Y. Yoshidomi, R. Hassan, H Harada, N. Sakashita, H. Akari, K. Motoyoshi, and S. Okada (2008) "Interaction between Hck and HIV-1 Nef negatively regulates cell surface expression of M-CSF receptor." Blood **111**(1), 243.

[196] S. Suzu, H. Harada, T. Matsumoto, and S. Okada (2005) "HIV-1 Nef interferes with M-CSF receptor signaling through Hck activation and inhibits M-CSF bioactivities." Blood **105**, 3230.

[197] R. Hassan, S. Suzu, M. Hiyoshi, N. Takahashi-Makise, T. Ueno, T. Agatsuma, H. Akari, J. Komano, Y. Takebe, K. Motoyoshi, and S. Okada (2009) "Dys-regulated activation of a Src tyrosine kinase Hck at the Golgi disturbs N-glycosylation of a cytokine receptor Fms." J. Cell Physiol. **221**(2), 458.

[198] T. Holemans, D. Mollerup Sørensen, S. van Veen, S. Martin, D. Hermans, G. Christine Kemmer, C. Van den Haute, V. Baekelandt, T. Günther Pomorski, P. Agostinis, F. Wuytack, M. Palmgren, J. Eggermont, and P. Vangheluwe (2015) "A lipid switch unlocks Parkinson's disease-associated ATP13A2." Proc. Nat. Acad. Sci. **112**(29), 9040.

[199] C.T. Sigal, W. Zhou, C.A. Buser, S. McLaughlin, and M.D. Resh (1994) "Amino-terminal basic residues of Src mediate membrane binding through electrostatic interaction with acidic phospholipids." Proc. Nat. Acad. Sci. **91**, 12253.

[200] E.E. Kooijman, D. Peter Tielman, C. Testerink, T. Munnik, D.T.S. Rijkers, K.N.J. Burger, and B. de Kruijff (2007) "An electrostatic/hydrogen bond switch as the basis for the specific interaction of phosphatidic acid with proteins." J. Biol. Chem. **282**(15), 11356.

[201] E.E. Kooijman, K.M. Carter, E.G. van Laar, V. Chupin, K.N. Burger, and B. de Kruijff (2005) "What makes the bioactive lipids phosphatidic acid and lysophosphatidic acid so special?" Biochem. **44**(51), 17007.

[202] J. JH Shin and C. JR Loewen (2011) "Putting the pH into phosphatidic acid signaling." *BMC* Biol. **9**, 85.

[203] J.A. De Feijter, J. Benjamins and F.A. Veer (1978) "Ellipsometry as a tool to study the adsorption behavior of synthetic and biopolymers at the air-water interface." Biopolymers **17**(7). 1759.

[204] A-L. Le Roux, M.A. Busquets, F. Sagués, and M. Pons (2015) "Kinetics characterization of c-Src binding to lipid membranes: switching from labile to persistent binding." Colloids & Surfaces B: Biointerfaces **138**, 17.

[205] B.T. Andresen, M.A. Rizzo, K. Shome, and G. Romero (2002) "The role of phosphatidic acid in the regulation of the Ras/MEK/Erk signaling cascade." FEBS Letter **531**, 65.

[206] C. Testerink and T. Munnik (2005) "Phosphatidic acid: a multifunctional stress signaling lipid in plants." Trends Plants Sci. **10**(8), 368.

[207] M. Maffei, M. Arbesú, A-L. Le Roux, I. Amata, S. Roche, and M. Pons (2015) "The SH3 domain acts as a scaffold for the N-terminal intrinsically disordered regions of c-Src." Structure **23**(5), 893.

[208] K. Moravcevic, C.L. Oaxley, and M.A. Lemmon (2012) "Conditional peripheral membrane proteins: facing up to limited specificity." Structure **20**, 15.